Microenvironment-mediated cancer dormancy and metastasis: implications for cell biophysics and biology

vorgelegt von
M. Sc.
Sadra Bakhshandeh

an der Fakultät III - Prozesswissenschaften
der Technischen Universität Berlin
zur Erlangung des akademischen Grades

Doktor der Ingenieurwissenschaften
-Dr.-Ing.-

genehmigte Dissertation

Promotionsausschuss:
Vorsitzenderin: Prof. Dr. rer. nat. Sina Bartfeld
Gutachter: Prof. Dr. rer. nat. Roland Lauster
Gutachterin: Dr. Amaia Cipitria
Tag der wissenschaftlichen Aussprache: 18. Februar 2022

Berlin 2023

Zusammenfassung

Bei kurativ resezierten soliden Tumoren kommt es trotz systemischer Verabreichung molekular adaptierter (neo)adjuvanter Behandlungen oder Chemotherapien häufig zu einem Rückfall mit Metastasen in anderen Organen (wobei Knochen zu den am häufigsten betroffenen Organen gehören). Die Bildung von Metastasen in sekundären Organen erfolgt möglicherweise nicht sofort, sondern kann Jahre bis Jahrzehnte dauern, was darauf hindeutet, dass eine Reihe der Krebszellen in einen arzneimittelresistenten Ruhezustand übergeht. Durch die Seltenheit und die Komplexität, die mit dem Nachweis, der Isolierung und der Analyse von disseminierten Tumorzellen (DTCs) in symptomfreien Patienten verbunden sind, ist es dringend notwendig, in-vitro-Kultursysteme zu entwickeln, die diesen asymptomatischen Zustand der Krebsmetastasierung künstlich nachahmen. Dadurch werden skalierbare Wirkstoffscreening-Kampagnen zur Identifizierung von Medikamenten ermöglicht, die gegen DTCs gerichtet sind. Jüngste Studien haben gezeigt, dass eine dichte extrazelluläre Matrix (ECM) einzelne disseminierte Krebszellen einschließt, was darauf hindeutet, dass die ECM-vermittelte mechanische Einschließung ein plausibler Mechanismus ist, der die Krebszellenruhe auslöst.

Wir haben eine Ruhe-induzierende 3D-Matrix unter Verwendung von kovalent vernetzten Thiol-En-Alginat-Hydrogelen mit ultraviolettem (UV) Licht entwickelt, welche einen mechanischen Einschluss erzeugt, der das Wachstum von schwach und stark metastasierenden Brustkrebszelllinien blockiert. Nach einer umfassenden Materialcharakterisierung der entwickelten Plattform sowie einer gründlichen phänotypischen Beschreibung (d.h. Viabilität, Stoffwechselaktivität, Zellzykluszustand, Proliferation, Medikamentenempfindlichkeit) der eingekapselten Zellen haben wir die biophysikalischen Eigenschaften dieser wachstumsfixierten Zellen mit modernsten kontakt- und markierungsfreien Techniken untersucht. Insbesondere haben wir die 3D Massendichteverteilung der eingekapselten menschlichen Brustkrebszellen (BCC) MDA-MB-231 mit einer kombinierten optischen Beugungstomographie (ODT) und Epifluoreszenz- Mikroskop quantitativ ausgewertet. Anschließend haben wir die viskoelastischen 3D-Eigenschaften dieser Zellen mittels Brillouin-Spektroskopie erfasst. Im Gegensatz zu Zellen die auf 2D Substraten haften, wiesen die Kerne von Zellen in der 3D Umgebung überraschenderweise eine höhere Massendichte sowie eine höhere Steifigkeit und Viskosität im Vergleich zum Zytoplasma auf.

Als Nächstes sind wir zu einer molekularen Charakterisierung (d. h. Immunfärbung ausgewählter Moleküle, RNA-Sequenzierung) von Zellen mit Wachstumsstillstand übergangen. Wir konnten zeigen, dass unsere künstliche, Ruhe-induzierende Matrix unterschiedliche Populationen von wachstumsgestoppten Zellen selektiert, wobei Zellen in der G0/G1-

Zellzyklusphase resistenter gegen die Blockade sind. In Kombination mit der RNA-Sequenzierung konnten wir eine steifigkeitsabhängige Kernlokalisierung des Proteins ‚Four-and-a-half LIM-Domains 2' (FHL2) als zugrundeliegenden Mechanismus des Ruhezustandes nachweisen. Diese Lokalisation führt zu einer p53-unabhängigen p21Cip1/Waf1-Expression, welche in menschlichem und murinem Gewebe validiert wurde. Die ruhenden Zellen reagieren nach der Herunterregulierung von FHL2 empfindlich auf eine medikamentöse Behandlung, was auf eine resistenzverursachende Rolle von FHL2 hindeutet und das Potenzial unseres Ansatzes als Instrument für die Identifizierung und gezielte Suche von neuen Wirkstoffen zur Ausrottung potenziell rezidivierender DTCs belegt.

Schließlich wollten wir in einem physiologisch relevanteren System beobachten, wie sich DTCs im Knochen verhalten. Aufbauend auf einer wachsenden Zahl von Hinweisen auf Parallelen zwischen DTCs und ruhenden hämatopoetischen Vorläufer-Stammzellen (HSPCs) haben wir DTCs in ein mit primären humanen mesenchymalen Stromazellen (MSCs) und multipotenten HSPCs, aus menschlichem Nabelschnurblut, vorbesiedeltes 3D-Hydroxylapatit-beschichtetes Zirkonoxid-Gerüst ausgesät. Interessanterweise können wir BCCs und HSPCs nachweisen, die in einem spinnwebenartigen Netzwerk aus Fibronektin eingeschlossen sind, wobei die BCCs zu einem langsam proliferativen Zustand neigen, was auf eine potenziell ruhezustandsfördernde Rolle der Knochenmikroumgebung hindeutet.

Trotz der inhärenten Komplexität, die mit der molekularen Charakterisierung biologischer Prozesse verbunden ist, ermöglicht die Betrachtung dieser Phänomene aus einer physikalischen Perspektive eine globalere Beschreibung, die von vielen Details der Systeme unabhängig ist. Durch das Ziehen von Parallelen von klinischen und experimentellen Daten und aufbauend auf thermodynamischen Phasentrennungskonzepten haben wir die durch die Mikroumgebung vermittelten Ruhemechanismen in Form von Keimbildungsprozessen klassifiziert, die auf drei verschiedenen Klassen von Wechselwirkungen basieren: (i) Zellen, die an einer benetzenden flachen Oberfläche in Form einer kugelförmigen Kappe haften, (ii) ein kugelförmiges Tröpfchen, das von einer elastischen Hülle umschlossen wird, als mechanische Interpretation der durch die extrazelluläre Matrix (ECM) vermittelten Begrenzung, und (iii) ein kugelförmiges Tröpfchen mit größenabhängig begrenztem Wachstum aufgrund von Nährstoff- und Sauerstoffmangel, was zur Zellapoptose tief im Gewebe führt. Anschließend stellen wir die These auf, dass lokale Energieminima oder metastabile Zustände, die in der Wachstumskinetik des Gewebetropfens auftreten, als Stellvertreter für ruhende Zustände betrachtet werden können. Trotz seiner Einfachheit erfasst das vorgestellte Modell mehrere Aspekte im Zusammenhang mit Krebsruhezuständen und Tumorwachstum.

Abstract

Curatively resected solid cancers often relapse with distant metastasis (the bone being among the preferred sites), despite systemic administration of molecularly tailored (neo)adjuvant or chemo-therapies. Outgrowth of tumor cells disseminated to secondary organs might not occur instantly, with recurrences ranging from years to decades, pointing to the fact that a number of these cells might go into a drug-resistant state of dormancy. The rarity and complexity associated with detection, isolation and analysis of disseminated tumor cells (DTCs) in disease-free patients have called for an urgent need to develop in vitro culture systems to artificially mimic this asymptomatic state of cancer metastasis, therefore enabling scalable drug screening campaigns to identify drugs able to target DTCs. Recent studies have found dense extracellular matrix (ECM) confining individual disseminated cancer cells, hinting to ECM-mediated mechanical confinement to be a plausible mechanism inducing cancer dormancy.

Here we engineered a quiescence-inducing three-dimensional (3D) engineered matrix using ultraviolet (UV) light-initiated covalently-crosslinked thiol-ene alginate hydrogels, which generates mechanical confinement inducing growth arrest of weakly and highly metastatic breast cancer cell lines. After extensive material characterization of the engineered platform, as well as thorough phenotypic profiling (i.e. viability, metabolic activity, cell cycle state, proliferation, drug sensitivity) of the encapsulated cells, we looked at the biophysical properties of these growth-arrested cells with state-of-the-art contact/label-free techniques. Specifically, we quantitatively mapped the 3D mass density distribution of encapsulated human breast cancer cells (BCCs) MDA-MB-231, using a combined optical diffraction tomography (ODT)-epifluorescence microscope. We then mapped the 3D viscoelastic properties of these cells via Brillouin spectroscopy. Surprisingly, and in contrast to cells adhering to 2D substrates, the nuclei of cells in 3D revealed a higher mass density, as well as higher stiffness and viscosity compared to the cytoplasm.

Next, we moved to a more molecular characterization (i.e. immunostaining of selected molecules, RNA seq) of growth-arrested cells. We showed that our artificial quiescence-inducing matrix selects for distinct populations of growth-arrested cells, with cells in the G0/G1 cell cycle phase being more resistant to confinement. Combined with RNA sequencing, we revealed a stiffness-dependent nuclear localization of the four-and-a-half LIM domains 2 (FHL2) protein as an underlying mechanism of quiescence, which led to a p53-independent p21Cip1/Waf1 expression, validated in human and murine tissue. Suggestive of a resistance-causing role, quiescent cells became sensitive against drug treatment upon FHL2 downregulation, evidencing

the potential of our approach as a tool for the identification and targeting screens for novel compounds suited to eradicate potentially relapsing DTCs.

Finally, we sought to observe how DTCs behave in the bone in a more physiologically relevant system. Building on a growing body of evidence suggesting the existence of parallels between DTCs and quiescent hematopoietic and progenitor stem cells (HSPCs), we seeded DTCs within a 3D hydroxyapatite-coated zirconium oxide scaffold pre-seeded with primary human mesenchymal stromal cells (MSCs) and human cord blood-derived multipotent HSPCs. Interestingly, we detected BCCs and HSPCs entrapped in a web-like network of fibronectin, with BCCs leaning towards a slow-proliferative state, hinting at a potential quiescence-inducing role for the bone microenvironment.

Despite the inherent complexities associated with the molecular characterization of biological processes, viewing these phenomena from a physical perspective allows for a more global description, independent from many details of the systems. By drawing parallels with clinical and experimental data, and building on thermodynamic phase separation concepts, we classified microenvironmental-mediated dormancy mechanisms in terms of nucleation processes based on three distinct classes of interactions: (i) cells adhering to a wetting flat surface in the form of a spherical cap (ii) a spherical droplet enclosed by an elastic sheath as a mechanical interpretation of extracellular matrix (ECM)-mediated confinement, and (iii) a spherical droplet with size-dependent limited growth due to lack of nutrients and oxygen, leading to cell apoptosis deep inside the tissue. We then advance the notion that local energy minima, or metastable states, emerging in the tissue droplet growth kinetics can be considered proxies of dormant states. Despite its simplicity, the provided framework captures several aspects associated with cancer dormancy and tumor growth.

Table of Contents

1

State of the art

1.1 Physical aspects of cancer and how to model them

Cancer had been classically considered a disease concerning genetic mutations at the cellular level [1], until recent findings advanced the notion that the microenvironment has an unneglectable role in driving tumor initiation and progression [2]. The latter involves physiochemical disruption of the microenvironment, emphasizing the need for an attempt to investigate some cancer-associated aspects from a physical perspective [2] (Fig.1.1).

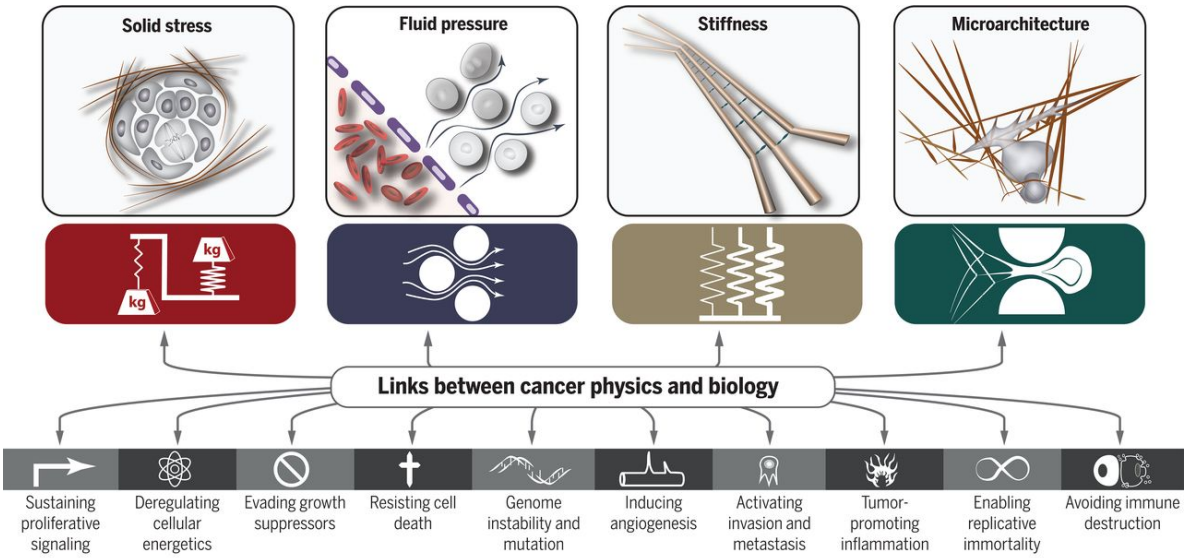

Figure 1.1: Some physical aspects of cancer and its microenvironment known to affect several biological hallmarks of cancer. Reproduced with permission from [2].

Cell's microenvironment, or niche, consists of biochemical factors, neighboring cells, as well as the extracellular matrix (ECM) [3]. The latter, besides functioning as a supporting scaffold, can actively influence cells behavior via its composition and dynamic regulation [3, 4] (Fig.1.2).

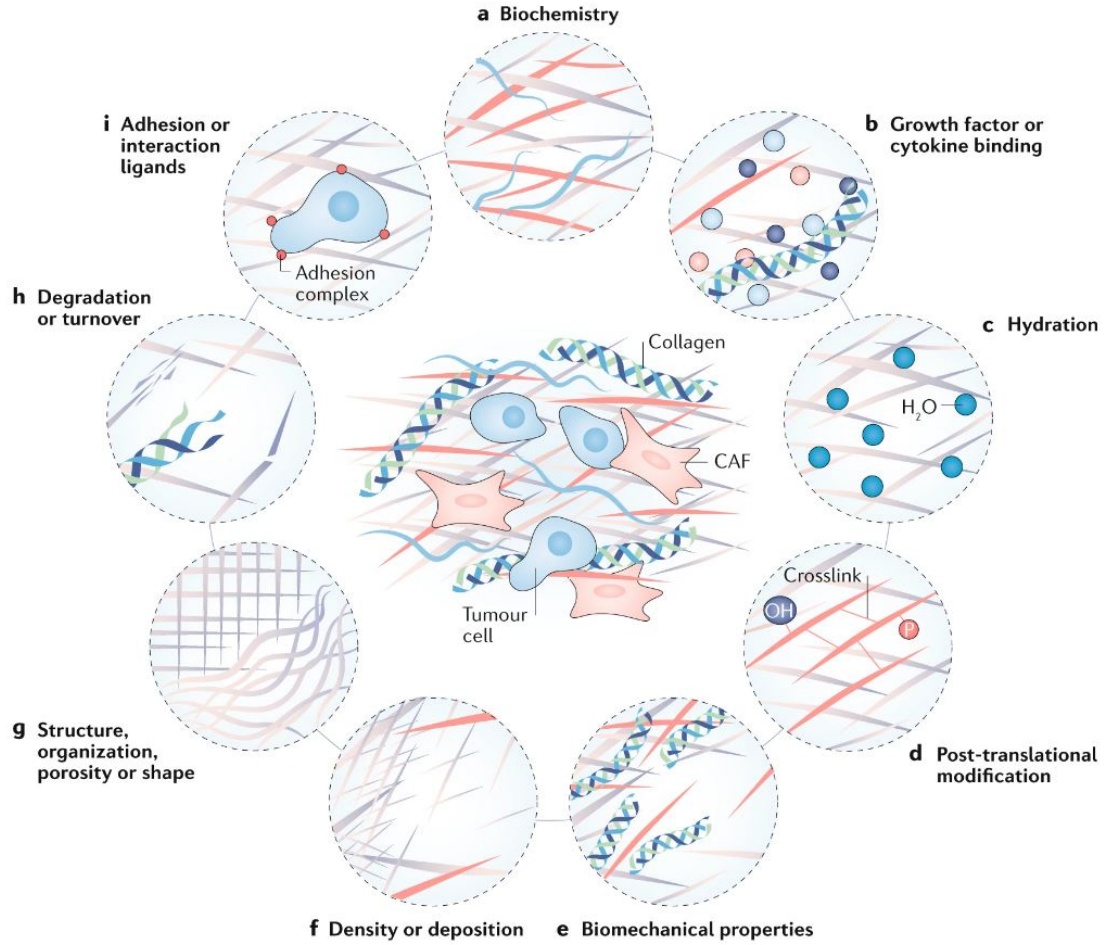

Figure 1.2: The extracellular matrix (ECM) in both physiological and pathological settings perform several important functions, far from being a simple passive scaffold (CAF=cancer associated fibroblasts). Reproduced with permission from [4].

So far, the overwhelming focus in stem cell, cancer and organoid research has been on describing the role of biochemical or genetic factors involved in cell response, with the ECM gaining traction only in the latest years [2]. The highly fibrous and hydrated nature of the ECM motivated the use of water-absorbing polymeric materials, known as hydrogels, to mimic the structural aspects of cell's microenvironment (a feature neglected in conventional two-dimensional (2D) cultures), as 3D cell culture biomaterials [5]. Conveniently, most recent hydrogels have been shown to allow specific, controlled and independent tuning of both biophysical and biochemical properties, further enabling tailored configurations fitting different applications [5, 6, 7] (Fig.1.3).

Alginate hydrogels, in particular, derived from brown seaweed algae, are known as being naturally inert (non-cytotoxic and non-adherent), while allowing for several chemical modifications as well as different crosslinking modalities [8]. These span from ionic to covalent crosslinking, which, based on molecular weights, ratios and composition, can yield hydrogels with a wide range of elastic and viscous properties [8]. Furthermore, alginate hydrogels allow for fast and simple chemical functionalization with biomolecules such as the adhesive peptide RGD [9], or as drug carriers to deliver transforming growth factor-beta 1 (TGF-β1)

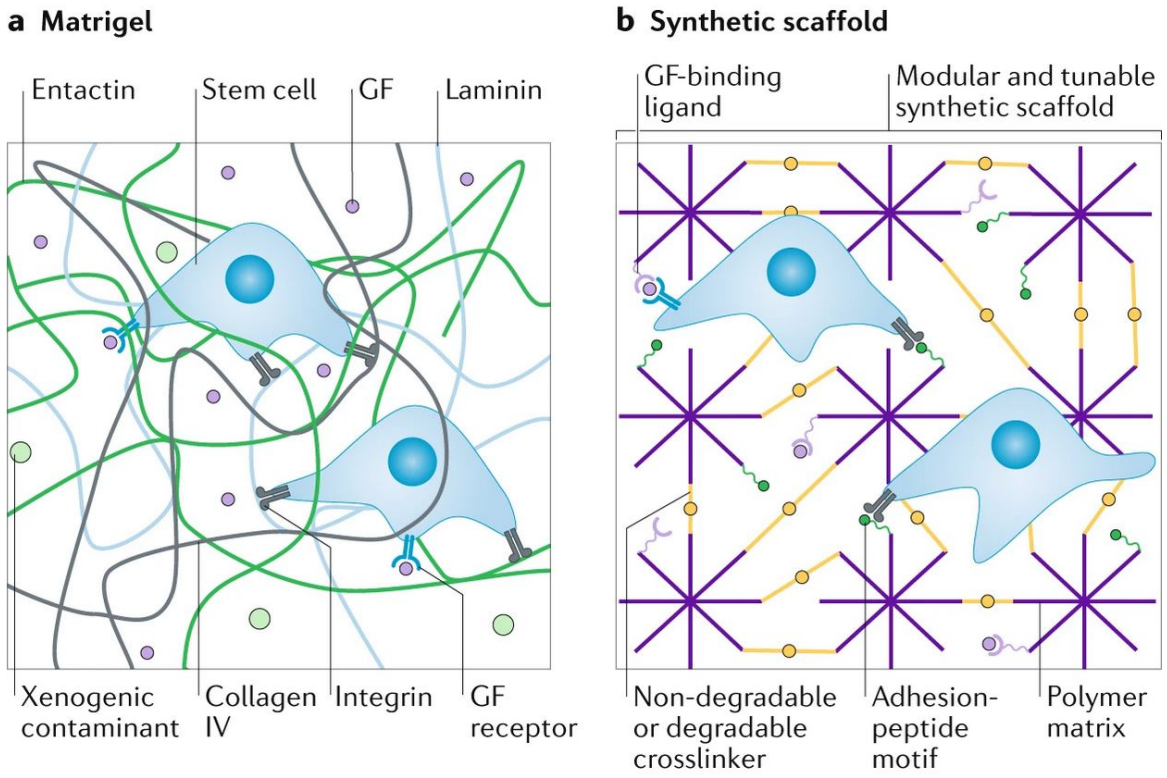

Figure 1.3: Comparison of Matrigel and synthetic scaffolds. The latter is highly tunable from both physical and chemical aspects unlike the former. Reproduced with permission from [7].

[10], bone morphogenetic proteins (BMPs) [11] and vascular endothelial growth factors (VEGF) [12]. This versatility has enabled unprecedented findings on the mechanism of cell-ECM interactions, uncovering the critical role of ECM biophysical properties such as matrix stiffness [13], viscoelasticity [14], adhesion [15], or matrix degradability [16] on cell response. The independent effect of these physical properties is hard to decouple, especially in in-vivo scenarios, further stressing the importance of having tunable systems to allow such deconvolution [17] (Fig.1.4). This is essential considering the highly dynamic nature of the ECM, which stems from its stepwise deposition formation, chemical modification at the post-translational level, proteolytic degradation and force-mediated physical remodeling [18].

These aspects are further accentuated in cancer, where highly proliferative malignant cells chemically and physically remodel the ECM at higher rates than normal [18]. In this regard, higher stiffness of the stroma surrounding solid tumors is now considered a hallmark of cancer [4]. Several studies have similarly reported high ECM stiffness to be a driver of malignancy in human epithelial breast cancer cells [13, 19, 20]. Nonetheless, research about the role of the ECM in cancer progression has so far centered around primary tumor, and less on later stages following metastasis such as homing and dormancy at secondary sites.

1.2 Cancer dormancy: the quest for in vitro models

Dormancy is an evolutionary-conserved mechanism found in bacteria [21], worms [22], plant seeds [23] as well as eukaryotic cells [24], which is activated upon exposure to hostile

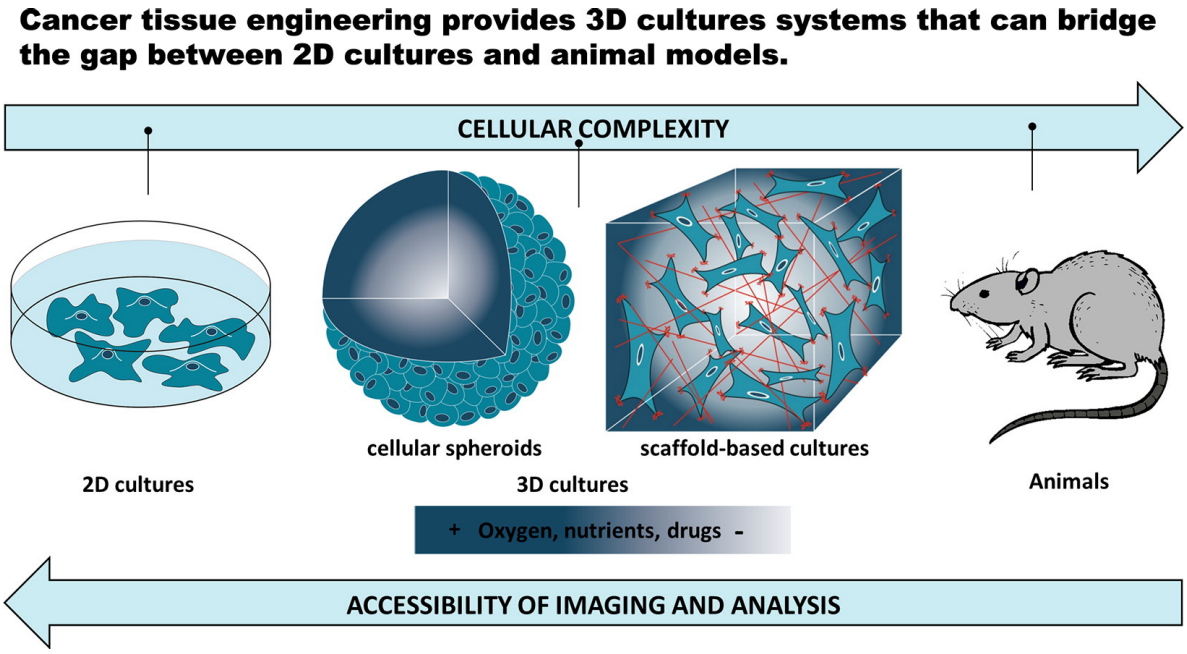

Figure 1.4: Comparison of Matrigel and synthetic scaffolds. The latter is highly tunable from both physical and chemical aspects unlike the former. Reproduced with permission from [17].

circumstances, enabling low energy consumption until favorable growth conditions are once again met [24]. Such mechanism is similarly exploited by cancer cells, where, as part of the metastatic cascade of solid tumors, single/clusters of cancer cells detach from the primary tumor, intravasate into the blood stream, followed by extravasation and homing to distant organs. Here, if the secondary site does not foster immediate growth, disseminated tumor cells (DTCs) switch to a low proliferative/metabolic state, also referred to as dormancy [25, 26] (Fig.1.5).

Considering that, between 10-90% (depending on tumor type and stage) of apparently cured resected solid cancers relapse at metastatic sites, with recurrences ranging from years to decades, point towards the presence of an invisible latent stage which allows DTCs to evade systemic administration of chemotherapeutics [27]. This difference in growth kinetics between primary and secondary sites, has prompted researchers to propose the microenvironment at the metastatic site to be responsible for such non-linearity, which might provide stimuli necessary to induced DDCs dormancy until either niche alterations or genetic aberrations trigger their awakening [27].

Unfortunately, the rarity and complexity associated with detection, isolation and analysis of DTCs in disease-free patients, have so far posed significant technical and ethical challenges to the advancement of cancer dormancy research [28]. These hurdles have called for an urgent need to develop in vitro culture systems able to reliably mimic this asymptomatic state, to finally enable scalable drug screening campaigns for the identification of promising target drugs. So far researchers have relied on different strategies (depending on tumor type and metastatic site) to induce dormancy either by using drugs, biochemical factors, niche cells or ECM-mediated mechanical confinement [29] (Fig.1.6).

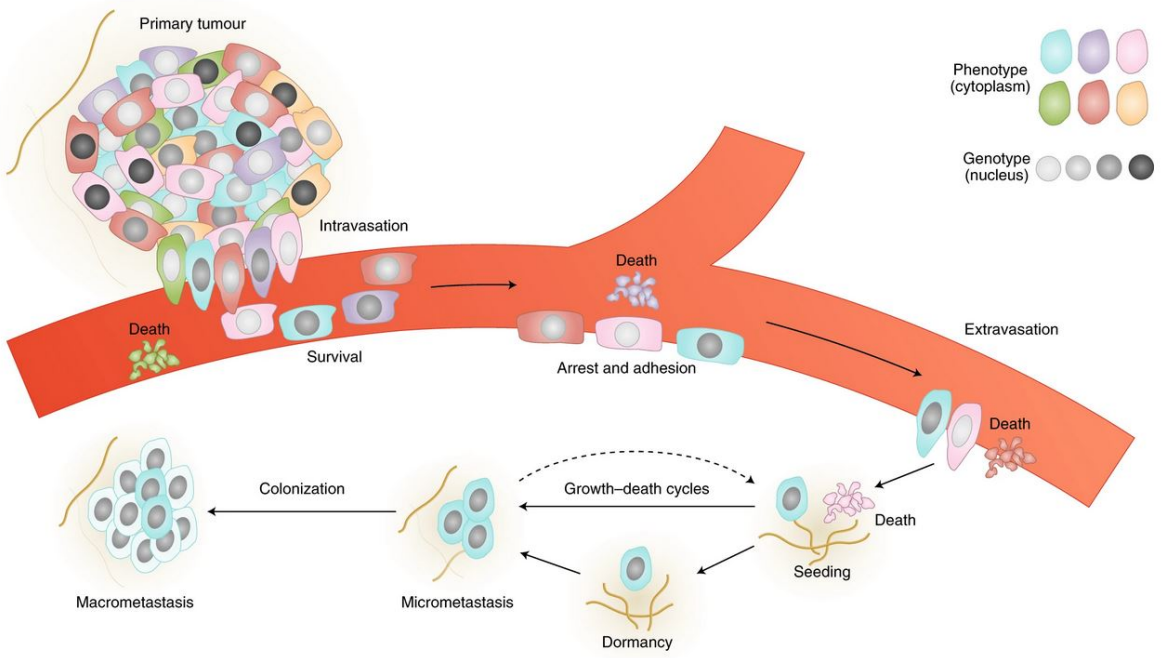

Figure 1.5: The metastatic cascade. Reproduced with permission from [25].

Earlier works investigating breast cancer cell (BCCs) dormancy have relied on commercially available basement membrane matrices, in which weakly metastatic BCCs were embedded and their proliferative phenotype assessed [30, 31]. Later on, depending on the niche meant to mimic, coculture of BCCs with different stromal cells were developed including osteoblasts [32], osteoclasts [33], neutrophils [34], peripheral blood mononuclear cells [35], liver stromal cells [36], lung alveolar cells [37] or bone marrow stromal cells together with endothelial cells [38, 39]. The latter reported particularly promising in vivo results, suggesting integrin inhibition as a potential adjuvant therapy approach to sensitize DTCs to chemotherapy [40]. Motivated by these results, a preclinical study assessing PI3K inhibition (a downstream kinase of integrin-β1) on preventing metastasis or reducing DTC burden was performed, with unsuccessful outcome [41], stressing again on the hurdles associated with clinical translation.

Others have focused on biochemical factors by treating BCCs with hypoxia inducing factors (CoCl2) [42, 43], fibroblast growth factor-2 (FGF-2) [44] or thrombospondin [38] to induce dormancy. More recently, recapitulating cancer growth arrest by immobilizing cancer cells via matrix-mediated mechanical confinement is gaining traction [29, 45, 46, 47]. Despite its simplicity, the versatility of this method allows tunable regulation of physical aspects of the microenvironment (i.e. ECM), enabling phenotypic mapping of cells at various stages of growth [48, 49]. Here, we leveraged a similar approach by developing ultraviolet (UV) light-initiated, thiol-ene-mediated, covalently-crosslinked alginate hydrogels, which generate mechanical confinement inducing growth arrest in BCCs. Briefly, systematic tuning of matrix stiffness, degradability (via MMP-degradable crosslinkers) and adhesion (via RGD cell adhesion peptide) enable generation of different fractions of cell populations with defined and controllable cell cycle status. Furthermore, RNA sequencing data of growth-arrested cells

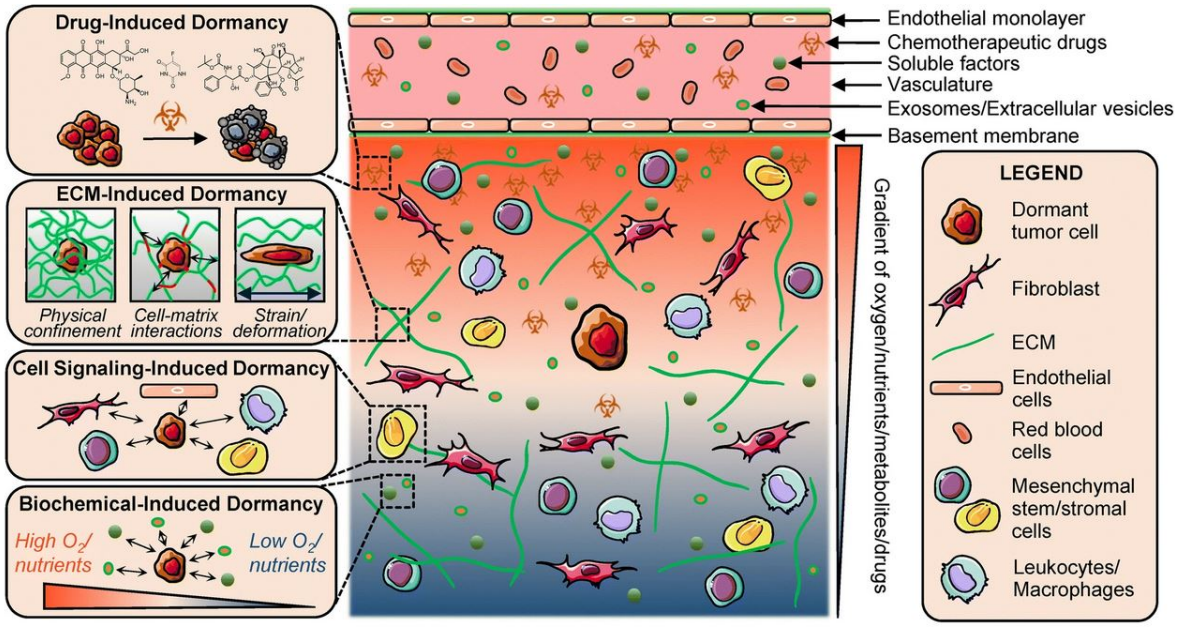

Figure 1.6: Modes of dormancy induction. Reproduced with permission from [29].

revealed several parallels with recent mRNA screening data of patient-derived-DTCs [50].

Importantly, we identified an underlying mechanism of growth arrest mediated by the stiffness-dependent nuclear localization of the transcription factor four-and-a-half LIM domains 2 (FHL2) protein, leading to a p53-independent expression of the cell cycle inhibitor p21Cip1/Waf1. Strikingly, upon downregulation of FHL2, cells in the quiescence-inducing matrix became sensitive to the mitosis-blocking chemotherapeutic Paclitaxel, suggesting a resistance-causing role. Despite its simplicity, we showed that mechanically-induced quiescence not only recapitulates several aspects of patient-derived DTCs and mouse models of metastasis, but can be used as a simple, fast and potentially scalable drug screening method to investigate large populations of single growth-arrested cells, known to be rare and inaccessible in large numbers from clinical settings. For more details, please refer to chapter 3 of this dissertation.

1.3 Cancer cell biophysics: a new readout for diagnostics

Intrinsic biophysical properties of cells have been shown to be valuable indicators of homeostatic functions [51], as well as pathological alteration [52]. Cell stiffness, for instance, has been reported to be a marker of stem cell differentiation [53] as well as cancer malignancy [54, 55]. Nonetheless, recent systematic studies comparing common techniques (i.e. atomic force microscopy, magnetic twisting cytometry, particle-tracking micro-rheology, parallel-plate rheometry, cell monolayer rheology, and optical stretching) used to assess cell mechanics indicated significantly different measurement values, even in the order of 100-1000 fold [56]. This calls for more reproducible methods to standardize cell mechanics measurements to enable objective assessment. A recently emerged and promising technique is optical Brillouin spectroscopy, which, unlike its counterparts, allows for fast, label-free, non-perturbative and non-contact measurements [57]. Its ability to map 3D viscoelastic properties at high resolution

has made Brillouin microscopy an attractive tool in the field of mechanobiology [58].

Nonetheless, most of the reported studies have either been conducted in suspended cells or in cells adhering to 2D substrates, neither of which is an authentic representation of cells' physiological state, where they are surrounded by neighboring cells or the ECM in a 3D context. To address this gap, we encapsulated cells in our 3D alginate hydrogels with varying stiffness and measured their intracellular mechanical properties under 3D confinement. We observed higher stiffness and viscosity for the nucleus compared to the cytoplasm. Interestingly, increasing hydrogel stiffness revealed higher stiffness and viscosity for both nuclei and cytoplasm of cells encapsulated in stiff versus soft 3D alginate hydrogels.

Another cell-intrinsic physical property holding important biological information is the cell's refractive index (RI), which has been reported to be linearly proportional to protein concentration and mass density (ρ) in most biological materials [59, 60]. Several physiological and pathological cell states (e.g. apoptosis [61], cell growth [62], dormancy [63] and aging [64]) have been recently observed to be associated with changes in ρ within the cell, mainly via a process of liquid-liquid phase separation [65]. Earlier optical studies investigating intracellular RI distribution on cells adhering to 2D substrates had reported higher RI for the nucleus compared to the cytoplasm [66, 67, 68, 69]. Nonetheless, recent reports with more advance imaging techniques such as quantitative phase imaging [70, 71], plasmon resonance [72], transport-of-intensity [73] and orientation-independent differential interference microscopy [74] have shown the opposite. Importantly, the higher ρ in the nucleus vs. the cytoplasm is robustly conserved throughout the cell cycle even when subjected to cytoskeletal or chromatin perturbations [75].

Analogous to cell mechanics, the majority of the studies reporting the cell refractive index have been performed on suspended cells or cells adhering to 2D substrates. To bridge this gap, we took advantage of our alginate hydrogels and a state-of-the-art combined optical-diffraction-tomography and epifluorescence microscope that allow fast, contact/label-free and high-resolution 3D mapping of intracellular ρ distribution. To our surprise, cells nuclei in 3D displayed higher ρ than the cytoplasm, as opposed to cells on 2D substrates, stressing again on the importance of accounting for the role of dimensionality in the interpretation of cellular responses.

The ability to visualize and quantify intracellular biophysical properties at the single-cell level with non-invasive techniques is a first and important step towards a better understanding of a wide variety of biological processes, in particular those associated with intracellular physical alterations such as in aging [64] or cancer progression [54, 55]. For more details, please refer to chapter 4 of this dissertation.

1.4 Organotypic model of breast cancer bone metastasis

Different strategies have been pursued in modeling cancer behavior: (i) a more minimalistic and simpler approach where the aim is to actively mimic a particular feature of the microenvironment or phenotype of cancer cells, as conducted in sections a-c (ii), or to replicate the tumor microenvironment with as many details as possible and monitor the spontaneous response of cancer cells. Despite its complexity, and therefore difficulties associated with dissecting the role of entangled parameters, the latter approach allows observation of cancer cells' behavior in a more unperturbed and physiologically relevant setting. For this purpose, we teamed up with Dr. Rosowski and his group, which had previously developed a bone-marrow-on-a-chip model for long-term culture of human hematopoietic stem and progenitor cells (HSPCs) in a 3D co-culture environment [76]. The system consists of a 3D hydroxyapatite-coated zirconium oxide scaffold pre-seeded with primary human mesenchymal stromal cells (MSCs) and the addition of human cord blood-derived multipotent HSPCs, genuinely resembling several molecular and structural features of the bone microenvironment (Fig.1.7). Importantly, the system allows preservation of HSPCs in their primitive, undifferentiated and quiescent state for several months, longer than any other known model reported so far.

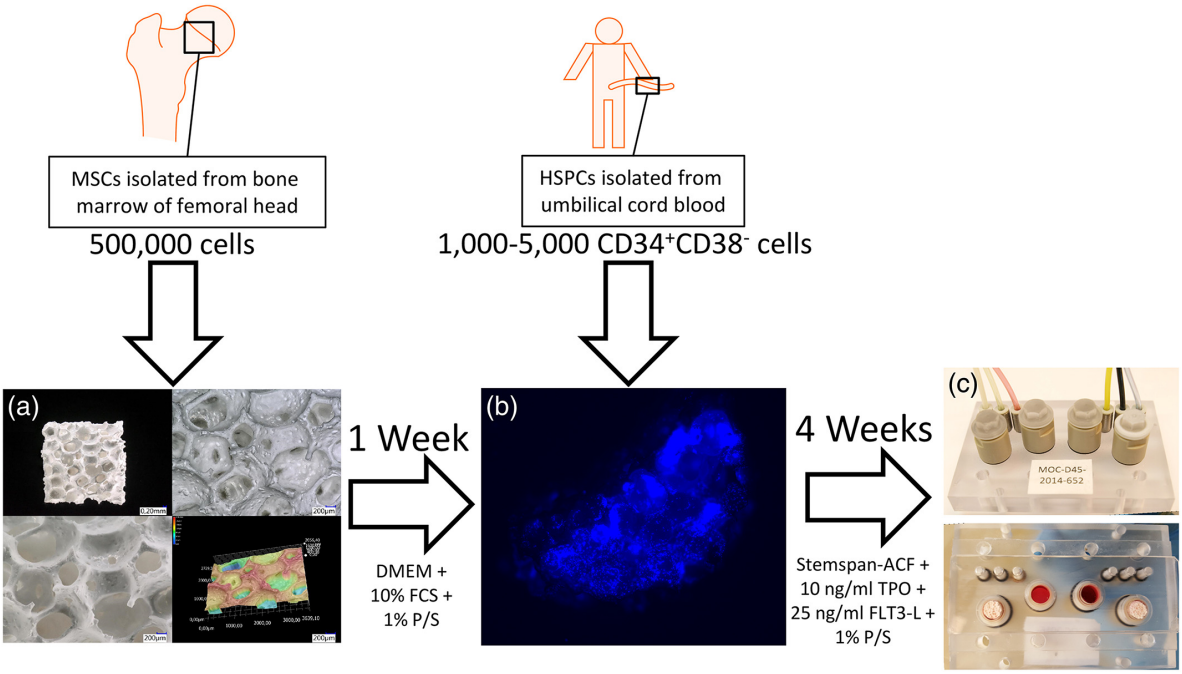

Figure 1.7: Schematic of bone marrow model. Blue staining represents DAPI nuclear signal of MSCs. Reproduced with permission from [76].

The similar quiescent state of HSCs and dormant DTCs has prompted researchers to suggest the existence of parallel governing mechanisms of growth arrest [77, 78]. Recent studies showing an increase in HSCs mobilization and differentiation after cancer cell dissemination [79, 80, 81], hints at a potential competition for occupying specific quiescence-inducing niches in the bone marrow. To investigate this, we included a breast cancer cell cycle reporter in the 3D bone marrow model and observed both BCCs and HSCs to be located within a web-like network of fibronectin, with the former preferentially tending towards a G0/G1 vs.

S/G2/M stage of the cell cycle, suggesting a potential quiescence-inducing role for the bone microenvironment. For more details, please refer to chapter 5 of this dissertation.

1.5 Thermodynamic metastability: a proxy of cancer dormancy

Research efforts to investigate cancer have historically weighed toward understanding molecular mechanisms and signaling pathways involved in the process, providing a local and specific form of description. Physics contribution, on the other hand, lies in its attempt to provide a more global narrative, independent from many details of the system. This approach has proved particularly useful when considering cancer, as several steps in its healthy-to-malignant transition, like epithelial-to-mesenchymal transition [82] or tumor invasion [83], resemble thermodynamic phase transitions seen in inert matter [84].

Aiming at providing a broader explanation for the role of the microenvironment in modulating differences in growth rate between cancer cells at primary tumor sites and disseminated cancer cells at secondary organs (explained in detail in section c), we leveraged concepts of stability and metastability occurring during phase transitions of growing droplets [85, 86, 87, 88, 89]. We postulated that cancer cells' (described as droplets) tendency to grow is driven by their interaction with two or more interfaces (i.e. different ECMs, cell-ECM, or cell-cell) with intrinsic energetic differences (contributed by surface and volume changes), such that the droplet would grow at the interface which is more energetically favorable. This is analogous to nucleation processes, well known from the thermodynamics of phase separation theory, which can happen either homogeneously, where the droplet exists within a single parent phase, or heterogeneously, where the droplet grows in contact with a foreign surface which lowers the overall interface between the nucleating droplet and the parent phase [84].

Looking at the growth kinetics of a droplet for both nucleation cases, revealed the emergence of "metastable" states, defined as a state of local (as opposed to global) energy minima, which we proposed can be considered as proxies of dormancy. The tendency of the droplet to remain in this energy valley (or dormant) or to overcome it, is influenced by microenvironmental fluctuations and perturbations which may or may not provide the energy required to overcome this energy valley (also known as energy barrier), thereby affecting the droplet's growth progression. Inspired by experimental data, here we simplistically modelled three distinct types of interactions: (i) cells adhering to a wetting flat surface in the form of a spherical cap (ii) a spherical droplet enclosed by an elastic sheath as a mechanical interpretation of extracellular matrix (ECM)-mediated confinement, and (iii) a spherical droplet with size-dependent limited growth due to lack of nutrients and oxygen, leading to cell apoptosis deep inside the tissue droplet. Interestingly, and in line with experimental and clinical data, we observed that metastable states are predicted only when physical aspects of the microenvironment are considered, that is adhesion and mechanical confinement and not in the case of lack of nutrients and oxygen.

Despite its simplicity, the proposed framework captures several aspects of cancer dormancy. However, this is not meant to replace molecular, cellular or genetic mechanisms, but to provide a more global level of description, where the microenvironment feeds information to cells and vice versa. For details, please refer to chapter 6 of this dissertation.

2

Thesis Structure

2.1 Overview

The thesis is based on four separate works, two of which led to distinct publications in peer-review journals, one being recently submitted, while the latter is currently being prepared for submission. As the works are largely independent and mainly performed in parallel, they will be presented in the most logical order irrespective of their chronological date of publication.

The first work **(P1)** embodies the bulk of the project, in which a quiescence-inducing platform was developed using thiol-ene crosslinked covalent alginate hydrogels, with extensive material and biological characterization.

In the second work [90] **(P2)**, stemming from a collaboration with the Guck lab at the time at TU Dresden, we optically quantified intracellular mass density and mechanics of breast cancer cells under 3D mechanical confinement using optical diffraction tomography and Brillouin microscopy. We further complement these findings with high resolution proof-of-concept data using cryo-FIB-SEM imaging of cells encapsulated in 3D hydrogels.

Overall, the data here illustrates the potential of using cryo-FIB-SEM to observe the detailed intracellular architecture of cells in a 3D environment in their most close-to-native condition.

In the third work, conducted in collaboration with Dr. Rosowski's lab at TU Berlin with the help of a dedicated master student, Ms. Sanem Özayral, we aimed at investigating the effect of the bone microenvironment on disseminated cancer cells in a more physiologically relevant system. The latter is mainly preliminary results requiring further analysis, which nevertheless provide additional insight into the role of the bone microenvironment on breast cancer metastasis. We therefore decided to selectively report only the most relevant and

reliable set of results in this case.

In the last work **(P3)** we proposed a physical framework based on nucleation theory where cancer dormancy can be viewed as a metastable state, the stability of which depends on microenvironmental cues.

2.2 Project-related publications

P1 Bakhshandeh et al., "Quiescence-inducing 3D-engineered matrix uncovers mechanosensitive and drug protective FHL2-p21 signaling axis", this work has been deposited in *bioRxiv* in January 2022 (https://doi.org/10.1101/2023.01.25.525382)

P2 Bakhshandeh et al., "Optical quantification of intracellular mass density and cell mechanics in 3D mechanical confinement", *Soft Matter*, 2021, 17, 853-862

P3 Microenvironment-mediated cancer dormancy: insights from metastability theory", *Proceedings of the National Academy of Sciences of the United States of America (PNAS)*, 2022 119 (1) e2111046118

3

Publication I: Quiescence-inducing 3D-engineered matrix uncovers drug protective signaling pathway of dormant cancer cells

3.1 Overview

The impetus for the first part of the project was to develop a quiescence-inducing platform to mimic the dormant state of a subset of disseminated cancer cells. We took advantage of a previously developed 3D culture system based on norbornene-modified alginate crosslinked with non-degradable crosslinkers using UV-initiated thiol-ene chemistry16. After extensive material and phenotypic characterization of the hydrogels and the growth-arrested cells, respectively, we performed RNA sequencing for cells retrieved from quiescence-inducing and proliferation-permissive platforms. These analyses revealed a mechanosensitive FHL2-p21 signaling axis mediating chemotherapy resistance in growth arrested cells, which we further investigated in preclinical mouse models of breast cancer metastasis and in human primary breast tumor biopsies.

3.2 Personal contribution

For this publication, I carried out the material synthesis, hydrogel fabrication and characterization, as well as in vitro and ex-vivo experiments with the support of all co-authors. Additionally, I evaluated the data, interpreted the results, generated the figures, and wrote the manuscript. RNA-seq data acquisition and analysis were performed by collaborators from Regensburg.

3.3 Publication notification

This work has been deposited in bioRxiv in January 2022 (https://doi.org/10.1101/2023.01.25.525382) and is currently under review in *Science Advances* (reuse permitted for preprint).

"Quiescence-inducing 3D-engineered matrix uncovers mechanosensitive and drug protective FHL2-p21 signaling axis"

Sadra Bakhshandeh, Hubert M. Taïeb, Adithi R. Varadarajan, Sarah M. Hücker, Xin Lu, Daniela S. Garske, Sarah A. E. Young, Jörg Contzen, Manfred Gossen, Stefan Kirsch, Jens Warfsmann, Kamran Honarnejad, Christoph A. Klein, Amaia Cipitria.

Quiescence-inducing 3D-engineered matrix uncovers mechanosensitive and drug protective FHL2-p21 signaling axis

Sadra Bakhshandeh[1], Hubert M. Taïeb[1], Adithi R. Varadarajan[2], Susanna M. Lissek[3], Sarah M. Hücker[2], Xin Lu[2], Daniela S. Garske[1], Sarah A. E. Young[1], Jörg Contzen[4, 5, 6], Manfred Gossen[5, 6], Stefan Kirsch[2], Jens Warfsmann[2], Kamran Honarnejad[2], Christoph A. Klein[2, 3], Amaia Cipitria[1, 7, 8*]

[1]Department of Biomaterials, Max Planck Institute of Colloids and Interfaces, Potsdam, Germany

[2]Division of Personalized Tumor Therapy, Fraunhofer Institute for Toxicology and Experimental Medicine, Regensburg, Germany

[3]Experimental Medicine and Therapy Research, University of Regensburg, Regensburg, Germany

[4]Department of Experimental Neurology, Charité - Universitätsmedizin Berlin, Berlin, Germany

[5]Institute of Active Polymers, Helmholtz-Zentrum Hereon, Teltow, Germany

[6]Berlin-Brandenburg Center for Regenerative Therapies, Charité Campus Virchow Klinikum, Berlin, Germany

[7] Group of Bioengineering in Regeneration and Cancer, Biodonostia Health Research Institute, San Sebastian, Spain

[8]IKERBASQUE, Basque Foundation for Science, Bilbao, Spain

Correspondence to: amaia.cipitria@mpikg.mpg.de

Abstract

Resected tumors frequently relapse with distant metastasis, despite systemic treatment. Cellular quiescence has been identified as an important mechanism underlying such drug resistance enabling late relapse. Nonetheless, hurdles associated with detection and isolation of disseminated cancer cells (DCCs) in disease-free patients urge the need for *in vitro* models of quiescent cells suited for drug screening campaigns. Here, we explore a quiescence-inducing 3D-engineered matrix based on ultraviolet light-initiated thiol-ene-crosslinked alginate hydrogels, which generate mechanical confinement and induce growth arrest and survival against chemotherapy in cancer cells. As underlying mechanism, we identified stiffness-dependent nuclear localization of the four-and-a-half LIM domains 2 (FHL2) protein, leading to p53-independent high $p21^{Cip1/Waf1}$ nuclear expression, validated in murine and human tissue. Suggestive of a resistance-causing role, cells in the quiescence-inducing matrix became sensitive against chemotherapy upon FHL2 downregulation. Thus, our biomaterial-based approach will enable systematic screens for novel compounds suited to eradicate potentially relapsing, dormant cancer cells.

Introduction

Most cancer-associated deaths are due to metastasis, with eventual relapses spanning from years to decades despite adjuvant and chemotherapies(*1*, *2*). Cancer dormancy has been described as one of the main mechanisms of evasion, which, due to its asymptomatic nature, poses significant technical and ethical challenges for the identification, isolation and investigation of DCCs(*3*). This calls for reliable *in vitro* culture systems to mimic this geno/phenotypic state to finally enable scalable drug screening campaigns for the identification of promising target drugs. Material-based, bioengineered-niche approaches have been previously pursued to induce and/or preserve the quiescence of astrocytes(*4*) and muscle stem cells(*5*), maintain neural progenitor(*6*) and hematopoietic cell stemness(*7*), investigate mechanical memory(*8*) and differentiation of stem cells(*9*), as well as to investigate cancer cell cycle progression(*10*, *11*). Here, we harnessed a similar approach by developing ultraviolet (UV) light-initiated, thiol-ene-mediated, covalently-crosslinked alginate hydrogels, which through 3D mechanical confinement induce and maintain large populations of single breast cancer cells in a growth-arrested state. We showed that artificial quiescence-inducing matrices select for distinct populations of growth-arrested cells, with cells in the G_0/G_1 cell cycle phase being more resistant to confinement. Combined with RNA sequencing, we revealed a stiffness-dependent nuclear localization of the four-and-a-half LIM domains 2 (FHL2) protein as an underlying mechanism of quiescence, leading to a p53-independent high $p21^{Cip1/Waf1}$ nuclear expression, validated in murine and human tissue. Suggestive of a growth arrest-mediated drug resistance, quiescent cells became sensitive against drug treatment upon FHL2 downregulation. This biomaterial-based approach with mechanically-induced quiescent cancer cells offers therapeutic applications as a simple and scalable method, to investigate large populations of dormant cancer cells, otherwise rare and inaccessible in large numbers from clinical settings, and for high throughput drug screens of novel compounds to eradicate potentially relapsing DCCs.

Results

3D mechanical confinement via covalently-crosslinked alginate yields distinct fractions and populations of growth-arrested cells based on hydrogel composition

Building on the now widely acknowledged role of the ECM in cancer induction and progression(*12*, *13*), we employed a versatile ECM-mimicking hydrogel encapsulation approach to investigate the effect of ECM-mediated 3D mechanical confinement on cell cycle progression. We used ultraviolet (UV) light-initiated thiol-ene-crosslinked alginate(*14*), an inherently inert hydrogel (non-cell adherent and non-degradable) which allows for selective modulation of parameters such as stiffness, cell adhesion or degradation (Fig.1a). Cells were encapsulated in the presence (or absence) of adhesion ligands (RGD), within degradable matrix metalloproteinases (MMP)-sensitive or non-degradable dithiothreitol (DTT)-crosslinked hydrogels (Fig.1a and Supp.Fig.1). The stiffness of the hydrogels ranged between 0.5-13kPa as a function of crosslinker concentration (Fig.1b). To monitor cell cycle progression in real-time, we genetically modified widely-used triple-negative MDA-MB-231 (MDA231) and luminal MCF7 breast cancer cell (BCC) lines, known to disseminate to secondary organs in *in vivo* models, with the fluorescence-ubiquitination-based cell cycle indicator 2 (FUCCI2)(*15*, *16*) (Fig.1c). Time-lapse imaging of MDA-FUCCI2 cells encapsulated within alginate hydrogels of different stiffness (soft for 1kPa and stiff for 10kPa), adhesion and degradation properties, as well as on two-dimensional tissue culture plastic (2D-TCP) and in 3D Matrigel, was performed over a period of 4-5 days, followed by quantification of the cell cycle state at the experimental endpoint (Fig.1d, Supp.Mov.1). 3D Matrigel and 2D TCP yielded highly proliferative (Ki67+) and metabolically active cells (resazurin reduction) in the form of 3D spheroids and single cells, respectively (Fig.1d, Supp.Fig.2b,d). Cells within the 3D alginate groups remained mostly as single cells, with the highest fraction of $S/G_2/M$ phase cells being in the soft

group, while the stiff adherent (RGD) and degradable (MMP-sensitive) groups displayed a lower percentage of S/G_2/M and higher fraction of G_0/G_1 phase cells (Fig.1d). 3D alginate stiff yielded the highest fraction of cell cycle-arrested cells over 5 days (Fig.1d), while preserving high viability (Supp.Fig.2a). Interestingly, we noticed different sub-populations of cell cycle-arrested cells as a function of the expression (or lack of) of the licensing factor cdt1 (G_0/G_1 cdt1+/–; Fig.1d, Fig.2a, Supp.Mov.2-7). A recent mapping of protein dynamics during cell cycle progression revealed that the expression patterns of cdt1 is highly dynamic and distinctive of different levels of quiescence, with the lowest (cdt1-) identifying a longer time spent in a growth-arrested state(*17*). MDA231 cells in quiescence-inducing alginate stiff hydrogels displayed higher resistance to chemotherapy compared to cells in proliferation-permissive 3D Matrigel (Supp.Fig.2e) and, reminiscent of post-therapeutic relapses in clinical settings, were able to exit the growth-arrested state and resumed proliferation when retrieved from the hydrogels and seeded on 2D TCP (Supp.Fig.2c).

Dynamics of cell cycle and viability correlation reveal that G_0/G_1 cells are substantially more resistant to 3D mechanical confinement than cells in the S/G_2/M phase

To understand the dynamics of 3D mechanical confinement-induced growth arrest, we tracked single-cell MDA-FUCCI2 fluorescence intensity (f.i.) within stiff hydrogels. Cells which were in the G_0/G_1 state at the time of encapsulation, had either lost (cdt1-) (Fig.2a1, b) or kept (cdt1+) (Fig.2a2, b) their fluorescence by the end of the experiment. On the other hand, in almost every cell initially in the S/G_2/M phase, we observed a decrease in f.i. within the first few hours after encapsulation (Fig.2a3, b). By correlating cell's FUCCI2 imaging and *in situ* viability staining (calcein+; Fig.2c), we revealed that the vast majority of viable cells at day 5 were initially in the G_0/G_1 cycle state (Fig.2c, d). We validated these results for MCF7-FUCCI2 cells (Fig.2d), confirming that cells in the G_0/G_1 state are more resilient to 3D mechanical confinement compared to cells in the S/G_2/M phase.

Gene expression analysis of cells in quiescence-inducing versus proliferation-permissive 3D matrices

We then looked into the gene expression of quiescence-induced cells in more details. RNA-sequencing on live cells retrieved from 3D alginate stiff (Fig.3a) revealed enrichment of cell cycle and retinoblastoma-associated molecular pathways (Fig.3b-d, Supp.Fig.3, 4), as well as regulation of senescence, autophagy and apoptosis processes when compared to cells retrieved from 3D Matrigel. In particular, we noticed strong enrichment of inflammatory response-associated pathways (TNF, NFkB and IL-17 signaling) and DNA damage stimuli response (ATM, p53 and miRNA regulation of DNA damage) (Fig.3b-e, Supp.Fig.3, 4). Intriguingly, we noticed that despite increased mRNA expression of *cdkn1a* (coding for the p21 protein) upon culture in 3D alginate stiff compared to 3D Matrigel, the levels of its key upstream cell cycle regulator *p53* is lower (Fig.3e), hinting to a potential p53-independent mechanism regulating p21 expression(*18*). This matches the lack of correlation of p53-p21 observed in patients with estrogen receptor negative (ER-) breast cancer (Supp.Fig.5). Noticing the particularly high levels of p21 (*cdkn1a*) expression among other genes in 3D alginate (Fig.3e) and its relevance in cell cycle regulation, we decided to investigate the role of p21 in regulating mechanically-induced cancer cell cycle arrest in more detail.

p21 and FHL2 localization in 3D matrices is stiffness-dependent and FHL2 mediates p21 localization and Ki67 expression

Despite the now widely acknowledge advantages of 3D vs. 2D culture systems in studying physiologically-relevant cellular processes(*19*), the role of dimensionality in the expression, localization and function of p21 remains underexplored. This is of utmost importance considering that in cancer cells the p21 oncogenic vs. suppressing function is known to depend on its level of expression and intracellular localization(*18*). We therefore assessed these features across different

3D culture systems, focusing on soft and stiff 3D alginate hydrogels. As expected, the fraction of p21-positive cells was significantly higher in 3D alginate stiff compared to soft or 3D Matrigel (Supp.Fig.6), accompanied by strong enrichment of DNA repair-associated pathways (Fig.4a-b and Supp.Fig.7). Importantly, cells in 3D alginate stiff revealed a significantly higher nuclear vs. cytoplasmic (nuc./cyto. ratio) localization of p21 compared to the soft group, together with a lower fraction of proliferative cells (Ki67 expression) (Fig.4c). Inhibiting MEK/ERK, PI3K/Akt and JNK, as some of the major signaling pathways regulating cell proliferation, displayed a strong effect on p21 localization (Fig.4d).

Previous work on 2D cultures had found that, in MDA231 cells, p21 is induced in response to treatment with DNA damaging drugs such as doxorubicin, and this is mediated by FHL2 in a p53-independent manner(*20*). Notably, FHL2 was shown to be stably expressed in only a small subset of BCC lines with MDA231 being among the highest(*20*). Nonetheless, FHL2 localization and functional role in physiologically-relevant 3D cultures had not been addressed. We therefore investigated the nuc./cyto. ratio of FHL2 in 3D stiff compared to soft alginate hydrogels. Surprisingly, and in stark contrast to 2D cultures where soft 2D substrates lead to nuclear accumulation of FHL2(*21*), we observed a significantly higher expression and nuc./cyto. ratio of FHL2 in 3D stiff compared to soft alginate hydrogels (Fig.4e). This effect was mitigated by inhibiting MEK/ERK and PI3K/Akt pathways but not JNK (Fig.4f). Importantly, knock-down of FHL2 revealed a decrease in p21 nuclear localization in 3D stiff hydrogels (Fig.4g), as well as an increase in proliferation activity (Ki67; Fig.4f), pointing to FHL2 being upstream of p21. The correlated expression of *cdkn1a* and *FHL2* is also found in tumor samples of patients with ER- breast cancer (Supp.Fig.8).

FHL2 knockdown sensitizes cells to chemotherapy

We then investigated whether FHL2 knockdown sensitizes cells to chemotherapy. FHL2-silenced cells in 3D alginate stiff displayed higher viability and metabolic activity than wild-type MDA231 when untreated (vehicle) (Fig.5a). Upon exposure to mitosis-blocking chemotherapeutic Paclitaxel in a concentration-dependent fashion (0.01-0.5mM), a significant reduction in viability and metabolic activity was observed (Fig.5a), pointing to a chemo-sensitizing effect upon FHL2 knockdown.

FHL2 expression and localization in murine tissue, human primary breast tumor and human early DCCs

Finally, to assess the implications for human disease, we investigated FHL2 expression and localization in a preclinical mouse model with metastatic breast cancer and in human primary tumor biopsies. Remarkably, single quiescent MDA231 cells (bone-tropic 1833 subclone) spontaneously disseminated to the mouse femur revealed nuclear FHL2, as opposed to proliferative clusters with cytoplasmic FHL2 (Fig.5b, Supp.Fig.9). Similarly, human tissue biopsies of breast tumor reveal a primarily cytoplasmic/membranous localization of FHL2 (Fig.5c), matching our observation in 3D Matrigel (Fig.5d). Furthermore, we investigated human early DCCs of an M0 breast cancer patient, with only microscopy evidence of metastasis and no clinical or radiographic evidence of distant metastasis. Disseminated breast cancer cells (cytokeratin+, an epithelial marker) in the sentinel lymph node displayed varying FHL2 signal intensity suggestive of functional heterogeneity (Fig.5e, f).

To sum up, ligand-rich, proliferation-permissive microenvironments maintain FHL2 in the membranous regions, whereas in low or non-adherent microenvironments the increase in mechanical confinement (stiffness) results in FHL2 translocation to the nucleus, leading to high p21 nuclear expression, cell cycle arrest and chemo-resistance (Fig.6).

Discussion

In this study, we use a 3D quiescence-inducing engineered matrix to investigate a mechanism of chemoresistance in mechanically-induced dormant BCCs. Systematic tuning of three variables (adhesion via RGD, degradability through MMP-sensitive crosslinkers and stiffness) enables generation of different fractions of cell populations with defined and controllable cell cycle status. Here, we harness this approach and reveal a stiffness-dependent nuclear localization of the FHL2 protein which leads to p53-independent nuclear expression of p21 as a quiescence and resistance-conferring mechanism. We further show that the expression and localization of both p21 and FHL2 in 3D to be strikingly different than previously-reported 2D studies, where FHL2 shuttling to the nucleus was shown to be substrate rigidity-dependent, such that on soft surfaces (as opposed to stiff substrates where mechanical tension is higher) it would translocate to the nucleus and induce p21 expression(*21*). In contrast, in 3D matrices ligand-rich environments such as in basement membrane matrices or primary breast tumor sites, FHL2 accumulates in adhesion sites(*21*), whereas loss of adhesion (occurring in intrinsically non-adherent materials such as alginate), results in FHL2 release from sub-membranous regions and shuttling to cytoplasmic (soft alginate) and nuclear (stiff alginate) regions. This cascade leads to p21 nuclear expression, cell cycle arrest and drug resistance for the latter (Fig.5e). Such dimensionality-dependent behavior has been similarly reported for YAP mechanotransduction in the context of breast tumor progression(*22*) and stem cell fate(*23*). Thus, it is critical to take into account the context-dependent role of the FHL2-p21 signaling axis, given its potential dual oncogenic vs. suppressive function(*18*, *24*). Notably, omission of adhesion ligands in our quiescence-inducing matrix was intentional, stemming from recent *in vivo* observations(*25*) where single DCCs were shown to reside in a dormant state with expressed but not engaged integrin receptors. Other studies have similarly observed DCCs expressing low levels of adhesion molecules(*26*), and integrin activation being a central mediator leading to their awakening(*26–29*).

FHL2 has been previously shown to concentrate at RNA polymerase (Pol) II sites(*21*), inducing c-Jun, IL6 and IL8 transcription. This is reflected in our sequencing data by the strong enrichment of RNA Pol II associated genes, with JUN, IL6 and IL8 being among the top ten (out of 9427) differentially regulated genes in the alginate stiff group (Fig.3b-e). This is in line with a recent study showing IL6 pathway activation in patient-derived early disseminated BCC in bone marrow(*30*).

To further support our findings, we investigated breast cancer cells disseminated to the bone in a metastasis mouse model, human tissue biopsies of primary breast cancer and early DCCs of an M0 breast cancer patient. Here we noted nuclear FHL2 localization in single dormant DCCs (Fig.5b) as opposed to cytoplasmic FHL2 corresponding to high proliferation activity (Ki67+) in a mouse model of breast cancer metastasis (Fig 5b). Likewise, cytoplasmic/membranous FHL2 is observed in human primary breast tumor biopsies (Fig.5c) matching the findings of proliferating cancer cells in 3D Matrigel (Fig. 5d). This is in agreement with screenings of normal and malignant human breast tissues revealing higher FHL2 expression for the latter, as shown in previous studies(*20*, *31*) and UALCAN database, while high FHL2 expression in ER- patients is associated with lower relapse-free survival rate (Supp.Fig.10). A number of disseminated breast cancer cells (cytokeratin+) were found in the sentinel lymph node both as single cells (Fig. 5e) and within cell clusters (Fig. 5f). We noted a substantial heterogeneity among the DCCs, further supporting the notion that various phenotypes exist in patients that may require different targeting approaches.

To conclude, we identify a stiffness-mediated FHL2 signaling mechanism in 3D bioengineered matrices inducing breast cancer cell quiescence and drug resistance, which recapitulates several aspects of patient-derived DCCs and mouse models of metastasis. Further, this approach can be exploited to generate large populations of single growth-arrested cells for simple,

fast and potentially scalable drug screening, since these are known to be rare and inaccessible in large numbers from clinical settings.

Materials and Methods

Synthesis of peptide-crosslinked alginate hydrogels

Norbornene-modified alginate hydrogels with thiol-ene crosslinking were synthesized as previously described(*32*). Briefly, high molecular weight (265 kDa; HMW), high guluronic acid, sodium alginate (Pronova MVG; NovaMatrix) was dissolved at 1% w/v in 0.1 M 2-(N- morpholino)ethanesulfonic acid (MES; Sigma-Aldrich), 0.3M NaCl (EMD Millipore) buffer (pH 6.5) overnight at room temperature. N-hydro-xysuccinimide (NHS; Sigma-Aldrich), followed by 1-ethyl-3-(3-dimethylami-nopropyl)-carbodiimide hydrochloride (EDC; Sigma-Aldrich) were added drop-wise at 5000 molar equivalents to the alginate solution while stirring. To functionalize the alginate backbone with norbornene functional groups, 5-norbornene-2-methylamine (TCI Deutschland GmbH) was added at a theoretical degree of substitution (DStheo) of 300 molecules per alginate chain. The final concentration of both reactions was 0.6% w/v and was run while stirring at 700 rpm at room temperature for 20 h. Next, the solution was quenched by adding hydroxylamine (Sigma-Aldrich), followed by dialysis (Spectra/Por 6, MWCO 3.5 kDa; Spectrum) against a salt gradient (6 g/L to 0 g/L; Sigma-Aldrich) in ddH_2O for 3 days with 3-4 changes per day. The solution was then purified with activated charcoal (Sigma-Aldrich), sterile-filtered (0.22 µm; Steriflip-GP; Merck) and lyophilized. To assess the actual degree of substitution, NMR measurements were performed using an Agilent 600 MHz PremiumCOMPACT equipped with Agilent OneNMR Probe (256 scans), with samples dissolved at a final concentration of 1.5% w/v in deuterium oxide (D_2O) (Supp. Fig 1b, c).

Casting of peptide-crosslinked alginate hydrogels

For hydrogel casting, the VPMS↓MRGG sequence was chosen as the enzymatically-degradable peptide crosslinker (↓ denotes the MMP cleavage site), ordered from WatsonBio Sciences at 98% purity with trifluoroacetic acid removal (Supp. Fig 1d). Double-cysteine containing dithiothreitol (DTT, Sigma-Aldrich, 43816) was used as the non-degradable crosslinker. Before casting, norbornene-modified alginate and the photoinitiator (Irgacure 2959; Sigma-Aldrich) were dissolved in phosphate-buffered saline (PBS) overnight at 50 °C under shaking. Alginate and photoinitiator concentrations were kept at 2 and 0.5% w/v respectively. The concentration of the crosslinker was changed to yield hydrogels with different mechanical properties. After mixing, the solution was pipetted with positive-displacement pipettes on a glass plated and covered with a dichloromethylsilane-coated glass slide (≥99.5%; Sigma-Aldrich). To initiate thiol-ene crosslinking, the mixture was exposed to UV light (365 nm at 10 mW/cm^2, OmniCure S2000) by placing the gel sheet in a custom-built curing chamber for 10 min. Gels were then punched out using biopsy punches of 4-6 mm (Integra Miltex) and washed with PBS until further use. To render norbornene-modified alginate adherent, a thiol-containing RGD sequence (CGG- GGRGDSP; Peptide 2.0) was added to the gel precursor mix (at 0.95 mM) to bind residual norbornene groups via UV-mediated thiol-ene chemistry. For 3D cell encapsulation, a cell suspension ($5x10^5$ cells/ mL) was added to the precursor solution and mixed before UV exposure. Matrigel (356237, Corning) was used at 100% w/v concentration (~ 10mg/mL).

Mechanical characterization

Rheology measurements were performed to calculate the elastic modulus (E) of pre-formed gels. Norbornene-modified alginate (2% w/v) hydrogels with different stiffness were cast by changing the DTT crosslinker concentration (0.01-1 mg/mL). After gel equilibration overnight in PBS, frequency sweep measurements were performed from 0.01 to 10 Hz at 1% shear strain with an 8 mm parallel plate (PP08, Anton Paar) using a rheometer (Physica MCR 301; Anton Paar),

while keeping the temperature at 25 °C with a Peltier cooling module. The initial E modulus was then calculated as follows: $E = 2G(1 + \vartheta)$ and $G = \sqrt{G'^2 + G''^2}$ where G, G' and G'' are the shear, storage and loss moduli, respectively, and ϑ the Poisson's ratio with a value of 0.5 for hydrogels(*33*).

Cell culture

MDA-MB-231 (HTB-26; ATCC), MDA-MB-231-1883 BoM (provided by Dr. Joan Massagué and purchased from the Antibody and Bioresource Core Facility of the Memorial Sloan Kettering Cancer Center, USA. The subclone 1833 is a bone tropic human cell line deriving from a metastasis formed by MDA-MB-231 TGL cells hosted in a mouse(*34*, *35*),which in turn are MDA-MB-231 (HTB-26; ATCC) human epithelial breast cancer cells stably transduced with a lentivirus expressing a triple-fusion reporter(*36*)) and MCF-7 (HTB-22; ATCC) human breast cancer cell lines were cultured in low glucose Dulbecco's Modified Eagle's Medium (D6046; Sigma-Aldrich) with 10% v/v fetal bovine serum (S0615, Sigma-Aldrich) and 1% penicillin/streptomycin (Gibco). For MCF-7 cells, 0.1% insulin (I1882, Sigma-Aldrich) was added. Cells were then incubated in a 5% CO_2 environment at 37 °C and passaged every 3-5 days.

Viability and metabolic activity characterization

Live and dead cells were stained with 1.6 mM calcein AM (C125400; TRC) and 4 mM ethidium homodimer-1 (EthD-1 L3224; ThermoFisher), respectively. To measure metabolic activity, Presto blue (ThermoFisher) was used. Briefly, after 1 and 7 days of incubation, cell culture medium was replaced with 10% Presto blue reagent in DMEM and the plate incubated for at least 4 h at 37 °C. Next, 100 µL of the supernatant was transferred to a black 96 well plate (655892, Greiner Bio-one) and fluorescence emission was measured at 590 nm (Cytation5, BioTek). ATP concentration was measured using CellTiter-Glo (Promega) according to the manufacturer's instruction. Briefly, a 1:1 volume of reagent and culture medium was added to each sample of a black 96 well plate (655892, Greiner Bio-one), shaken for 10 min at room temperature, and allowed to equilibrate for another 20 min before measuring bioluminescence signal (Cytation5, BioTek).

Lentiviral particle production, transduction and generation of FUCCI2 breast cancer cell lines

As previously reported(*37*), FUCCI2 vectors mCherry hCdt1(30/120)/pCSII EF MCS (DDBJ/EMBL/GenBank, AB512478) and mVenus hGeminin(1/100)/pCSII EF MCS (DDBJ/EMBL/GenBank, AB512479) were purchased from the Riken Brain Science Institute (Japan) and used to generate lentivirus particles by co-transfecting HEK 293TN cells (System Biosciences) with packaging (psPAX2, Addgene plasmid, #12260) and envelope (pMD2.G (Addgene plasmid, #12259) plasmids. The supernatant was collected by centrifuging (Beckman L7-55 with SW32Ti rotor) at 22,000 rpm for 3h at 4 °C. MDA-MB-231 and MCF-7 breast cancer cell lines were first transfected with mVenus hGeminin (1/110) (multiplicity of infection (MOI) of six and five, respectively) followed by mCherry hCdt1 (30/120) at an MOI of three. Verification of successful transduction and subsequent sorting of stably expressing mVenus and mCherry cell lines were perform using flow cytometry (FACSAriaTM II, Becton Dickinson).

Inhibition, RNA interference and drug response experiments

For inhibition experiments, the following small molecule and inhibitors were used: MEK/ERK inhibitor PD98059 (10 mM, Focus Biomolecules), JNKinhibitor SP600125 (10 mM, Focus Biomolecules) and PI3K/Akt inhibitor LY294002 (10 mM, Focus Biomolecules). The inhibitors were mixed with culture medium and refreshed every 2-3 days. To knock down FHL2, MDA-MB-231 cells were transfected with two different FHL2-targeting small interfering RNAs (Silencer siRNA, Invitrogen) or non-targeting siRNA (Stealth RNAi negative control, Invitrogen) using Lipofectamine RNAiMAX Reagent (Invitrogen), diluted in Opti-MEM reduced serum

medium (Gibco) for a final concentration of 10-20 nM. Cells were transfected 2-3 days before encapsulation following manufacturer's instructions. To assess MDA-MB-231 response to chemotherapy, Paclitaxel (Tokyo Chemical Industry) was diluted at 0.01, 0.1 and 0.5 mM and added to the culture medium after 3-5 days post-encapsulation for a drug treatment of 2 days. The highest concentration tested contained around 1% (v/v) of DMSO, which was used as vehicle medium and didn't show any negative effect on cell viability.

Immunofluorescence staining

Gels with encapsulated cells were washed (3x) with PBS and fixed with 4% paraformaldehyde (PFA, Boster, #AR1068) for 30 min at room temperature, (3x) washed with 3% w/v bovine serum albumin (BSA, Sigma Aldrich), permeabilized with 0.1 % w/v Triton X 100 (Sigma-Aldrich, #T8787) for 15 min with a final washing (3x) step with 3% BSA. Whole-mount primary antibody staining was performed at 4 °C overnight, diluted in a 3% BSA+0.1% Triton X 100 buffer solution under mild shaking. The gels were then washed (3x) with 3% BSA and incubated with secondary antibody at 4 °C overnight with the same dilution buffer under mild shaking. The samples were finally imaged after a last washing step with PBS (3x). The primary antibodies and respective concentrations used in this study are the following: anti-Ki67 (2 µg/mL, ab15580, abcam), anti-$p21^{Cip1/Waf1}$ (0.48 µg/mL, 2947S, Cell Signaling), anti-FHL2 (0.5 µg/mL, HPA006028, Sigma/Prestige Antibodies). The secondary antibodies are: Alexa Fluor 405 (10 µg/mL, ab175651, abcam) and Alexa Fluor 647 (4 µg/mL, A21244, Invitrogen). To stain for nucleus and cytoskeleton, DAPI (1:1000, Roche) and Alexa Fluor 488 Phalloidin (1:50, Invitrogen) were used.

Immunoblot

Cells were first lysed with RIPA buffer (Abcam) for 5 min on ice and then collected in Eppendorf tubes. Protein concentration was calculated following Bradford assay (Bradford reagent, Sigma-Aldrich). A 1:50 mixture of β-mercaptoethanol (Acros Organics) and 2x Tricine sample buffer (Bio-Rad) was added at a 1:1 volume to the cell lysates. The mixture was then heated to 95 °C for 5 min and loaded into pre-cast polyacrylamide gels (Mini-PROTEAN TGX, Bio-Rad) for electrophoresis in TGS buffer (Bio-Rad) at 100 V for 30 min, then 200 V for 30 min (Mini-PROTEAN Tetra System, Bio-Rad). Proteins in the gels were then blotted onto to a PVDF membrane (BioTrace, PALL) at 150 V for 90 min in ice-cold transfer buffer (1:5 volume of 100% Methanol in TGS buffer). Next, the membrane was transferred to TBST buffer (150 mM NacL, 20 mM Tris-base, 0.1% Tween20), blocked in 5% BSA in TBST buffer for 1 h under gentle shaking, washed in TBST (3x) and incubated with primary antibodies diluted in 1% BSA in TBST overnight at 4 °C. After washing with TBST (3x), the membrane was incubated with an HRP-linked secondary antibody for 1 h at room temperature, after which the chemoluminescence substrate (SuperSignal West Pico PLUS, Thermo Scientific) was added before visualizing it with a blot imager (G:BOX Chemi XX6/XX9, Syngene). GAPDH (1:1000, 2118, Cell Signaling) was used as housekeeping gene and HRP-linked (1:1000, 7074, Cell Signaling) as secondary antibody.

Cell retrieval from 3D gels

For RNA sequencing, MDA-MB-231 cells were retrieved from 3D alginate stiff, soft and 3D Matrigel. Briefly, alginate hydrogels were incubated with alginate lyase (2mg/mL, Sigma Aldrich, A1603) in HBSS (ThermoFisher, 14185045) for 30 min at 37 °C with three mixture steps every 10 min. For Matrigel, pre-cooled (4°C) HBSS was added and mixed for 5-10 min at room temperature, followed by incubation with Trypsin/EDTA (0.05%/0.02%, PAN Biotech, P10-023100) for 5 min at 37 °C. Cells were then washed twice with HBSS for 5 min. Next, retrieved cells were stained using a LIVE/DEAD fixable cell staining method (ThermoFisher, L34969) following manufacturer's instructions, and viable cells were sorted via FACSAria II flow cytometer (Becton Dickinson). Approximately 1500 sorted cells per sample were then lysed using pre-cooled

(4 °C) RLN buffer (0.05 M Tri-HCl pH 8.0, 0.14 M NaCl, 0.0015 M $MgCl_2$, 0.5 % v/v Nonidet P-40/IGEPAL (Sigma Aldrich, 56741) and 1000 U/mL RNase inhibitor (Promega, N2615), 0.001 M DTT) on ice for 5 min. The lysates were then centrifuged with a pre-cooled centrifuge for 2 min at 300 x g, the supernatants transferred to -80 °C and stored until further processing.

RNA sequencing and analysis

Samples were resuspended in 5 µl 1X NEBNext Cell Lysis Buffer of the NEBNext Single Cell/Low Input RNA Library Prep Kit (NEB, E6420). After 5 min incubation at RT, 2.5X RNA XP Clean Up Beads (Beckman Coulter, A63987) were added to the sample by pipetting up and down. Then, samples were incubated for 5 min at RT, the beads were pelleted on a magnet, the supernatant was removed, the samples were washed twice with 80% ethanol while remaining on the magnet, and finally the beads were resuspended in 8 µl nuclease-free water. The reverse transcription was conducted according to the manual of the NEBNext Single Cell/Low Input RNA Library Prep Kit in the presence of the beads. Next, the beads were pelleted on the magnet and the supernatant was used for the following PCR amplification as described in the manual. Twenty-one PCR cycles were applied, because the RNA concentration was below the detection limit of the Qubit RNA HS Assay Kit (Thermo Fisher, Q23852). The cleanup, quality control, fragmentation, and adapter ligation steps were performed as described in the kit manual. NEBNext Multiplex Oligos for Illumina (Index Primer Set 1) (NEB, 7335S) were used for the final PCR amplification. The fragment length distribution of the final libraries was determined using a 2100 Bioanalyzer Instrument (Agilent) with a High Sensitivity DNA kit (Agilent, 5067-4626). The libraries were quantified by qPCR with the KAPA Library Quantification Kit (Roche, KK4854). The nine samples were divided into two pools (one pool of four samples, the other of five samples) with equimolar amount. The pools were sequenced on an Illumina MiSeq with 2 x 150 bp.

After demultiplexing, raw FASTQ data were given to an in-house mRNA analysis pipeline 0.9.5.5. BBDuk 38.76(*38*) was used to trim the raw sequence data from soft, 3D matrigel and 3D alginate stiff, deleting any residual adapter sequences and low-quality bases at the ends of each read. BioBloom Tools 2.0.13(*39*) was used to decontaminate reads from the genomes Mus musculus (mm38), Escherichia coli (BL21), Mycoplasma pneumoniae (M129), Sphingobium sp. (SYK-6), Bradyrhizobium japonicum (USDA 110), Pichia pastoris (GS115), Malessia globosa (CBS 7966), Aspergillus fumigatus (Af293), and a set of viral genomes (RefSeq, 5k+ genomes). All reads that did not map exclusively to the transcriptome of hg38 (GENCODE version 27, GRCh38.p10) were labeled as potentially contaminated and were removed from further processing. FastQC 0.11.9(*40*) was used to evaluate sequence quality per sample before as well as after trimming and decontamination. In addition, all samples were examined as a collective with MultiQC 1.8(*41*). Following that, the cleaned sample reads were aligned to the hg38 reference genome using STAR 2.5.1b(*42*). Using featureCounts from Subread 2.0.0, uniquely mapping reads were counted per gene and sample(*43*). Further quality criteria were evaluated, including library complexity (using Preseq 2.0.3(*44*)) and the genomic origin of the reads and the 5'-3'-bias (both using QualiMap 2.2.2d(*45*)). The final counts table of 9 samples were utilized for differential expression analysis.

All the subsequent steps after the count tables were performed in R programming language 4.0.2 (2020-06-22)(*46*). Matrix table containing gene counts were visualized using Principle Component Analysis (PCA) and t-distributed stochastic neighbor embedding (t-SNE) clustering techniques. For PCA, raw counts were scaled and prcomp function from stats package was employed. tSNE plots were constructed using Rtsne 0.15(*47*). Subsequent steps including Quality Control (QC) analysis, filtering, normalization, feature selection, scaling, regression of unwanted variables were performed using Seurat package 4.0.2(*48*). Default parameters were taken for all used functions unless otherwise mentioned. Normalization was done using 'log.normalize' method with a scale factor of $1x10^{-6}$ to obtain logCPM count values and 2,000 most variable genes were

used for feature selection. Only mitochondrial genes were regressed out during scaling, cell cycle associated genes did not have an effect on the cell-to-cell clustering. "DESeq2" method was applied to do differential expression analysis between the three groups, soft, stiff and matrigel and in addition testing of genes was limited to a logFoldChange (logFC) cutoff of 1. Further, the differentially expressed genes were manually filtered for an adjusted *p-value* of 0.05. Finally, volcano plots were constructed using EnhancedVolcano 1.8.0(*49*). In addition to applying single cell method, Seurat, we also applied pure bulk RNA seq method, DESeq2(*50*), to perform the data analysis of the single cell pool samples. Results from both methods were highly similar including the list of differentially expressed genes, their respective fold changes and adjusted *p*-value. We chose to report results from Seurat due to the zero-inflated count distribution of our data which is typical of single cells than bulk RNA data (Supp.Fig.4).

Gene Set Enrichment Analysis (GSEA) of significantly Differentially Expressed Genes (DEGs) (adjusted p-value < 0.05 and |logFC|> 1) into functional categories were performed using Bioconductor packages 1.30.15. GOseq 1.42.0(*51*) and clusterProfiler 3.18.1(*52*) were used, respectively, to conduct Gene Ontology (GO)(*53*) and Kyoto Encyclopedia of Genes and Genomes (KEGG)(*54*) enrichment analyses. All the enrichment plots including GSEA, dot plot and heatmap were made using built-in functions in Seurat package or ggplot2 3.3.3(*55*). Network maps were processed based on the selected enriched GO categories using Cytoscape 3.8.2 and enrichment Map plugin(*56*).

Animal experiment

12-week-old female BALB/c nude mice (CAnN.Cg-Foxn1nu/Crl, Charles River, Sulzfeld, Germany) were acclimatized in the animal facility of the Charité-Universitätsmedizin Berlin and housed with ad libitum access to food and water. Mice injected into the left ventricle of the heart with MDA-MB-231-1833 BoM cells ($5x10^5$ cells in 100 µL ice cold PBS), using a 27G needle, under ultrasound guidance (Vevo2100, FUJIFILM VisualSonics Inc., Canada). The animals received Carprosol (CP-Pharma Handelsgesellschaft mbH, Burgdorf, Germany) and Bupresol (CP-Pharma Handelsgesellschaft mbH, Burgdorf, Germany) as analgesic drugs during and after the injection. The animals were anesthetized using isoflurane (CP-Pharma Handelsgesellschaft mbH, Burgdorf, Germany) and the eyes were protected from drying with Pan-Ophtal gel (Dr. Winzer Pharma GmbH, Berlin, Germany). The mouse was sacrificed after 2 weeks by cervical dislocation. The hind limbs were harvested and fixed with 4% paraformaldehyde (PFA) in phosphate-buffered saline (PBS) for 12 h at 4 °C and stored in PBS until further processing. All animal experiments were carried out according to the policies and procedures approved by local legal research animal welfare representatives (LAGeSo Berlin, G0224/18).

For each mouse, bones of one limb were cold embedded at 4°C in poly(methyl methacrylate) (PMMA) (Technovit 9100, Kulzer, Germany), following the manufacturer's instructions. Briefly, samples were dehydrated in an ascending ethanol series, followed by a xylene washing step, infiltration and embedding in PMMA. The staining was performed on 6 µm thick longitudinal sections using a standard protocol of Haematoxylin and Eosin staining (H & E Rapid kit, Clin-Tech, Surrey, UK). Samples were washed in tap water, followed by staining in Carazzi's double-strength Haematoxylin. After another wash in tap water, the slides were stained in Eosin, rinsed in tap water, dehydrated and mounted. The stained sections were imaged with a Keyence Digital Microscope (VKX-5550E, Keyence, Germany). For immunostaining of the slides, after deplastification and rehydration, antigen retrieval was performed (sodium citrate pH 6.0/ 0.05% Tween20) at 105°C for 15 min, followed by 10 min quenching of endogenous peroxidase activity with 3% hydrogen peroxide (Sigma-Aldrich), and a final blocking was performed with Background Sniper (Biocare Medical, Concord, CA, USA) for 10 min. Primary (FHL2 2 µg/mL and Ki67 2 µg/mL) and secondary antibodies (same as for in vitro immunofluorescence staining) were diluted in Dako antibody diluent (Dako, Germany). Washing steps were done in Dako washing buffer.

Slides were then mounted with Vectashield antifade mounting medium (Biozol, Germany) following manufacturer's instructions.

Bones of the other limb of the mouse were freeze embedded following the method of the SECTION-LAB Co. Ltd. (Hiroshima, Japan). The samples were dehydrated in an ascending sucrose solution (10%, 20% and 30% in distilled water) for 24 h each at 4°C. Following this, a metal mold was placed in cooled isopropanol and filled with embedding medium (SCEM; SECTION-LAB Co. Ltd.), placing the bone in the middle. Cryosections with a thickness of 20 µm were cut following the Kawamoto method(*57*) using a cryostat (Leica CM3060S). The section was collected using a Kawamoto film (cryofilm type II C(9)) and later attached to a microscopic slide and stored at -20°C until further use. For immunostaining the slides were blocked with blocking buffer (1%BSA/ 0.1%Tween20 in PBS). Primary and secondary antibodies were diluted in blocking buffer and incubated for at least 4 and 1h at room temperature, respectively. Washing steps (2x for 15min) were conducted in washing buffer (0.1%Tween20 in PBS) and distilled water. Slides were then mounted with Dako fluorescence mounting media (S302380-2, Agilent Technologies).

Immunofluorescence staining of human early DCCs in lymph node samples of an M0 breast cancer patient

After informed consent (ethics vote number 18-948-101), the sentinel lymph node of an M0-stage breast cancer patient (i.e. with no evidence of distant metastasis) was first divided into two halves and one half examined by histopathology. The other half was disaggregated mechanically (DAKO Medimachine, DAKO) to generate a single-cell suspension. Then, mononuclear cells were isolated using a density gradient centrifugation (60% Percoll solution, Amersham) and plated onto adhesive slides. After sedimentation of the cells, the supernatant was discarded and slides were air-dried and stored at -20°C. For immunofluorescence staining of FHL2 and Cytokeratin 8/18/19, the slides were first thawed at RT and moistened with PBS. Cells were fixed with 2% PFA (Sigma, P6148) for 10 min, washed twice with PBS and permeablized with 0.05% TritonX100 for 5 min. After two additional washing steps with PBS, cells were blocked with PBS/10% AB serum (#805135, Bio-Rad) for 1.5 hours at RT. Primary antibody incubation with monoclonal mouse anti-human Cytokeratin 8/18/19 (2 µg/mL, clone A45-B/B3, AS Diagnostik) and polyclonal rabbit anti-human FHL2 (2 µg/mL, HPA006028, Sigma/Prestige Antibodies) was performed at 4 °C overnight in PBS/10% AB serum. Following washing with PBS (4x 20 min), the slides were incubated with secondary antibodies, anti-mouse AlexaFluor 488 (5 µg/mL, A11029, Invitrogen) and anti-rabbit AlexaFluor Plus 647 (5 µg/mL, A32733, Invitrogen) and DAPI (1µg/mL, MBD0015, Sigma) in PBS/5% AB serum/2.5% goat serum for 1.5 hours. After washing off the secondary antibodies (PBS 3x 10 min) the slides were mounted with SlowFade™ Glass Soft-set Antifade Mountant (S36917, Invitrogen) and imaged on Zeiss LSM980. Images were processed with ImageJ (v.1.53q) to show the max-z-projections.

Image acquisition and analysis

Live-cell imaging was conducted in a stage top incubator (Okolab, UNO-T-H-CO_2) mounted on an inverted epifluorescence microscope (Zeiss, AxioObserver 7) and a 10x, 0.3 NA objective at 37 °C and 5% CO_2. Images were recorded every 6 h for 4-5 days. For FUCCI2 image analysis, live-cell imaging of cells on 2D TCP or 3D hydrogels was performed and mCherry and mVenus fluorescence signals were recorded every 6 h. Briefly, after choosing a focus plane at the beginning of the experiment for each field of view, a z-stack of this region/20 µm was acquired around this position, and phase contrast as well as fluorescence images were recorded.

At the end of the experiment, *in situ* viability staining with calcein was performed and the same z-stack/middle-focus plain as the final timelapse acquisition step was acquired. This allowed longitudinal correlation of viability at the end of the experiment with cell cycle progression over the course of the experiment. The number of cdt1- cells at the final timepoint was counted as the

difference between FUCCI2+ cells (cells that either express mCherry or mVenus) at the initial and the last timepoint, with additional reference to phase contrast images. Next, viable (calcein+) single cells were counted and the dynamics of their FUCCI2 fluorescence signal extracted using a semi-automated custom-made MATLAB script. To do this, viable cells were picked and tracked over and mean nuclear FUCCI2 intensity was extracted.

To quantify viability, projected images were thresholded for each channel corresponding to viable (calcein +) or dead (EthD-1) cells using a counting custom-made MATLAB script. To quantify immunofluorescence, images were first thresholded for nucleus (DAPI) and cytoskeleton (F-Actin) to localize single cells, after which the immunofluorescence signal intensity within the defined boundaries was extracted for each cell. The background signal of negatively-stained samples was used to define the threshold for positive cells. The described process was performed using an automated custom-made MATLAB script.

To quantify p21 and FHL2 localization, a Leica SP8 confocal microscope with 63x, 1.4 NA oil-immersion objective was used. Briefly, images were thresholded for nucleus (DAPI) and cytoskeleton (F-Actin) to define the respective intracellular regions, after which p21 or FHL2 average intensity within each region was recorded. The described process was performed using an automated custom-made MATLAB script.

Images of human tissue samples from patients with primary breast cancer were obtained from the Human Protein Atlas (www.proteinatlas.org)(*58*). Samples with strong FHL2 intensity were selected, of which the localization was already designated as being either nuclear or cytoplasmic.

Statistical analysis

For statistical comparison between two groups, two-tailed student's t-test or Mann-Whitney U-test were performed for normally-distributed or non-parametric groups, respectively (*: $p \leq 0.05$, **: $p \leq 0.01$, ***: $p \leq 0.001$, ****: $p \leq 0.0001$). One-way Anova with Tukey's correction or Kruskal-Wallis test with Dunn's correction were conducted for multiple-group comparison. Error bars indicate mean and standard deviation used for fraction graphs. Datasets shown as box plots with median, for 25th to 75th percentiles and whiskers for minimum and maximum used for ratio graphs. Violin plots show dashed lines for median and dotted lines for the two quartile lines, used for fluorescence intensity graphs. GraphPad Prism 8 software was used to plot the data and for statistical analysis.

References

1. C. A. Klein, Cancer progression and the invisible phase of metastatic colonization. *Nat. Rev. Cancer*. **20**, 681–694 (2020).
2. C. M. Ghajar, Metastasis prevention by targeting the dormant niche. *Nat. Rev. Cancer*. **15**, 238–247 (2015).
3. M. Montagner, E. Sahai, In vitro Models of Breast Cancer Metastatic Dormancy. *Front. Cell Dev. Biol.* **8**, 1–10 (2020).
4. S. Galarza, A. J. Crosby, C. Pak, S. R. Peyton, Control of Astrocyte Quiescence and Activation in a Synthetic Brain Hydrogel. *Adv. Healthc. Mater.* **9**, 1901419 (2020).
5. M. Quarta, J. O. Brett, R. DiMarco, A. De Morree, S. C. Boutet, R. Chacon, M. C. Gibbons, V. A. Garcia, J. Su, J. B. Shrager, S. Heilshorn, T. A. Rando, An artificial niche preserves the quiescence of muscle stem cells and enhances their therapeutic efficacy. *Nat. Biotechnol.* **34**, 752–759 (2016).

6. C. M. Madl, B. L. LeSavage, R. E. Dewi, C. B. Dinh, R. S. Stowers, M. Khariton, K. J. Lampe, D. Nguyen, O. Chaudhuri, A. Enejder, S. C. Heilshorn, Maintenance of neural progenitor cell stemness in 3D hydrogels requires matrix remodelling. *Nat. Mater.* **16**, 1233–1242 (2017).
7. A. Roch, S. Giger, M. Girotra, V. Campos, N. Vannini, O. Naveiras, S. Gobaa, M. P. Lutolf, Single-cell analyses identify bioengineered niches for enhanced maintenance of hematopoietic stem cells. *Nat. Commun.* **8**, 221 (2017).
8. C. Yang, M. W. Tibbitt, L. Basta, K. S. Anseth, Mechanical memory and dosing influence stem cell fate. *Nat. Mater.* **13**, 645–652 (2014).
9. S. Khetan, M. Guvendiren, W. R. Legant, D. M. Cohen, C. S. Chen, J. A. Burdick, Degradation-mediated cellular traction directs stem cell fate in covalently crosslinked three-dimensional hydrogels. *Nat. Mater.* **12**, 458–465 (2013).
10. S. Pradhan, J. H. Slater, Tunable hydrogels for controlling phenotypic cancer cell states to model breast cancer dormancy and reactivation. *Biomaterials*. **215**, 119177 (2019).
11. S. Nam, V. K. Gupta, H. Lee, J. Y. Lee, K. M. Wisdom, S. Varma, E. M. Flaum, C. Davis, R. B. West, O. Chaudhuri, Cell cycle progression in confining microenvironments is regulated by a growth-responsive TRPV4-PI3K/Akt-p27 Kip1 signaling axis. *Sci. Adv.* **5**, eaaw6171 (2019).
12. O. Chaudhuri, S. T. Koshy, C. Branco da Cunha, J.-W. Shin, C. S. Verbeke, K. H. Allison, D. J. Mooney, Extracellular matrix stiffness and composition jointly regulate the induction of malignant phenotypes in mammary epithelium. *Nat. Mater.* **13**, 970–978 (2014).
13. B. R. Seo, P. Bhardwaj, S. Choi, J. Gonzalez, R. C. Andresen Eguiluz, K. Wang, S. Mohanan, P. G. Morris, B. Du, X. K. Zhou, L. T. Vahdat, A. Verma, O. Elemento, C. A. Hudis, R. M. Williams, D. Gourdon, A. J. Dannenberg, C. Fischbach, Obesity-dependent changes in interstitial ECM mechanics promote breast tumorigenesis. *Sci. Transl. Med.* **7**, 301ra130-301ra130 (2015).
14. A. Lueckgen, D. S. Garske, A. Ellinghaus, D. J. Mooney, G. N. Duda, A. Cipitria, Enzymatically-degradable alginate hydrogels promote cell spreading and in vivo tissue infiltration. *Biomaterials*. **217**, 119294 (2019).
15. A. Sakaue-Sawano, H. Kurokawa, T. Morimura, A. Hanyu, H. Hama, H. Osawa, S. Kashiwagi, K. Fukami, T. Miyata, H. Miyoshi, T. Imamura, M. Ogawa, H. Masai, A. Miyawaki, Visualizing Spatiotemporal Dynamics of Multicellular Cell-Cycle Progression. *Cell*. **132**, 487–498 (2008).
16. A. Sakaue-Sawano, T. Kobayashi, K. Ohtawa, A. Miyawaki, Drug-induced cell cycle modulation leading to cell-cycle arrest, nuclear mis-segregation, or endoreplication. *BMC Cell Biol.* **12**, 2 (2011).
17. S. Gookin, M. Min, H. Phadke, M. Chung, J. Moser, I. Miller, D. Carter, S. L. Spencer, A map of protein dynamics during cell-cycle progression and cell-cycle exit. *PLOS Biol.* **15**, e2003268 (2017).
18. A. Karimian, Y. Ahmadi, B. Yousefi, Multiple functions of p21 in cell cycle, apoptosis and transcriptional regulation after DNA damage. *DNA Repair (Amst).* **42**, 63–71 (2016).
19. B. M. Baker, C. S. Chen, Deconstructing the third dimension – how 3D culture microenvironments alter cellular cues. *J. Cell Sci.* **125**, 3015–3024 (2012).
20. B. T. Martin, K. Kleiber, V. Wixler, M. Raab, B. Zimmer, M. Kaufmann, K. Strebhardt, FHL2 Regulates Cell Cycle-Dependent and Doxorubicin-Induced p21Cip1/Waf1 Expression in Breast Cancer Cells. *Cell Cycle*. **6**, 1779–1788 (2007).
21. N. Nakazawa, A. R. Sathe, G. V. Shivashankar, M. P. Sheetz, Matrix mechanics controls FHL2 movement to the nucleus to activate p21 expression. *Proc. Natl. Acad. Sci.* **113**, E6813–E6822 (2016).
22. J. Y. Lee, J. K. Chang, A. A. Dominguez, H. Lee, S. Nam, J. Chang, S. Varma, L. S. Qi, R.

B. West, O. Chaudhuri, YAP-independent mechanotransduction drives breast cancer progression. *Nat. Commun.* **10**, 1848 (2019).

23. O. Y. Dudaryeva, A. Bucciarelli, G. Bovone, F. Huwyler, S. Jaydev, N. Broguiere, M. Al-Bayati, M. Lütolf, M. W. Tibbitt, 3D Confinement Regulates Cell Life and Death. *Adv. Funct. Mater.* **i**, 2104098 (2021).
24. K. Kleiber, K. Strebhardt, B. T. Martin, The biological relevance of FHL2 in tumour cells and its role as a putative cancer target. *Anticancer Res.* **27**, 55–62 (2007).
25. J. Albrengues, M. A. Shields, D. Ng, C. G. Park, A. Ambrico, M. E. Poindexter, P. Upadhyay, D. L. Uyeminami, A. Pommier, V. Küttner, E. Bružas, L. Maiorino, C. Bautista, E. M. Carmona, P. A. Gimotty, D. T. Fearon, K. Chang, S. K. Lyons, K. E. Pinkerton, L. C. Trotman, M. S. Goldberg, J. T. H. Yeh, M. Egeblad, Neutrophil extracellular traps produced during inflammation awaken dormant cancer cells in mice. *Science (80-.).* **361**, eaao4227 (2018).
26. D. Barkan, H. Kleinman, J. L. Simmons, H. Asmussen, A. K. Kamaraju, M. J. Hoenorhoff, Z. -y. Liu, S. V. Costes, E. H. Cho, S. Lockett, C. Khanna, A. F. Chambers, J. E. Green, Inhibition of Metastatic Outgrowth from Single Dormant Tumor Cells by Targeting the Cytoskeleton. *Cancer Res.* **68**, 6241–6250 (2008).
27. J. A. Aguirre Ghiso, Inhibition of FAK signaling activated by urokinase receptor induces dormancy in human carcinoma cells in vivo. *Oncogene*. **21**, 2513–2524 (2002).
28. T. Shibue, R. A. Weinberg, Integrin 1-focal adhesion kinase signaling directs the proliferation of metastatic cancer cells disseminated in the lungs. *Proc. Natl. Acad. Sci.* **106**, 10290–10295 (2009).
29. E. E. Er, M. Valiente, K. Ganesh, Y. Zou, S. Agrawal, J. Hu, B. Griscom, M. Rosenblum, A. Boire, E. Brogi, F. G. Giancotti, M. Schachner, S. Malladi, J. Massagué, Pericyte-like spreading by disseminated cancer cells activates YAP and MRTF for metastatic colonization. *Nat. Cell Biol.* **20**, 966–978 (2018).
30. M. Werner-Klein, A. Grujovic, C. Irlbeck, M. Obradović, M. Hoffmann, H. Koerkel-Qu, X. Lu, S. Treitschke, C. Köstler, C. Botteron, K. Weidele, C. Werno, B. Polzer, S. Kirsch, M. Gužvić, J. Warfsmann, K. Honarnejad, Z. Czyz, G. Feliciello, I. Blochberger, S. Grunewald, E. Schneider, G. Haunschild, N. Patwary, S. Guetter, S. Huber, B. Rack, N. Harbeck, S. Buchholz, P. Rümmele, N. Heine, S. Rose-John, C. A. Klein, Interleukin-6 trans-signaling is a candidate mechanism to drive progression of human DCCs during clinical latency. *Nat. Commun.* **11**, 4977 (2020).
31. B. Gabriel, D.-C. Fischer, M. Orlowska-Volk, A. zur Hausen, R. Schüle, J. M. Müller, A. Hasenburg, Expression of the Transcriptional Coregulator FHL2 in Human Breast Cancer: A Clinicopathologic Study. *J. Soc. Gynecol. Investig.* **13**, 69–75 (2006).
32. A. Lueckgen, D. S. Garske, A. Ellinghaus, D. J. Mooney, G. N. Duda, A. Cipitria, Enzymatically-degradable alginate hydrogels promote cell spreading and in vivo tissue infiltration. *Biomaterials*. **217**, 119294 (2019).
33. S. T. Gould, N. J. Darling, K. S. Anseth, Small peptide functionalized thiol–ene hydrogels as culture substrates for understanding valvular interstitial cell activation and de novo tissue deposition. *Acta Biomater.* **8**, 3201–3209 (2012).
34. A. J. Minn, G. P. Gupta, P. M. Siegel, P. D. Bos, W. Shu, D. D. Giri, A. Viale, A. B. Olshen, W. L. Gerald, J. Massagué, Genes that mediate breast cancer metastasis to lung. *Nature*. **436**, 518–524 (2005).
35. Y. Kang, P. M. Siegel, W. Shu, M. Drobnjak, S. M. Kakonen, C. Cordón-Cardo, T. A. Guise, J. Massagué, A multigenic program mediating breast cancer metastasis to bone. *Cancer Cell*. **3**, 537–549 (2003).
36. V. Ponomarev, M. Doubrovin, I. Serganova, J. Vider, A. Shavrin, T. Beresten, A. Ivanova, L. Ageyeva, V. Tourkova, J. Balatoni, W. Bornmann, R. Blasberg, J. Gelovani Tjuvajev, A

novel triple-modality reporter gene for whole-body fluorescent, bioluminescent, and nuclear noninvasive imaging. *Eur. J. Nucl. Med. Mol. Imaging*. **31**, 740–751 (2004).
37. H. M. Taïeb, D. S. Garske, J. Contzen, M. Gossen, L. Bertinetti, T. Robinson, A. Cipitria, Osmotic pressure modulates single cell cycle dynamics inducing reversible growth arrest and reactivation of human metastatic cells. *Sci. Rep.* **11**, 13455 (2021).
38. BBtools software suite. *JGI DataScience* (2019).
39. J. Chu, S. Sadeghi, A. Raymond, S. D. Jackman, K. M. Nip, R. Mar, H. Mohamadi, Y. S. Butterfield, A. G. Robertson, I. Birol, BioBloom tools: fast, accurate and memory-efficient host species sequence screening using bloom filters. *Bioinformatics*. **30**, 3402–3404 (2014).
40. S. Andrews, FastQC: A Quality Control Tool for High Throughput Sequence Data. (2010).
41. P. Ewels, M. Magnusson, S. Lundin, M. Käller, MultiQC: summarize analysis results for multiple tools and samples in a single report. *Bioinformatics*. **32**, 3047–3048 (2016).
42. A. Dobin, C. A. Davis, F. Schlesinger, J. Drenkow, C. Zaleski, S. Jha, P. Batut, M. Chaisson, T. R. Gingeras, STAR: ultrafast universal RNA-seq aligner. *Bioinformatics*. **29**, 15–21 (2013).
43. Y. Liao, G. K. Smyth, W. Shi, The Subread aligner: fast, accurate and scalable read mapping by seed-and-vote. *Nucleic Acids Res.* **41**, e108–e108 (2013).
44. C. Deng, T. Daley, A. Smith, Applications of species accumulation curves in large-scale biological data analysis. *Quant. Biol.* **3**, 135–144 (2015).
45. K. Okonechnikov, A. Conesa, F. García-Alcalde, Qualimap 2: advanced multi-sample quality control for high-throughput sequencing data. *Bioinformatics*. **32**, btv566 (2015).
46. R. C. Team, R: A Language and Environment for Statistical Computing. (2020).
47. L. van der Maaten, Accelerating t-SNE using Tree-Based Algorithms. *J. Mach. Learn. Res.* **15**, 3221–3245 (2014).
48. Y. Hao, S. Hao, E. Andersen-Nissen, W. M. Mauck, S. Zheng, A. Butler, M. J. Lee, A. J. Wilk, C. Darby, M. Zager, P. Hoffman, M. Stoeckius, E. Papalexi, E. P. Mimitou, J. Jain, A. Srivastava, T. Stuart, L. M. Fleming, B. Yeung, A. J. Rogers, J. M. McElrath, C. A. Blish, R. Gottardo, P. Smibert, R. Satija, Integrated analysis of multimodal single-cell data. *Cell*. **184**, 3573-3587.e29 (2021).
49. K. Blighe, S. Rana, M. Lewis, EnhancedVolcano: Publication-ready volcano plots with enhanced colouring and labeling. (2018).
50. M. I. Love, W. Huber, S. Anders, Moderated estimation of fold change and dispersion for RNA-seq data with DESeq2. *Genome Biol.* **15**, 550 (2014).
51. M. D. Young, M. J. Wakefield, G. K. Smyth, A. Oshlack, Gene ontology analysis for RNA-seq: accounting for selection bias. *Genome Biol.* **11**, R14 (2010).
52. G. Yu, L.-G. Wang, Y. Han, Q.-Y. He, clusterProfiler: an R Package for Comparing Biological Themes Among Gene Clusters. *Omi. A J. Integr. Biol.* **16**, 284–287 (2012).
53. M. Ashburner, C. A. Ball, J. A. Blake, D. Botstein, H. Butler, J. M. Cherry, A. P. Davis, K. Dolinski, S. S. Dwight, J. T. Eppig, M. A. Harris, D. P. Hill, L. Issel-Tarver, A. Kasarskis, S. Lewis, J. C. Matese, J. E. Richardson, M. Ringwald, G. M. Rubin, G. Sherlock, Gene Ontology: tool for the unification of biology. *Nat. Genet.* **25**, 25–29 (2000).
54. M. Kanehisa, S. Goto, M. Furumichi, M. Tanabe, M. Hirakawa, KEGG for representation and analysis of molecular networks involving diseases and drugs. *Nucleic Acids Res.* **38**, D355–D360 (2010).
55. H. Wickham, *ggplot2: Elegant Graphics for Data Analysis* (Springer-Verlag New York, 2016).
56. D. Merico, R. Isserlin, O. Stueker, A. Emili, G. D. Bader, Enrichment Map: A Network-Based Method for Gene-Set Enrichment Visualization and Interpretation. *PLoS One*. **5**, e13984 (2010).
57. T. Kawamoto, Use of a new adhesive film for the preparation of multi-purpose fresh-frozen

sections from hard tissues, whole-animals, insects and plants. *Arch. Histol. Cytol.* **66**, 123–143 (2003).

58. M. Uhlen, C. Zhang, S. Lee, E. Sjöstedt, L. Fagerberg, G. Bidkhori, R. Benfeitas, M. Arif, Z. Liu, F. Edfors, K. Sanli, K. von Feilitzen, P. Oksvold, E. Lundberg, S. Hober, P. Nilsson, J. Mattsson, J. M. Schwenk, H. Brunnström, B. Glimelius, T. Sjöblom, P.-H. Edqvist, D. Djureinovic, P. Micke, C. Lindskog, A. Mardinoglu, F. Ponten, A pathology atlas of the human cancer transcriptome. *Science (80-.).* **357**, eaan2507 (2017).

59. Cortazar, A. R. *et al.* CANCERTOOL: A Visualization and Representation Interface to Exploit Cancer Datasets. *Cancer Res.* **78**, 6320–6328 (2018).

60. Chen, F., Chandrashekar, D. S., Varambally, S. & Creighton, C. J. Pan-cancer molecular subtypes revealed by mass-spectrometry-based proteomic characterization of more than 500 human cancers. *Nat. Commun.* **10**, 5679 (2019).

61. Chandrashekar, D. S. *et al.* UALCAN: An update to the integrated cancer data analysis platform. *Neoplasia* **25**, 18–27 (2022).

62. Chandrashekar, D. S. *et al.* UALCAN: A Portal for Facilitating Tumor Subgroup Gene Expression and Survival Analyses. *Neoplasia* **19**, 649–658 (2017).

63. Lánczky, A. & Győrffy, B. Web-Based Survival Analysis Tool Tailored for Medical Research (KMplot): Development and Implementation. *J. Med. Internet Res.* **23**, e27633 (2021).

64. Győrffy, B. Survival analysis across the entire transcriptome identifies biomarkers with the highest prognostic power in breast cancer. *Comput. Struct. Biotechnol. J.* **19**, 4101–4109 (2021).

Acknowledgments

This work was funded by the Deutsche Forschungsgemeinschaft (DFG) Emmy Noether grant (CI 203/2-1 to A. C., S. B, D.S. G, and S. A. E. Y.). A. C. also thanks the funding from IKERBASQUE Basque Foundation for Science and from the Spanish Ministry of Science and Innovation (PID2021-123013OB-I00). H. M. T. thanks the International Max Planck Research School (IMPRS) on Multiscale Bio Systems for financial support. J.C. and M.G thank the support provided by the Helmholtz Association through program-oriented funding and by the Federal Ministry of Education and Research, Germany, as part of the program Health Research (BCRT; Grant No. 13GW0098). This work was funded by the Bavarian ministry of economic affairs, energy and technology ("Aufbau einer Infrastruktur und Logistik zur translationalen Forschung mit Geweben von Krebspatienten", AZ 20-3410.1-1-1). The authors thank the technicians of the Research Workshop at the Charité-Universitätsmedizin Berlin for developing and manufacturing some experimental devices. We thank the lab of Dr. Joan Massagué at the Memorial Sloan Kettering Cancer Center, USA, for providing the MDA-MB-231-1883 BoM cells. We thank Aline Lueckgen, Christine Pilz, Inés Moreno-Jiménez, Geonho Song, Tina Seeman, Nicky Tam, Reynel Urrea Castellanos, Stefanie Güldener and Reinhild Dünnebacke for technical assistance with hydrogel preparation, cell culture, immunostaining, rheology, confocal microscopy, immunoblotting, blot imaging, RNA sequencing and microplate-reader measurements, respectively. The authors would like to acknowledge Peter Fratzl, Maria M. Caffarel and Andrea Abaurrea for scientific discussion.

Competing interests: CAK is member of the SAB of HiberCell.

772 **Figures**

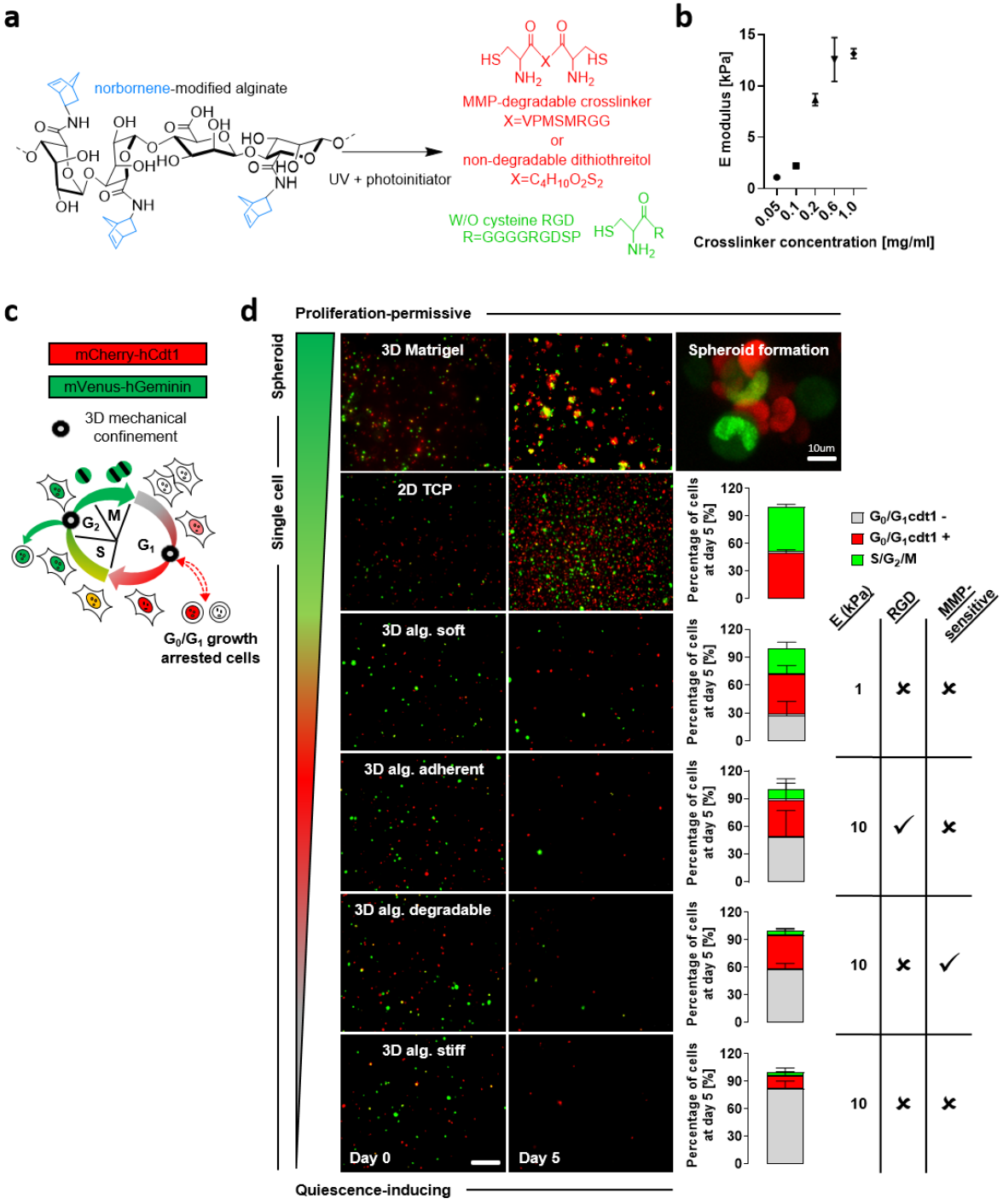

773

774 **Fig. 1 3D mechanical confinement via covalently-crosslinked alginate yields distinct**
775 **fractions and populations of growth-arrested cells based on hydrogel composition. a)**
776 Bis-cysteine enzymatically (MMP) degradable peptide or non-degradable dithiothreitol
777 (DTT) (red) crosslink with norbornene-modified alginate (blue) in the presence or absence
778 of cysteine-coupled RGD molecules (green). **b)** Frequency sweep of norbornene-modified
779 alginate (no RGD) with different concentrations of DTT crosslinker yields a range of
780 stiffness (Elastic/Young's moduli) (n=3). **c)** Diagram of FUCCI2 cell cycle reporter activity

(G_0/G_1=mCherry-hCdt1 and $S/G_2/M$=mVenus-hGeminin). The cartoon was adapted from Sakaue-Sawano et al.[15], Copyright (2008), with permission from Elsevier. **d)** Time lapse imaging (5 days) of MDA-FUCCI2 cells within a range of proliferation-permissive and quiescence-inducing hydrogels with distinct stiffness, adhesion and degradation properties (right-hand side table). Representative time lapse fluorescence maximum projections at day 0 and day 5, scale bar equals 200 μm. Scale bar equals 10 μm for 3D Matrigel spheroid image. Percentage bar plots show fraction of cell cycle distribution at day 5 for different experimental groups. Error bars indicate mean and standard deviation (n≥3 gels for 82 to 453 cells).

812

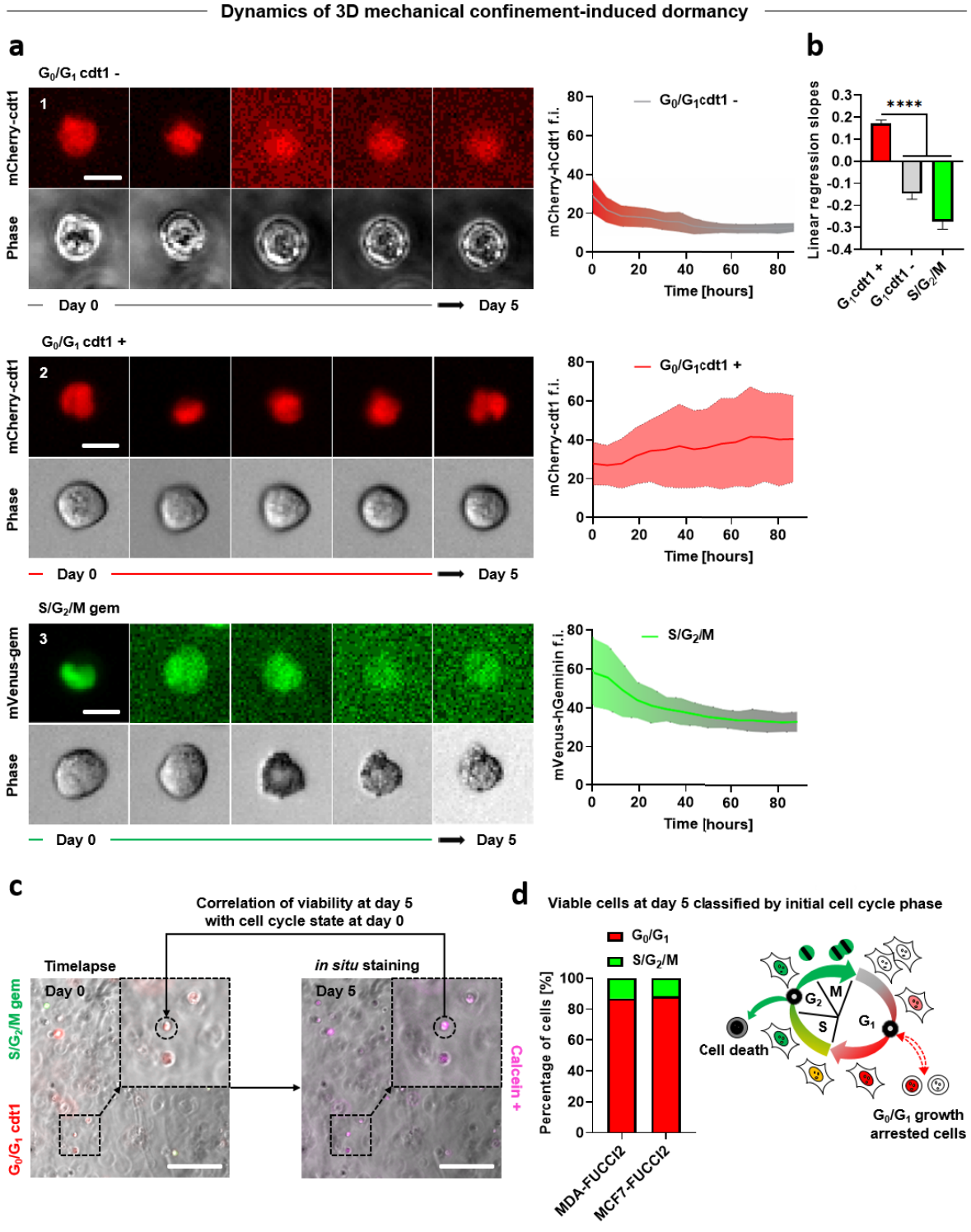

813 **Fig. 2 Dynamics of cell cycle and viability correlation reveal that G_0/G_1 cells are**
814 **substantially more resistant to 3D mechanical confinement than cells in the $S/G_2/M$**
815 **phase. a)** Representative time lapse images of single MDA-FUCCI2 cells in 3D alginate
816 stiff hydrogels with respective single cell longitudinal tracking of mCherry-hCdt1 and
817 mVenus-hGeminin fluorescence intensity (f.i.). Center trace and shaded area indicate mean
818 and standard deviation (n≥15 cells). Scale bar equals 10 µm. **b)** Comparison of linear

regression slopes from f.i. tracking graph. Kruskal–Wallis test with Dunn's correction ****p<0.0001. **c)** Experimental workflow for longitudinal correlation of FUCCI2 initial cell cycle state within 3D alginate stiff hydrogels and viability after 5 days of encapsulation. Cells were stained *in situ* for viability after 5 days time lapse and the selected cells (calcein+) were tracked back to their initial cell cycle state (time of encapsulation). Scale bar equals 200 μm. **d)** Percentage bar plots show fraction of viable cells with respect to their initial cell cycle state for MDA-FUCCI2 and MCF7-FUCCI2 cells (n≥241 cells pooled from 3 independent experiments). Diagram of cell cycle progression under 3D mechanical confinement, revealing growth arrest and higher resilience for cells in G_0/G_1 and death for cells in $S/G_2/M$. The cartoon was adapted from Sakaue-Sawano et al.[15], Copyright (2008), with permission from Elsevier.

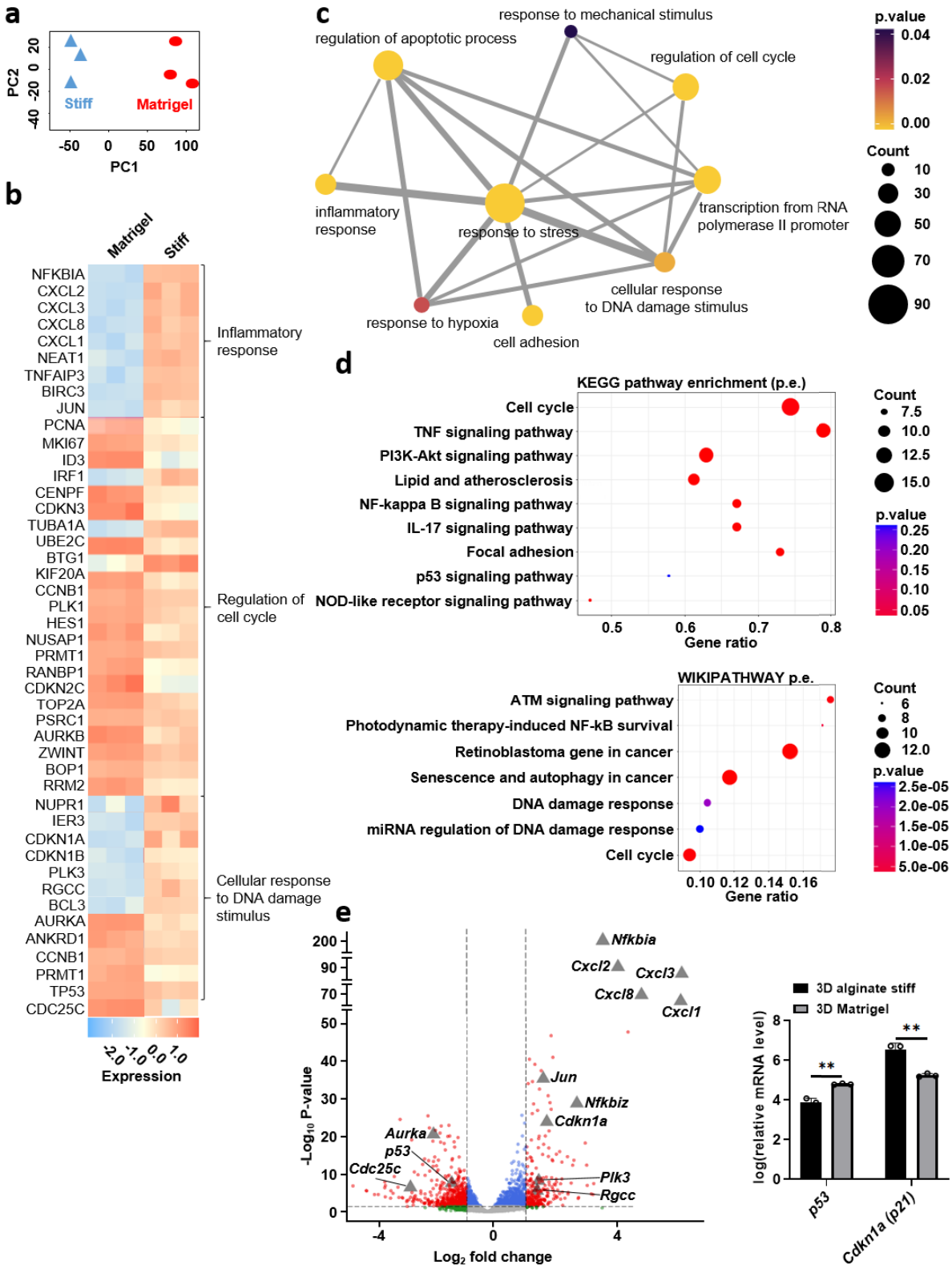

Fig. 3 Gene expression analysis of cells in 3D alginate stiff compared to 3D Matrigel. **a)** Principal-component analysis (PCA) based on all expressed genes between 3D alginate stiff and 3D Matrigel groups acquired from RNA sequencing (n=3 for each condition).

b) Heat map of selected differentially expressed genes involved in inflammatory response, regulation of cell cycle and cellular response to DNA damage stimulus. **c)** Network map of selected biological processes most enriched in 3D alginate compared to 3D Matrigel. Node size, node color and edge width represent number of genes, *p*-value from enrichment analysis and overlap of number of genes between two gene sets, respectively. **d)** Selected top differentially regulated pathways from Gene-set-enrichment analysis (GSEA) on differentially expressed genes between cells grown in 3D alginate stiff and 3D Matrigel according to KEGG and WIKIPATHWAY databases. **e)** Volcano plot of differentially expressed genes between 3D alginate stiff and 3D Matrigel. Grey triangles mark genes of interest associated with inflammation and DNA-damage pathways (grey dots=not significant, green dots= significant absolute log(base2) fold change of > 1, blue dots= significant *p-value* of < 0.05, red=significant absolute log(base2) fold change of > 1 and *p-value* <0.05 from a total of 9426 entries). Relative mRNA levels of p53 and cdkn1a (p21) (n=3 for each condition). Student's *t*-test **p≤0.01. Error bars indicate mean and standard deviation.

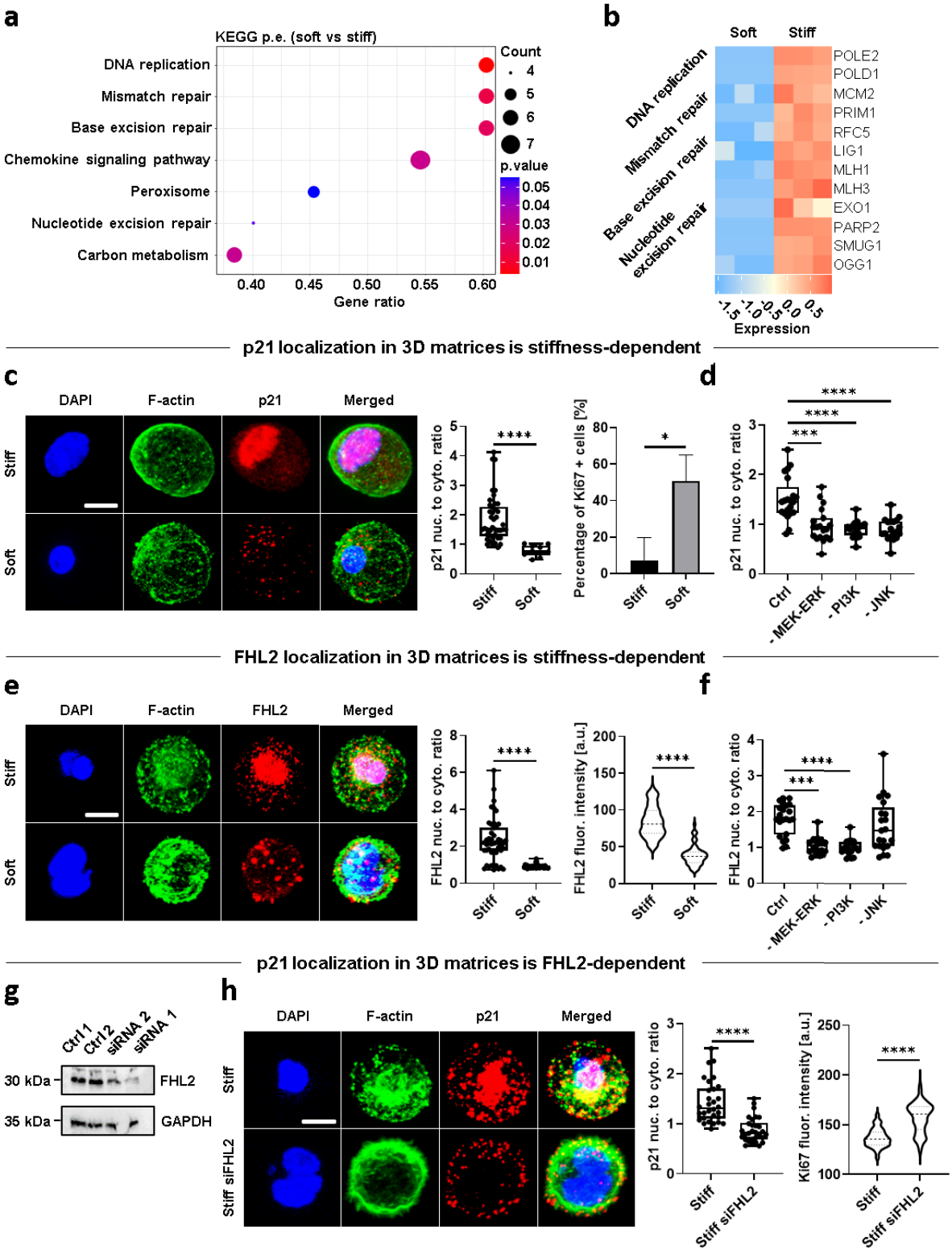

Fig. 4 p21 and FHL2 localization in 3D matrices is stiffness-dependent and FHL2 mediates p21 localization and Ki67 expression. a) Selected top differentially regulated pathways from GSEA based on differentially expressed genes between cells grown in soft vs. stiff alginate hydrogels. **b)** Heat map of differentially expressed genes (soft vs. stiff)

from DNA damage and repair pathways. **c)** Representative confocal images of p21 localization and quantification of its nuclear-to-cytoplasmic ratio (n=3 gels for 10 to 42 cells) for MDA231 cells within 3D stiff and soft alginate hydrogels after 7 days of encapsulation (blue=DAPI, green=F-Actin, red=p21). Scale bar equals 10 μm, Mann-Whitney *U*-test ****p<0.0001. Fraction of Ki67-positive cells (n=3 gels for 28 to 628 cells), student's *t*-test *p<0.05. **d)** Quantification of p21 localization in 3D alginate stiff hydrogels after 7 days in the presence or absence of indicated inhibitors (n≥19 cells). Student's *t*-test with respect to control group (3D alginate stiff) ***p<0.001 and ****p<0.0001. **e)** Representative confocal images of FHL2 localization and quantification of its nuclear-to-cytoplasmic ratio (n=3 gels for 36 to 46 cells) for MDA231 cells within 3D stiff and soft alginate hydrogels after 7 days of encapsulation (blue=DAPI, green=F-Actin, red=FHL2). Scale bar equals 10 μm, Mann-Whitney *U*-test ****p<0.0001. FHL2 fluorescence intensity (f.i.) per cell (n=3 gels for 59 to 151 cells) Mann-Whitney *U*-test ****p<0.0001. **f)** Quantification of FHL2 localization in 3D alginate stiff hydrogels after 7 days in the presence or absence of indicated inhibitors (n≥18 cells). Student's *t*-test with respect to control group (3D alginate stiff) ***p<0.001 and ****p<0.0001. **g)** Immunoblot showing FHL2 levels in MDA231 cells treated with two different anti-FHL2 siRNA oligos compared to untreated (control 1) or scramble (control 2) groups. GAPDH, glyceraldehyde-3-phosphate de-hydrogenase. **h)** Representative confocal images of p21 localization and quantification of its nuclear-to-cytoplasmic ratio (n=3 gels for 30 cells) for MDA231 normal and siRNA-FHL2 silenced cells within 3D stiff alginate hydrogels (blue=DAPI, green=F-Actin, red=p21). Scale bar equals 10 μm, Mann-Whitney *U*-test ****p<0.0001. Ki67 f.i. per cell (n= 74 to 260 cells), Mann-Whitney *U*-test ****p<0.0001. Datasets shown as box plots with median for 25th to 75th percentiles and whiskers for minimum and maximum. Violin plots show dashed lines for median and dotted lines for the two quartile lines. Error bars indicate mean and standard deviation.

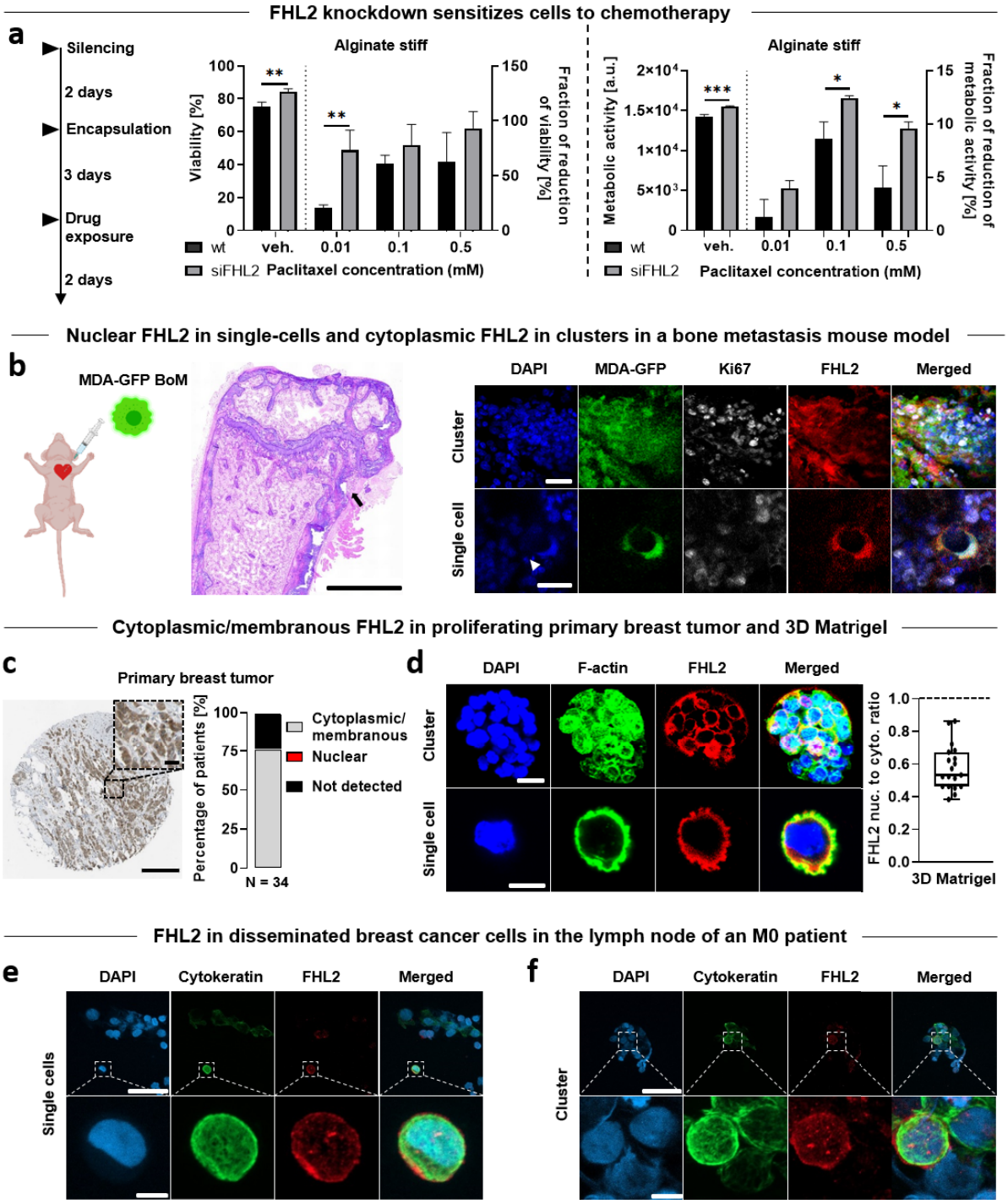

Fig. 5 FHL2 knockdown sensitizes cells to chemotherapy. FHL2 expression and localization in murine tissue of a breast cancer bone metastasis model, in human primary breast tumor and in early DCCs of an M0 patient. a) FHL2-silenced MDA231 cells were encapsulated for 3 days and exposed to Paclitaxel (0.01 to 0.5 mM) for 2 days, after which viability and metabolic activity (Presto Blue) measurements of normal and siRNA-FHL2 silenced cells within 3D alginate stiff were performed. Left y-axis corresponds to the overall viability and metabolic activity of vehicle (untreated groups). Right y-axis shows the fraction of reduction of viability and metabolic activity of drug treated groups with respect to the untreated group. Student's *t*-test (n=3 hydrogels) *p≤0.05,

p≤0.01, ***p≤0.001, ****p≤0.0001. Error bars indicate mean and standard deviation. **b) Intracardiac injection of GFP-tagged MDA-MB-231-1883 BoM cells in mice with representative Hematoxylin and Eosin (H&E) staining of the femur showing an osteolytic lesion (arrowhead). Representative confocal images of Ki67 (proliferation) and FHL2 localization of GFP-tagged MDA-MB-231-1883 BoM cells as single cells and clusters. Scale bars equal 1000 µm, 25 µm and 20 µm for H&E overview, cluster and single cell images, respectively. **c)** Representative immunohistochemical image of FHL2 localization in a female patient (50 years old) with breast ductal carcinoma. Fraction of FHL2 localization in 34 patients with primary breast ductal carcinoma. Data obtained from The Human Protein Atlas[58]. Scale bar equals 20 µm. **d)** Representative confocal images of FHL2 localization in spheroids and single MDA231 cells within 3D Matrigel after 7 days of encapsulation and quantification of its nuclear-to-cytoplasmic ratio (n=19 cells) (blue=DAPI, green=F-Actin, red=FHL2). Scale bar equals 20 µm for spheroid image and 10 µm for single cell image. **e, f)** Confocal images of cytokeratin (epithelial marker) and FHL2 (in single cells and within clusters) of human breast cancer cells disseminated in the sentinel lymph node of an M0 patient. Scale bars equal 50 µm and 5 µm for the wide and zoomed images, respectively.

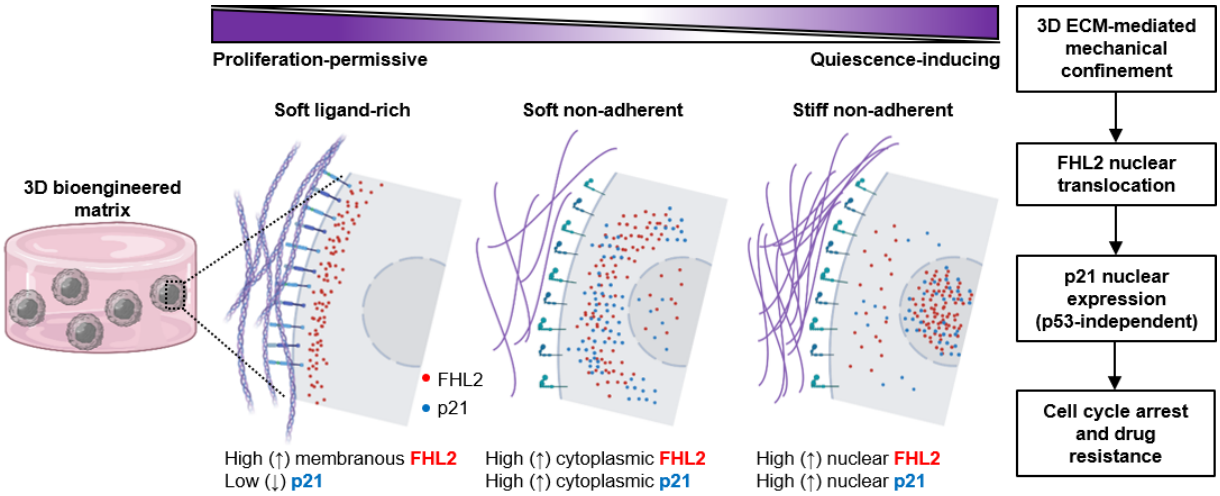

Fig. 6 Proposed stiffness-mediated FHL2 signaling mechanism in 3D bioengineered matrices inducing cancer cell quiescence and drug resistance. In proliferation-permissive, ligand-rich microenvironments such as basement membranes, stronger adhesion sites maintain FHL2 in the membranous regions. In low or non-adherent microenvironments, the increase in mechanical confinement (stiffness) results in FHL2 translocation to the nucleus, leading to high p21 nuclear expression and cell cycle arrest (graphical illustration created with BioRender.com).

SUPPLEMENTARY INFORMATION

METHODS

Synthesis of peptide-crosslinked alginate hydrogels

Norbornene-modified alginate hydrogels with thiol-ene crosslinking were synthesized as previously described[1]. Briefly, high molecular weight (265 kDa; HMW), high guluronic acid, sodium alginate (Pronova MVG; NovaMatrix) was dissolved at 1% w/v in 0.1 M 2-(N- morpholino)ethanesulfonic acid (MES; Sigma-Aldrich), 0.3M NaCl (EMD Millipore) buffer (pH 6.5) overnight at room temperature. N-hydro-xysuccinimide (NHS; Sigma-Aldrich), followed by 1-ethyl-3-(3-dimethylami-nopropyl)-carbodiimide hydrochloride (EDC; Sigma-Aldrich) were added drop-wise at 5000 molar equivalents to the alginate solution while stirring. To functionalize the alginate backbone with norbornene functional groups, 5-norbornene-2-methylamine (TCI Deutschland GmbH) was added at a theoretical degree of substitution (DStheo) of 300 molecules per alginate chain. The final concentration of both reactions was 0.6% w/v and was run while stirring at 700 rpm at room temperature for 20 h. Next, the solution was quenched by adding hydroxylamine (Sigma-Aldrich), followed by dialysis (Spectra/Por 6, MWCO 3.5 kDa; Spectrum) against a salt gradient (6 g/L to 0 g/L; Sigma-Aldrich) in ddH_2O for 3 days with 3-4 changes per day. The solution was then purified with activated charcoal (Sigma-Aldrich), sterile-filtered (0.22 µm; Steriflip-GP; Merck) and lyophilized. To assess the actual degree of substitution, NMR measurements were performed using an Agilent 600 MHz PremiumCOMPACT equipped with Agilent OneNMR Probe (256 scans), with samples dissolved at a final concentration of 1.5% w/v in deuterium oxide (D_2O) (Supp. Fig 1b, c).

Casting of peptide-crosslinked alginate hydrogels

For hydrogel casting, the VPMS↓MRGG sequence was chosen as the enzymatically-degradable peptide crosslinker (↓ denotes the MMP cleavage site), ordered from WatsonBio Sciences at 98% purity with trifluoroacetic acid removal (Supp. Fig 1d). Double-cysteine containing dithiothreitol (DTT, Sigma-Aldrich, 43816) was used as the non-degradable crosslinker. Before casting, norbornene-modified alginate and the photoinitiator (Irgacure 2959; Sigma-Aldrich) were dissolved in phosphate-buffered saline (PBS) overnight at 50 °C under shaking. Alginate and photoinitiator concentrations were kept at 2 and 0.5% w/v respectively. The concentration of the crosslinker was changed to yield hydrogels with different mechanical properties. After mixing, the solution was pipetted with positive-displacement pipettes on a glass plated and covered with a dichloromethylsilane-coated glass slide (≥99.5%; Sigma-Aldrich). To initiate thiol-ene crosslinking, the mixture was exposed to UV light (365 nm at 10 mW/cm^2, OmniCure S2000) by placing the gel sheet in a custom-built curing chamber for 10 min. Gels were then punched out using biopsy punches of 4-6 mm (Integra Miltex) and washed with PBS until further use. To render norbornene-modified alginate adherent, a thiol-containing RGD sequence (CGG- GGRGDSP; Peptide 2.0) was added to the gel precursor mix (at 0.95 mM) to bind residual norbornene groups via UV-mediated thiol-ene chemistry. For 3D cell encapsulation, a cell suspension (5x10^5 cells/ mL) was added to the precursor solution and mixed before UV exposure. Matrigel (356237, Corning) was used at 100% w/v concentration (~ 10mg/mL).

Mechanical characterization

Rheology measurements were performed to calculate the elastic modulus (E) of pre-formed gels. Norbornene-modified alginate (2% w/v) hydrogels with different stiffness were cast by changing the DTT crosslinker concentration (0.01-1 mg/mL). After gel equilibration overnight in PBS, frequency sweep measurements were performed from 0.01 to 10 Hz at 1% shear strain with an 8 mm parallel plate (PP08, Anton Paar) using a rheometer (Physica MCR 301; Anton Paar), while keeping the temperature at 25 °C with a Peltier cooling module. The initial E modulus was then calculated as follows: $E = 2G(1 + \vartheta)$ and $G = \sqrt{G'^2 + G''^2}$ where G, G' and G'' are the shear, storage and loss moduli, respectively, and ϑ the Poisson's ratio with a value of 0.5 for hydrogels[2].

Cell culture

MDA-MB-231 (HTB-26; ATCC), MDA-MB-231-1883 BoM (provided by Dr. Joan Massagué and purchased from the Antibody and Bioresource Core Facility of the Memorial Sloan Kettering Cancer Center, USA. The subclone 1833 is a bone tropic human cell line deriving from a metastasis formed by MDA-MB-231 TGL cells hosted in a mouse[3,4],which in turn are MDA-MB-231 (HTB-26; ATCC) human epithelial breast cancer cells stably transduced with a lentivirus expressing a triple-fusion reporter[5]) and MCF-7 (HTB-22; ATCC) human breast cancer cell lines were cultured in low glucose Dulbecco's Modified Eagle's Medium (D6046; Sigma-Aldrich) with 10% v/v fetal bovine serum (S0615, Sigma-Aldrich) and 1% penicillin/streptomycin (Gibco). For MCF-7 cells, 0.1% insulin (I1882, Sigma-Aldrich) was added. Cells were then incubated in a 5% CO_2 environment at 37 °C and passaged every 3-5 days.

Viability and metabolic activity characterization

Live and dead cells were stained with 1.6 mM calcein AM (C125400; TRC) and 4 mM ethidium homodimer-1 (EthD-1 L3224; ThermoFisher), respectively. To measure metabolic activity, Presto blue (ThermoFisher) was used. Briefly, after 1 and 7 days of incubation, cell culture medium was replaced with 10% Presto blue reagent in DMEM and the plate incubated for at least 4 h at 37 °C. Next, 100 µL of the supernatant was transferred to a black 96 well plate (655892, Greiner Bio-one) and fluorescence emission was measured at 590 nm (Cytation5, BioTek). ATP concentration was measured using CellTiter-Glo (Promega) according to the manufacturer's instruction. Briefly, a 1:1 volume of reagent and culture medium was added to each sample of a black 96 well plate (655892, Greiner Bio-one), shaken for 10 min at room temperature, and allowed to equilibrate for another 20 min before measuring bioluminescence signal (Cytation5, BioTek).

Lentiviral particle production, transduction and generation of FUCCI2 breast cancer cell lines

FUCCI2 vectors mCherry hCdt1(30/120)/pCSII EF MCS (DDBJ/EMBL/GenBank, AB512478) and mVenus hGeminin(1/100)/pCSII EF MCS (DDBJ/EMBL/GenBank, AB512479) were purchased from the Riken Brain Science Institute (Japan) and used to generate lentivirus particles by co-transfecting HEK 293TN cells (System Biosciences) with packaging (psPAX2, Addgene plasmid, #12260) and envelope (pMD2.G (Addgene plasmid, #12259) plasmids. The supernatant was collected by centrifuging (Beckman L7-55 with SW32Ti rotor) at 22,000 rpm for 3h at 4 °C. MDA-MB-231 and MCF-7 breast cancer cell lines were first transfected with mVenus hGeminin (1/110) (multiplicity of infection (MOI) of six and five, respectively) followed by mCherry hCdt1 (30/120) at an MOI of three. Verification of successful transduction and subsequent sorting of stably expressing mVenus and mCherry cell lines were perform using flow cytometry (FACSAriaTM II, Becton Dickinson).

Inhibition, RNA interference and drug response experiments

For inhibition experiments, the following small molecule and inhibitors were used: MEK/ERK inhibitor PD98059 (10 mM, Focus Biomolecules), JNKinhibitor SP600125 (10 mM, Focus Biomolecules) and PI3K/Akt inhibitor LY294002 (10 mM, Focus Biomolecules). The inhibitors were mixed with culture medium and refreshed every 2-3 days. To knock down FHL2, MDA-MB-231 cells were transfected with two different FHL2-targeting small interfering RNAs (Silencer siRNA, Invitrogen) or non-targeting siRNA (Stealth RNAi negative control, Invitrogen) using Lipofectamine RNAiMAX Reagent (Invitrogen), diluted in Opti-MEM reduced serum medium (Gibco) for a final concentration of 10-20 nM. Cells were transfected 2-3 days before encapsulation following manufacturer's instructions. To assess MDA-MB-231 response to chemotherapy, Paclitaxel (Tokyo Chemical Industry) was diluted at 0.01, 0.1 and 0.5 mM and added to the culture medium after 3-5 days post-encapsulation for a drug treatment of 2 days. The highest concentration tested contained around 1% (v/v) of DMSO, which was used as vehicle medium and didn't show any negative effect on cell viability.

Immunofluorescence staining

Gels with encapsulated cells were washed (3x) with PBS and fixed with 4% paraformaldehyde (PFA, Boster, #AR1068) for 30 min at room temperature, (3x) washed with 3% w/v bovine serum albumin (BSA, Sigma Aldrich), permeabilized with 0.1 % w/v Triton X 100 (Sigma-Aldrich, #T8787) for 15 min with a final washing (3x) step with 3% BSA. Whole-mount primary antibody staining was performed at 4 °C overnight, diluted in a 3% BSA+0.1% Triton X 100 buffer solution under mild shaking. The gels were then washed (3x) with 3% BSA and incubated with secondary antibody at 4 °C overnight with the same dilution buffer under mild shaking. The samples were finally imaged after a last washing step with PBS (3x). The primary antibodies and respective concentrations used in this study are the following: anti-Ki67 (2 µg/mL, ab45580, abcam), anti-p21$^{Cip1/Waf1}$ (0.48 µg/mL, 2947S, Cell Signaling), anti-FHL2 (0.5 µg/mL, HPA006028, Sigma/Prestige Antibodies). The secondary antibodies are: Alexa Fluor 405 (10 µg/mL, ab175651, abcam) and Alexa Fluor 647 (4 µg/mL, A21244, Invitrogen). To stain for nucleus and cytoskeleton, DAPI (1:1000, Roche) and Alexa Fluor 488 Phalloidin (1:50, Invitrogen) were used.

Immunoblot

Cells were first lysed with RIPA buffer (Abcam) for 5 min on ice and then collected in Eppendorf tubes. Protein concentration was calculated following Bradford assay (Bradford reagent, Sigma-Aldrich). A 1:50 mixture of β-mercaptoethanol (Acros Organics) and 2x Tricine sample buffer (Bio-Rad) was added at a 1:1 volume to the cell lysates. The mixture was then heated to 95 °C for 5 min and loaded into pre-cast polyacrylamide gels (Mini-PROTEAN TGX, Bio-Rad) for electrophoresis in TGS buffer (Bio-Rad) at 100 V for 30 min, then 200 V for 30 min (Mini-PROTEAN Tetra System, Bio-Rad). Proteins in the gels were then blotted onto to a PVDF membrane (BioTrace, PALL) at 150 V for 90

min in ice-cold transfer buffer (1:5 volume of 100% Methanol in TGS buffer). Next, the membrane was transferred to TBST buffer (150 mM NacL, 20 mM Tris-base, 0.1% Tween20), blocked in 5% BSA in TBST buffer for 1 h under gentle shaking, washed in TBST (3x) and incubated with primary antibodies diluted in 1% BSA in TBST overnight at 4 °C. After washing with TBST (3x), the membrane was incubated with an HRP-linked secondary antibody for 1 h at room temperature, after which the chemoluminescence substrate (SuperSignal West Pico PLUS, Thermo Scientific) was added before visualizing it with a blot imager (G:BOX Chemi XX6/XX9, Syngene). GAPDH (1:1000, 2118, Cell Signaling) was used as housekeeping gene and HRP-linked (1:1000, 7074, Cell Signaling) as secondary antibody.

Cell retrieval from 3D gels

For RNA sequencing, MDA-MB-231 cells were retrieved from 3D alginate stiff, soft and 3D Matrigel. Briefly, alginate hydrogels were incubated with alginate lyase (2mg/mL, Sigma Aldrich, A1603) in HBSS (ThermoFisher, 14185045) for 30 min at 37 °C with three mixture steps every 10 min. For Matrigel, pre-cooled (4°C) HBSS was added and mixed for 5-10 min at room temperature, followed by incubation with Trypsin/EDTA (0.05%/0.02%, PAN Biotech, P10-023100) for 5 min at 37 °C. Cells were then washed twice with HBSS for 5 min. Next, retrieved cells were stained using a LIVE/DEAD fixable cell staining method (ThermoFisher, L34969) following manufacturer's instructions, and viable cells were sorted via FACSAria II flow cytometer (Becton Dickinson). Approximately 1500 sorted cells per sample were then lysed using pre-cooled (4 °C) RLN buffer (0.05 M Tri-HCl pH 8.0, 0.14 M NaCl, 0.0015 M $MgCl_2$, 0.5 % v/v Nonidet P-40/IGEPAL (Sigma Aldrich, 56741) and 1000 U/mL RNase inhibitor (Promega, N2615), 0.001 M DTT) on ice for 5 min. The lysates were then centrifuged with a pre-cooled centrifuge for 2 min at 300 x g, the supernatants transferred to -80 °C and stored until further processing.

RNA sequencing and analysis

Samples were resuspended in 5 µl 1X NEBNext Cell Lysis Buffer of the NEBNext Single Cell/Low Input RNA Library Prep Kit (NEB, E6420). After 5 min incubation at RT, 2.5X RNA XP Clean Up Beads (Beckman Coulter, A63987) were added to the sample by pipetting up and down. Then, samples were incubated for 5 min at RT, the beads were pelleted on a magnet, the supernatant was removed, the samples were washed twice with 80% ethanol while remaining on the magnet, and finally the beads were resuspended in 8 µl nuclease-free water. The reverse transcription was conducted according to the manual of the NEBNext Single Cell/Low Input RNA Library Prep Kit in the presence of the beads. Next, the beads were pelleted on the magnet and the supernatant was used for the following PCR amplification as described in the manual. Twenty-one PCR cycles were applied, because the RNA concentration was below the detection limit of the Qubit RNA HS Assay Kit (Thermo Fisher, Q23852). The cleanup, quality control, fragmentation, and adapter ligation steps were performed as described in the kit manual. NEBNext Multiplex Oligos for Illumina (Index Primer Set 1) (NEB, 7335S) were used for the final PCR amplification. The fragment length distribution of the final libraries was determined using a 2100 Bioanalyzer Instrument (Agilent) with a High Sensitivity DNA kit (Agilent, 5067-4626). The libraries were quantified by qPCR with the KAPA Library Quantification Kit (Roche, KK4854). The nine samples were divided into two pools (one pool of four samples, the other of five samples) with equimolar amount. The pools were sequenced on an Illumina MiSeq with 2 x 150 bp.

After demultiplexing, raw FASTQ data were given to an in-house mRNA analysis pipeline 0.9.5.5. BBDuk 38.76[6] was used to trim the raw sequence data from soft, 3D matrigel and 3D alginate stiff, deleting any residual adapter sequences and low-quality bases at the ends of each read. BioBloom Tools 2.0.13[7] was used to decontaminate reads from the genomes Mus musculus (mm38), Escherichia coli (BL21), Mycoplasma pneumoniae (M129), Sphingobium sp. (SYK-6), Bradyrhizobium japonicum (USDA 110), Pichia pastoris (GS115), Malessia globosa (CBS 7966), Aspergillus fumigatus (Af293), and a set of viral genomes (RefSeq, 5k+ genomes). All reads that did not map exclusively to the transcriptome of hg38 (GENCODE version 27, GRCh38.p10) were labeled as potentially contaminated and were removed from further processing. FastQC 0.11.9[8] was used to evaluate sequence quality per sample before as well as after trimming and decontamination. In addition, all samples were examined as a collective with MultiQC 1.8[9]. Following that, the cleaned sample reads were aligned to the hg38 reference genome using STAR 2.5.1b[10]. Using featureCounts from Subread 2.0.0, uniquely mapping reads were counted per gene and sample[11]. Further quality criteria were evaluated, including library complexity (using Preseq 2.0.3[12]) and the genomic origin of the reads and the 5'-3'-bias (both using QualiMap 2.2.2d[13]). The final counts table of 9 samples were utilized for differential expression analysis.

All the subsequent steps after the count tables were performed in R programming language 4.0.2 (2020-06-22)[14]. Matrix table containing gene counts were visualized using Principle Component Analysis (PCA) and t-distributed stochastic neighbor embedding (t-SNE) clustering techniques. For PCA, raw counts were scaled and prcomp function from stats package was employed. tSNE plots were constructed using Rtsne 0.15[15]. Subsequent steps including Quality Control (QC) analysis, filtering, normalization, feature selection, scaling, regression of unwanted variables were performed

using Seurat package 4.0.2[16]. Default parameters were taken for all used functions unless otherwise mentioned. Normalization was done using 'log.normalize' method with a scale factor of $1x10^{-6}$ to obtain logCPM count values and 2,000 most variable genes were used for feature selection. Only mitochondrial genes were regressed out during scaling, cell cycle associated genes did not have an effect on the cell-to-cell clustering. "DESeq2" method was applied to do differential expression analysis between the three groups, soft, stiff and matrigel and in addition testing of genes was limited to a logFoldChange (logFC) cutoff of 1. Further, the differentially expressed genes were manually filtered for an adjusted *p-value* of 0.05. Finally, volcano plots were constructed using EnhancedVolcano 1.8.0[17]. In addition to applying single cell method, Seurat, we also applied pure bulk RNA seq method, DESeq2[18], to perform the data analysis of the single cell pool samples. Results from both methods were highly similar including the list of differentially expressed genes, their respective fold changes and adjusted *p*-value. We chose to report results from Seurat due to the zero-inflated count distribution of our data which is typical of single cells than bulk RNA data (Supp. Fig. 4).

Gene Set Enrichment Analysis (GSEA) of significantly Differentially Expressed Genes (DEGs) (adjusted *p*-value < 0.05 and |logFC|> 1) into functional categories were performed using Bioconductor packages 1.30.15. GOseq 1.42.0[19] and clusterProfiler 3.18.1[20] were used, respectively, to conduct Gene Ontology (GO)[21] and Kyoto Encyclopedia of Genes and Genomes (KEGG)[22] enrichment analyses. All the enrichment plots including GSEA, dot plot and heatmap were made using built-in functions in Seurat package or ggplot2 3.3.3[23]. Network maps were processed based on the selected enriched GO categories using Cytoscape 3.8.2 and enrichment Map plugin[24].

Animal experiment

12-week-old female BALB/c nude mice (CAnN.Cg-Foxn1nu/Crl, Charles River, Sulzfeld, Germany) were acclimatized in the animal facility of the Charité-Universitätsmedizin Berlin and housed with ad libitum access to food and water. Mice injected into the left ventricle of the heart with MDA-MB-231-1833 BoM cells ($5x10^5$ cells in 100 µL ice cold PBS), using a 27G needle, under ultrasound guidance (Vevo2100, FUJIFILM VisualSonics Inc., Canada). The animals received Carprosol (CP-Pharma Handelsgesellschaft mbH, Burgdorf, Germany) and Bupresol (CP-Pharma Handelsgesellschaft mbH, Burgdorf, Germany) as analgesic drugs during and after the injection. The animals were anesthetized using isoflurane (CP-Pharma Handelsgesellschaft mbH, Burgdorf, Germany) and the eyes were protected from drying with Pan-Ophtal gel (Dr. Winzer Pharma GmbH, Berlin, Germany). The mouse was sacrificed after 2 weeks by cervical dislocation. The hind limbs were harvested and fixed with 4% paraformaldehyde (PFA) in phosphate-buffered saline (PBS) for 12 h at 4 °C and stored in PBS until further processing. All animal experiments were carried out according to the policies and procedures approved by local legal research animal welfare representatives (LAGeSo Berlin, G0224/18).

For each mouse, bones of one limb were cold embedded at 4°C in poly(methyl methacrylate) (PMMA) (Technovit 9100, Kulzer, Germany), following the manufacturer's instructions. Briefly, samples were dehydrated in an ascending ethanol series, followed by a xylene washing step, infiltration and embedding in PMMA. The staining was performed on 6 µm thick longitudinal sections using a standard protocol of Haematoxylin and Eosin staining (H & E Rapid kit, Clin-Tech, Surrey, UK). Samples were washed in tap water, followed by staining in Carazzi's double-strength Haematoxylin. After another wash in tap water, the slides were stained in Eosin, rinsed in tap water, dehydrated and mounted. The stained sections were imaged with a Keyence Digital Microscope (VKX-5550E, Keyence, Germany). For immunostaining of the slides, after deplastification and rehydration, antigen retrieval was performed (sodium citrate pH 6.0/ 0.05% Tween20) at 105°C for 15 min, followed by 10 min quenching of endogenous peroxidase activity with 3% hydrogen peroxide (Sigma-Aldrich), and a final blocking was performed with Background Sniper (Biocare Medical, Concord, CA, USA) for 10 min. Primary (FHL2 2 µg/mL and Ki67 2 µg/mL) and secondary antibodies (same as for in vitro immunofluorescence staining) were diluted in Dako antibody diluent (Dako, Germany). Washing steps were done in Dako washing buffer. Slides were then mounted with Vectashield antifade mounting medium (Biozol, Germany) following manufacturer's instructions.

Bones of the other limb of the mouse were freeze embedded following the method of the SECTION-LAB Co. Ltd. (Hiroshima, Japan). The samples were dehydrated in an ascending sucrose solution (10%, 20% and 30% in distilled water) for 24 h each at 4°C. Following this, a metal mold was placed in cooled isopropanol and filled with embedding medium (SCEM; SECTION-LAB Co. Ltd.), placing the bone in the middle. Cryosections with a thickness of 20 µm were cut following the Kawamoto method[25] using a cryostat (Leica CM3060S). The section was collected using a Kawamoto film (cryofilm type II C(9)) and later attached to a microscopic slide and stored at -20°C until further use. For immunostaining the slides were blocked with blocking buffer (1%BSA/ 0.1%Tween20 in PBS). Primary and secondary antibodies were diluted in blocking buffer and incubated for at least 4 and 1h at room temperature, respectively. Washing steps (2x for 15min) were conducted in washing buffer (0.1%Tween20 in PBS) and distilled water. Slides were then mounted with Dako fluorescence mounting media (S302380-2, Agilent Technologies).

Image acquisition and analysis

Live-cell imaging was conducted in a stage top incubator (Okolab, UNO-T-H-CO_2) mounted on an inverted epifluorescence microscope (Zeiss, AxioObserver 7) and a 10x, 0.3 NA objective at 37 °C and 5% CO_2. Images were recorded every 6 h for 4-5 days. For FUCCI2 image analysis, live-cell imaging of cells on 2D TCP or 3D hydrogels was performed and mCherry and mVenus fluorescence signals were recorded every 6 h. Briefly, after choosing a focus plane at the beginning of the experiment for each field of view, a z-stack of this region/20 µm was acquired around this position, and phase contrast as well as fluorescence images were recorded.

At the end of the experiment, *in situ* viability staining with calcein was performed and the same z-stack/middle-focus plain as the final timelapse acquisition step was acquired. This allowed longitudinal correlation of viability at the end of the experiment with cell cycle progression over the course of the experiment. The number of cdt1- cells at the final timepoint was counted as the difference between FUCCI2+ cells at the initial and the last timepoint, with additional refer to phase contrast images. Next, viable (calcein+) single cells were counted and the dynamics of their FUCCI2 fluorescence signal extracted using a semi-automated custom-made MATLAB script. To do this, viable cells were picked and tracked over and mean nuclear FUCCI2 intensity was extracted.

To quantify viability, projected images were thresholded for each channel corresponding to viable (calcein +) or dead (EthD-1) cells using a counting custom-made MATLAB script. To quantify immunofluorescence, images were first thresholded for nucleus (DAPI) and cytoskeleton (F-Actin) to localize single cells, after which the immunofluorescence signal intensity within the defined boundaries was extracted for each cell. The background signal of negatively-stained samples was used to define the threshold for positive cells. The described process was performed using an automated custom-made MATLAB script.

To quantify p21 and FHL2 localization, a Leica SP8 confocal microscope with 63x, 1.4 NA oil-immersion objective was used. Briefly, images were thresholded for nucleus (DAPI) and cytoskeleton (F-Actin) to define the respective intracellular regions, after which p21 or FHL2 average intensity within each region was recorded. The described process was performed using an automated custom-made MATLAB script.

Images of human tissue samples from patients with primary breast cancer were obtained from the Human Protein Atlas (www.proteinatlas.org)[26]. Samples with strong FHL2 intensity were selected, of which the localization was already designated as being either nuclear or cytoplasmic.

Statistical analysis

For statistical comparison between two groups, two-tailed student's t-test or Mann-Whitney U-test were performed for normally-distributed or non-parametric groups, respectively (*: $p \leq 0.05$, **: $p \leq 0.01$, ***: $p \leq 0.001$, ****: $p \leq 0.0001$). One-way Anova with Tukey's correction or Kruskal-Wallis test with Dunn's correction were conducted for multiple-group comparison. Error bars indicate mean and standard deviation used for fraction graphs. Datasets shown as box plots with median, for 25^{th} to 75^{th} percentiles and whiskers for minimum and maximum used for ratio graphs. Violin plots show dashed lines for median and dotted lines for the two quartile lines, used for fluorescence intensity graphs. GraphPad Prism 8 software was used to plot the data and for statistical analysis.

SUPPLEMENTARY FIGURES

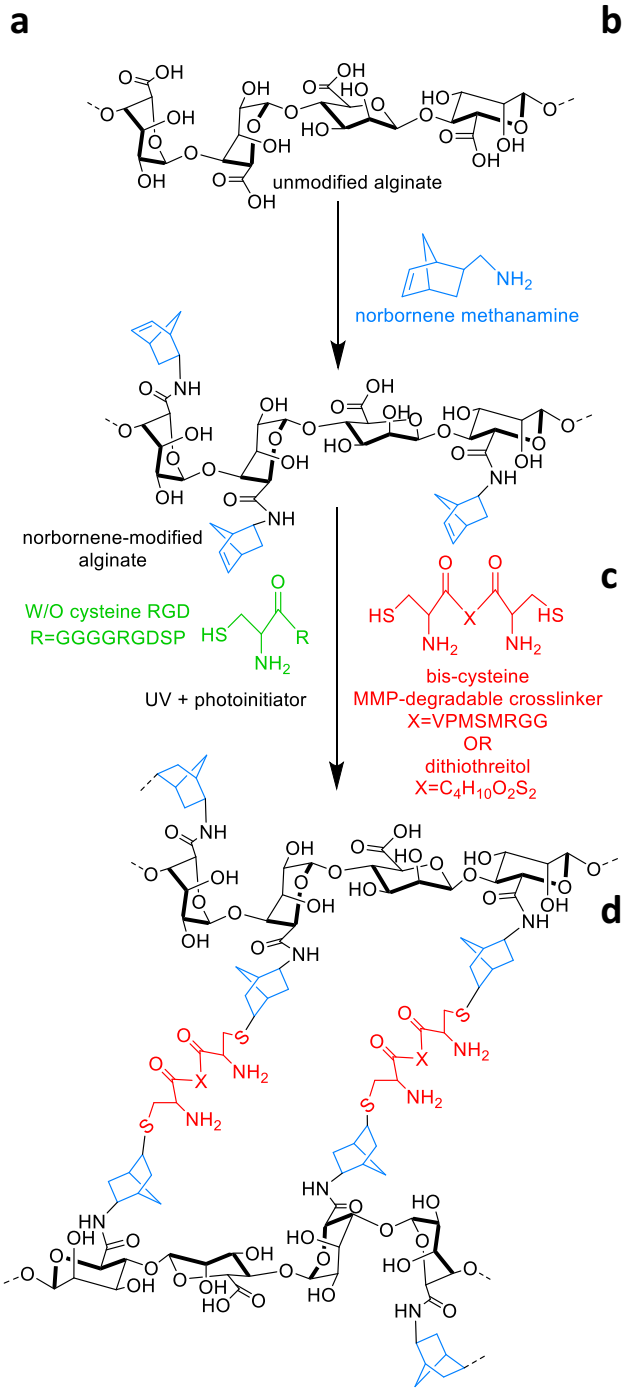

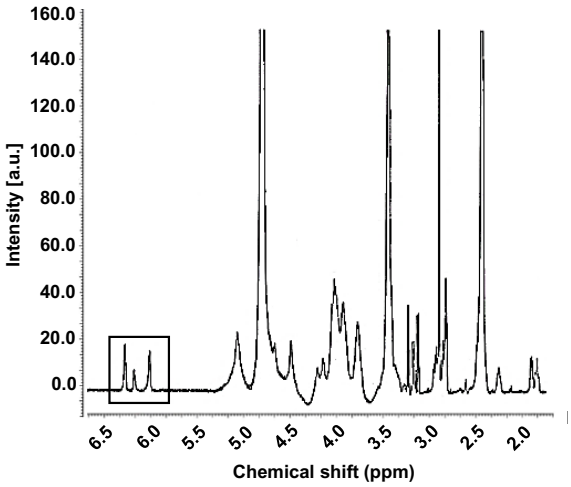

c

Molecular weight (kDa)	265
Norbornene DS (theo)	300
Norbornene DS (actual)	169.74
Reaction efficiency (%)	56.58

d

Sequence	GCRD**VPMSMRGG**DRCG
Structure	$C_{63}H_{109}N_{25}O_{22}S_4$
Residues (#)	16
Linker	GCRD-XXX-DRCG
Molecular Weight	1697
Water solubility	Good
Isoelectric point	8.11
Charge	+1

Supplementary Fig. 1 Norbornene-modified alginate chemical characterization. a) Norbornene modification of alginate chains upon exposure to UV light and a photoinitiator in the

presence of an MMP-degradable or non-degradable crosslinker via thiol-ene reaction. Cysteine-containing RGD is incorporated during the crosslinking reaction. **b)** NMR spectrum of norbornene-modified alginate, indicating the corresponding norbornene peaks (a.u.=arbitrary unit). **c)** Theoretical and actual degree of substitution (DS) with reaction efficiency (%) of norbornene-modified alginate. **d)** MMP-sensitive peptide crosslinker properties, including water solubility, isoelectric point and charge calculated using PepCalc.com (http://pepcalc.com; Innovagen AB).

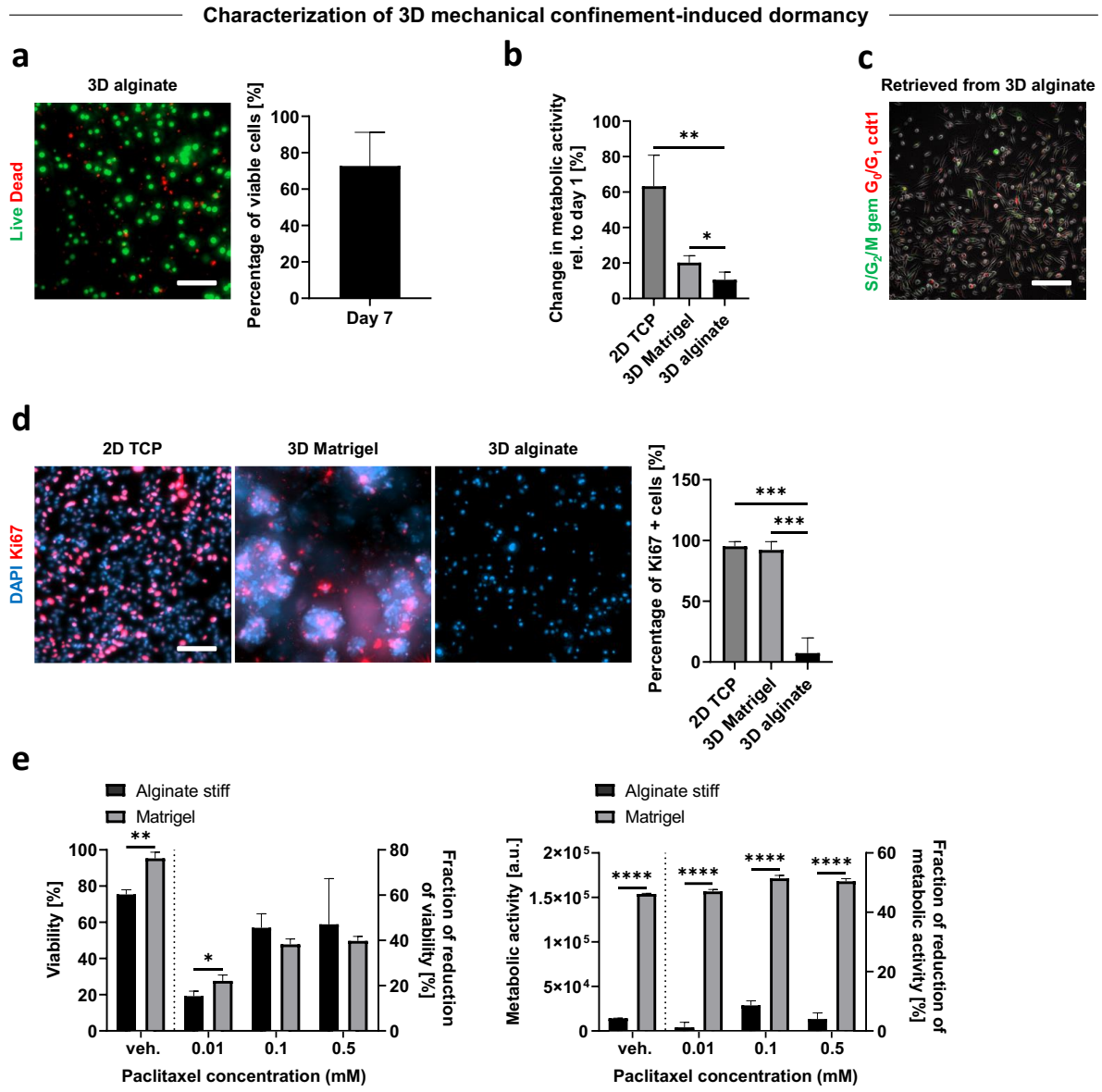

Supplementary Fig. 2 3D mechanical confinement induces quiescence while retaining high viability. a) Representative live/dead (live=calcein, dead=ethidium homodimer) fluorescence orthogonal projection and quantification of MDA231 cells encapsulated in 3D alginate stiff after 7 days of encapsulation (n=3 gels with 134 to 204 cells). Scale bar equals 200 µm **b)** Change in metabolic activity of MDA231 cells growing on 2D TCP, 3D Matrigel and 3D alginate stiff at day 7 relative to day 1 quantified using Presto Blue assay. **c)** MDA-FUCCI2 cells retrieved from 3D alginate stiff after 5 days of encapsulation (G_0/G_1=mCherry-cdt1 and $S/G_2/M$=mVenus-geminin). Scale bar equals 100 µm **d)** Representative Ki67 immunofluorescence images of MDA231 cells growing on 2D TCP, in 3D Matrigel and in 3D alginate stiff (blue=DAPI, red=Ki67). Fraction of Ki67-positive cells (n=3 gels for 148 to 1147 cells), student's *t*-test with respect to 3D alginate stiff ***p≤0.001. Scale bar equals 100 µm. Error bars indicate mean and standard deviation. **e)** MDA231 cells were encapsulated for 3 days and exposed to Paclitaxel (0.01 to 0.5 mM) for 2 days, after which viability (Calcein) and metabolic activity (Presto Blue) measurements within 3D

Matrigel and 3D alginate stiff were performed. Left y-axis corresponds to the overall metabolic activity of vehicle (untreated groups). Right y-axis shows the fraction of reduction of viability and metabolic activity of drug treated groups with respect to the untreated group. Student's *t*-test (n=3 hydrogels) *p≤0.05, **p≤0.01, ***p≤0.001, ****p≤0.0001. Error bars indicate mean and standard deviation.

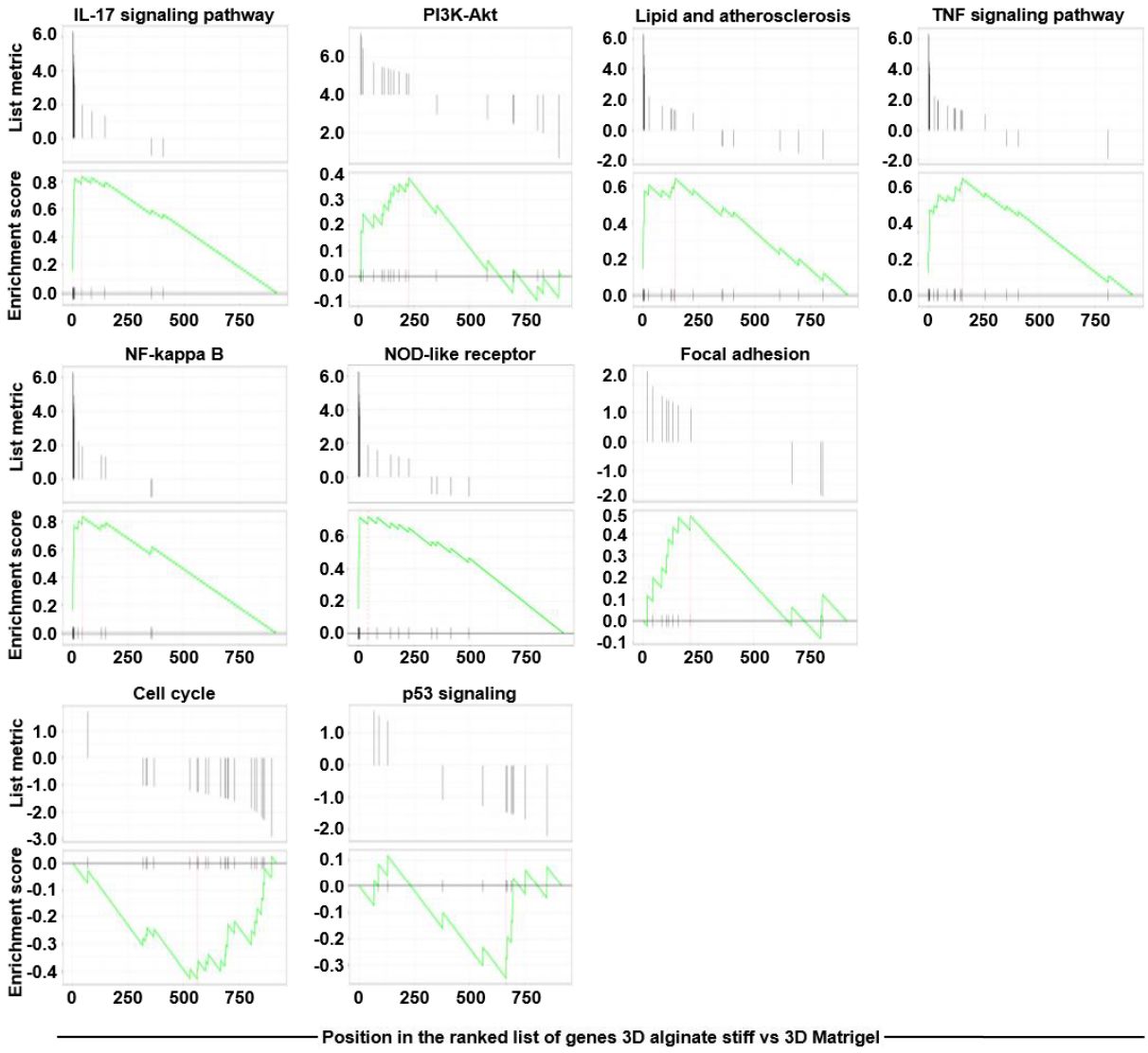

Supplementary Fig. 3 Representative genes-set-enrichment analysis (GSEA) of the differentially regulated pathways between cells grown in 3D alginate stiff and 3D Matrigel (relative to Fig. 3d).

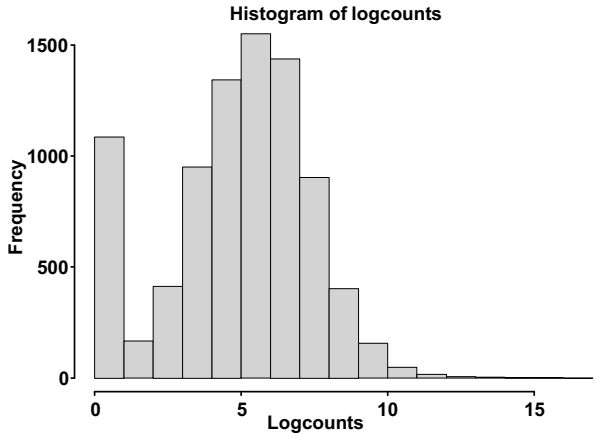

Supplementary Fig. 4 Histogram of RNA-seq logcounts.

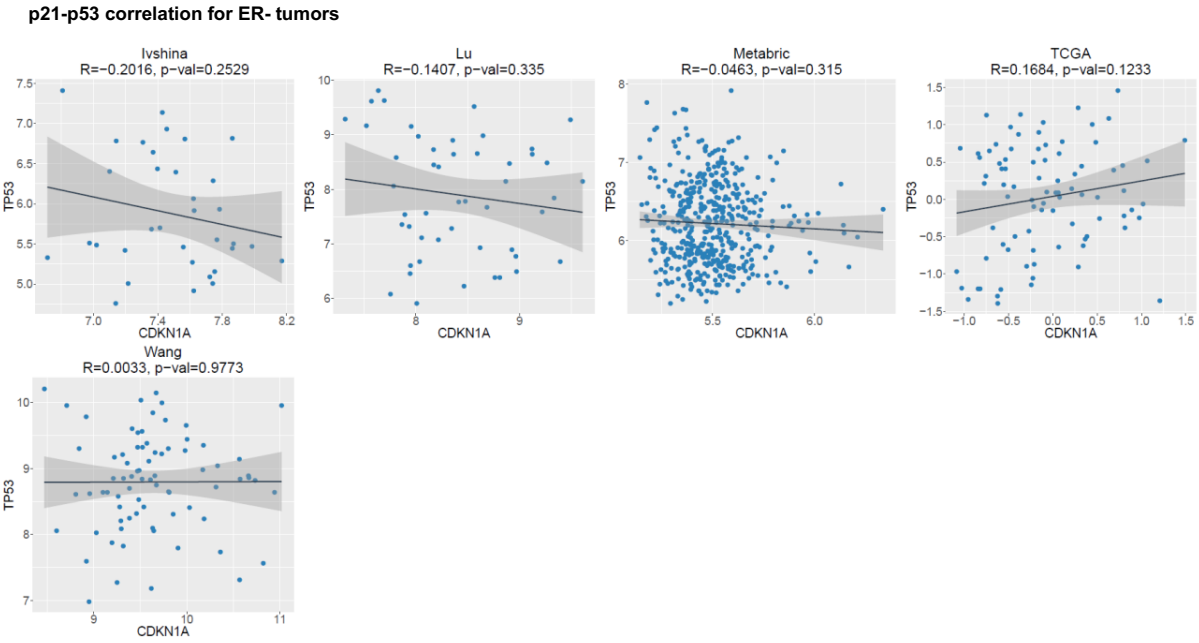

Supplementary Fig. 5 p21 and p53 show no correlation in patients with primary estrogen receptor negative (ER-) breast cancer. Plotted values correspond to the log2-normalized gene expression values (fluorescence intensity or RSEM-UQ) for two genes (in X and Y-axis) for each patient in the indicated dataset. Black line represents linear regression, grey area indicates the limits of the confidence intervals and R and p indicate Pearson´s correlation coefficient (depending on the analysis selected) and statistical significance, respectively. Data obtained from CANCERTOOL[27].

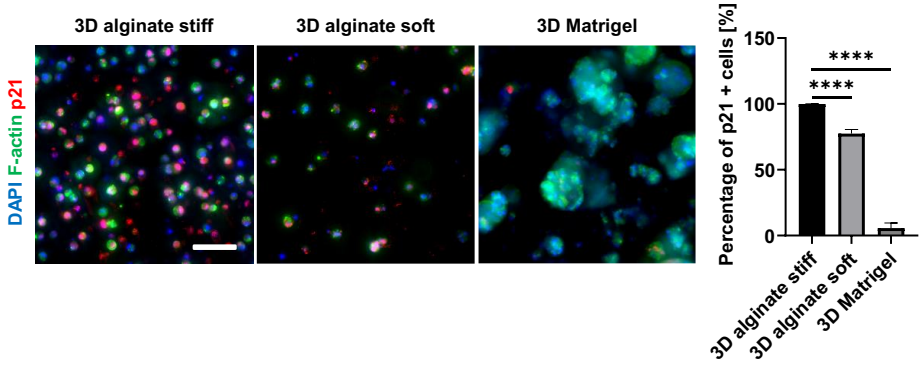

Supplementary Fig. 6 Representative p21 immunofluorescence images of MDA-FUCCI2 cells in 3D alginate stiff, soft and Matrigel (blue=DAPI, green=F-Actin, red=p21). Fraction of p21-positive cells (n=4 gels for 93 to 385 cells), student's *t*-test with respect to 3D alginate stiff ****p≤0.0001. Scale bar equals 100 µm. Error bars indicate mean and standard deviation.

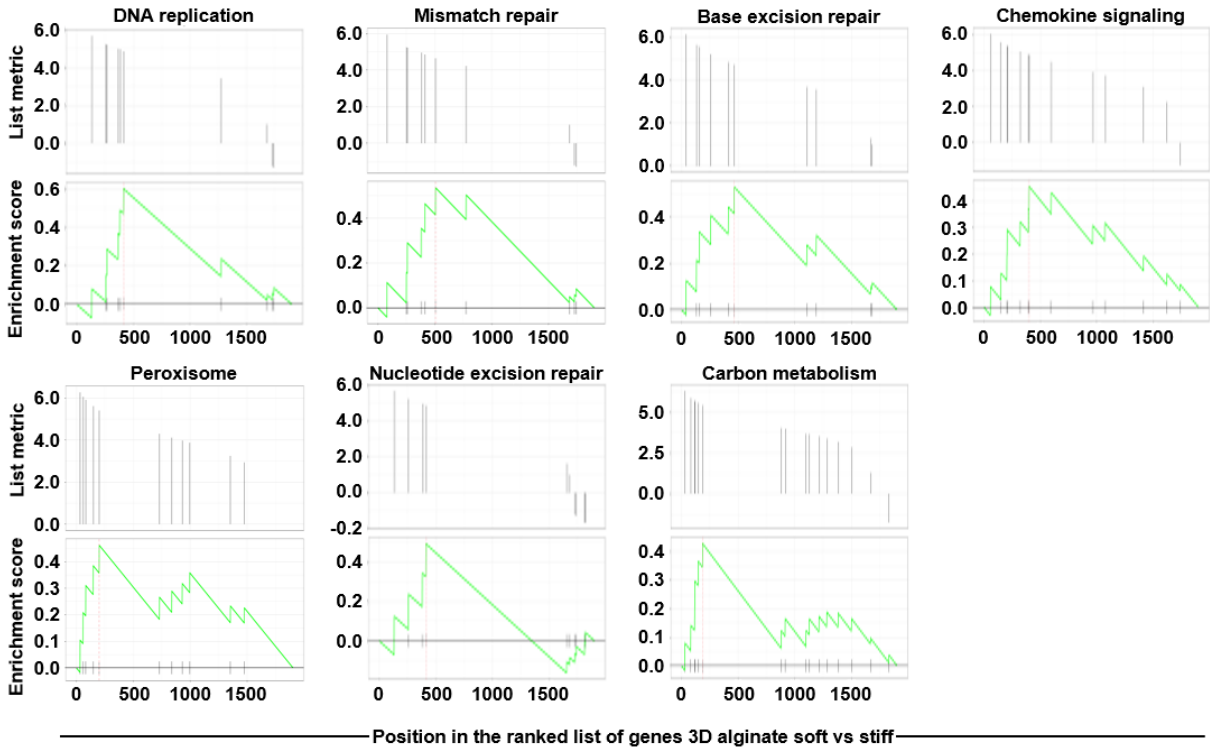

Supplementary Fig. 7 Representative genes-set-enrichment analysis (GSEA) of the differentially regulated pathways between cells grown in 3D alginate stiff and soft (relative to Fig. 4a).

Supplementary Fig. 8 FHL2 and p21 show correlation in patients with estrogen receptor negative (ER-) breast cancer. Plotted values correspond to the log2-normalized gene expression values (fluorescence intensity or RSEM-UQ) for two genes (in X and Y-axis) for each patient in the indicated dataset. Black line represents linear regression, grey area indicates the limits of the confidence intervals and R and p indicate Pearson´s correlation coefficient (depending on the analysis selected) and statistical significance, respectively. Data obtained from CANCERTOOL[27].

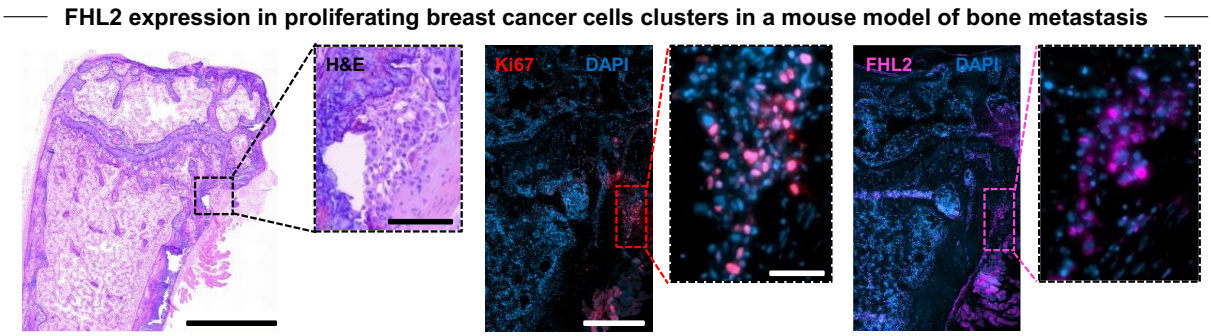

Supplementary Fig. 9 FHL2 expression in proliferating breast cancer cell clusters in a preclinical mouse model of metastatic breast cancer and in human primary tumor biopsies. Hematoxylin and Eosin (H&E) staining of mouse femur showing an osteolytic lesion with disseminated tumor cells in the cortical region with corresponding Ki67 and FHL2 immunofluorescence staining of the selected region. Scale bar equals 1000 µm for H&E overview image, 100 µm for H&E zoomed image, 400 µm for Ki67 and FHL2 overview images and 50 µm for Ki67 and FHL2 zoomed images.

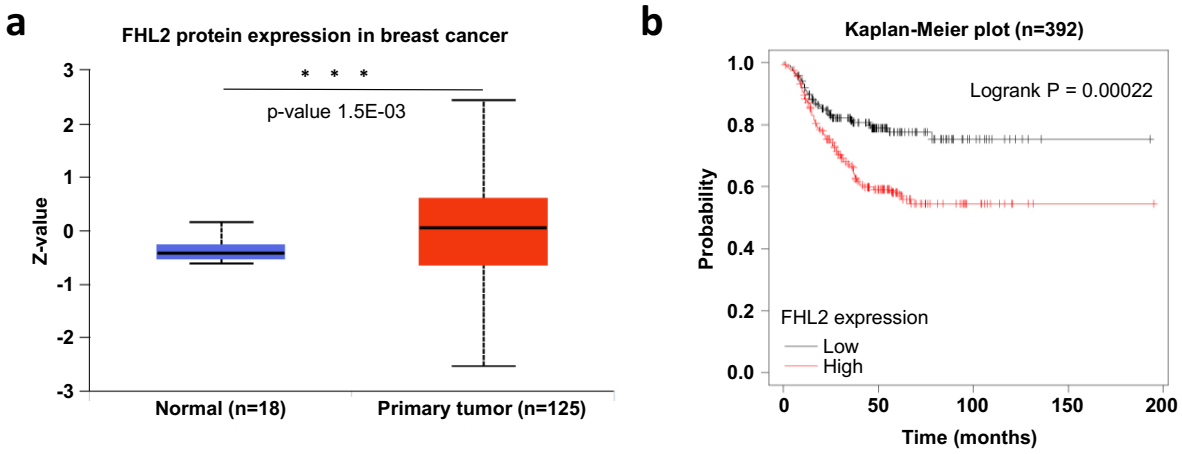

Supplementary Fig. 10 Higher FHL2 protein expression in primary breast tumor tissue and lower relapse-free survival of patients with triple-negative breast cancer and high FHL2. a) Protein expression of FHL2 in patients with breast cancer (n=number of patients). Z-values represent standard deviations from the median across samples. Log2 Spectral count ratio values from Clinical Proteomic Tumor Analysis Consortium (CPTAC)[28] were first normalized within each sample profile, then normalized across samples. Data obtained from UALCAN database[29]. **b)** Kaplan-Meier relapse-free survival plots according to FHL2 expression levels for patients with triple-negative breast cancer (n=number of patients). Data obtained from KMplot.com[30].

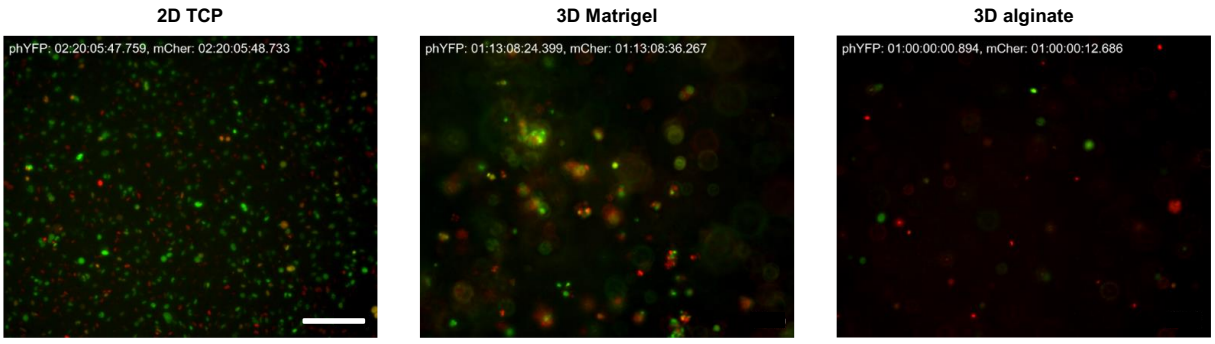

Supplementary Mov. 1-3 (separate files). Representative time lapse videos of MDA-FUCCI2 cells on 2D TCP, in 3D Matrigel and 3D alginate stiff. Scale bar equals 200 µm (G_0/G_1=mCherry-cdt1 and $S/G_2/M$=mVenus-geminin).

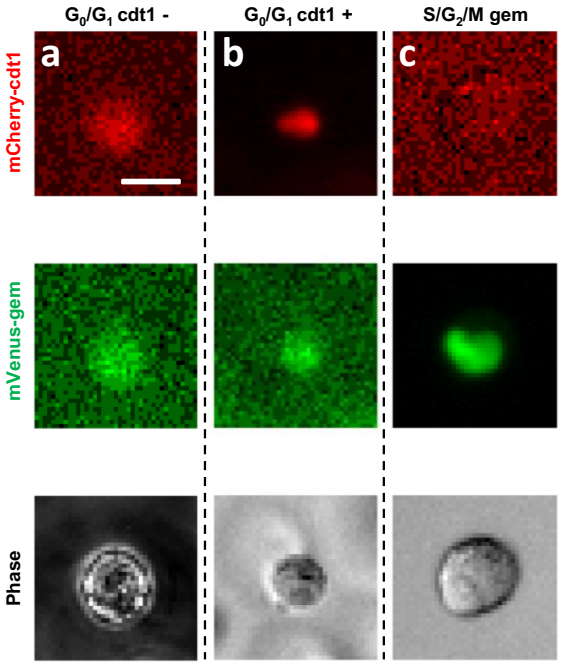

Supplementary Mov. 4-6 (separate files). Representative time lapse videos of three separate single MDA-FUCCI2 cells representative of a) G_0/G_1 cdt1-, b) G_0/G_1 cdt1+ and c) $S/G_2/M$ in 3D alginate stiff hydrogels (G_0/G_1=mCherry-cdt1, $S/G_2/M$=mVenus-geminin and phase contrast from top to bottom). Scale bar equals 10 µm.

REFERENCES

1. Lueckgen, A. *et al.* Enzymatically-degradable alginate hydrogels promote cell spreading and in vivo tissue infiltration. *Biomaterials* **217**, 119294 (2019).
2. Gould, S. T., Darling, N. J. & Anseth, K. S. Small peptide functionalized thiol–ene hydrogels as culture substrates for understanding valvular interstitial cell activation and de novo tissue deposition. *Acta Biomater.* **8**, 3201–3209 (2012).
3. Minn, A. J. *et al.* Genes that mediate breast cancer metastasis to lung. *Nature* **436**, 518–524 (2005).
4. Kang, Y. *et al.* A multigenic program mediating breast cancer metastasis to bone. *Cancer Cell* **3**, 537–549 (2003).
5. Ponomarev, V. *et al.* A novel triple-modality reporter gene for whole-body fluorescent, bioluminescent, and nuclear noninvasive imaging. *Eur. J. Nucl. Med. Mol. Imaging* **31**, 740–751 (2004).
6. BBtools software suite. *JGI DataScience* (2019).
7. Chu, J. *et al.* BioBloom tools: fast, accurate and memory-efficient host species sequence screening using bloom filters. *Bioinformatics* **30**, 3402–3404 (2014).
8. Andrews, S. FastQC: A Quality Control Tool for High Throughput Sequence Data. (2010).
9. Ewels, P., Magnusson, M., Lundin, S. & Käller, M. MultiQC: summarize analysis results for multiple tools and samples in a single report. *Bioinformatics* **32**, 3047–3048 (2016).
10. Dobin, A. *et al.* STAR: ultrafast universal RNA-seq aligner. *Bioinformatics* **29**, 15–21 (2013).
11. Liao, Y., Smyth, G. K. & Shi, W. The Subread aligner: fast, accurate and scalable read mapping by seed-and-vote. *Nucleic Acids Res.* **41**, e108–e108 (2013).
12. Deng, C., Daley, T. & Smith, A. Applications of species accumulation curves in large-scale biological data analysis. *Quant. Biol.* **3**, 135–144 (2015).
13. Okonechnikov, K., Conesa, A. & García-Alcalde, F. Qualimap 2: advanced multi-sample quality control for high-throughput sequencing data. *Bioinformatics* **32**, btv566 (2015).
14. Team, R. C. R: A Language and Environment for Statistical Computing. (2020).
15. van der Maaten, L. Accelerating t-SNE using Tree-Based Algorithms. *J. Mach. Learn. Res.* **15**, 3221–3245 (2014).
16. Hao, Y. *et al.* Integrated analysis of multimodal single-cell data. *Cell* **184**, 3573-3587.e29 (2021).
17. Blighe, K., Rana, S. & Lewis, M. EnhancedVolcano: Publication-ready volcano plots with enhanced colouring and labeling. (2018).
18. Love, M. I., Huber, W. & Anders, S. Moderated estimation of fold change and dispersion for RNA-seq data with DESeq2. *Genome Biol.* **15**, 550 (2014).
19. Young, M. D., Wakefield, M. J., Smyth, G. K. & Oshlack, A. Gene ontology analysis for RNA-seq: accounting for selection bias. *Genome Biol.* **11**, R14 (2010).
20. Yu, G., Wang, L.-G., Han, Y. & He, Q.-Y. clusterProfiler: an R Package for Comparing Biological Themes Among Gene Clusters. *Omi. A J. Integr. Biol.* **16**, 284–287 (2012).
21. Ashburner, M. *et al.* Gene Ontology: tool for the unification of biology. *Nat. Genet.* **25**, 25–29 (2000).
22. Kanehisa, M., Goto, S., Furumichi, M., Tanabe, M. & Hirakawa, M. KEGG for representation and analysis of molecular networks involving diseases and drugs. *Nucleic Acids Res.* **38**, D355–D360 (2010).
23. Wickham, H. *ggplot2: Elegant Graphics for Data Analysis*. (Springer-Verlag New York, 2016).
24. Merico, D., Isserlin, R., Stueker, O., Emili, A. & Bader, G. D. Enrichment Map: A Network-Based Method for Gene-Set Enrichment Visualization and Interpretation. *PLoS One* **5**, e13984 (2010).

25. Kawamoto, T. Use of a new adhesive film for the preparation of multi-purpose fresh-frozen sections from hard tissues, whole-animals, insects and plants. *Arch. Histol. Cytol.* **66**, 123–143 (2003).

26. Uhlen, M. *et al.* A pathology atlas of the human cancer transcriptome. *Science (80-.).* **357**, eaan2507 (2017).

27. Cortazar, A. R. *et al.* CANCERTOOL: A Visualization and Representation Interface to Exploit Cancer Datasets. *Cancer Res.* **78**, 6320–6328 (2018).

28. Chen, F., Chandrashekar, D. S., Varambally, S. & Creighton, C. J. Pan-cancer molecular subtypes revealed by mass-spectrometry-based proteomic characterization of more than 500 human cancers. *Nat. Commun.* **10**, 5679 (2019).

29. Chandrashekar, D. S. *et al.* UALCAN: A Portal for Facilitating Tumor Subgroup Gene Expression and Survival Analyses. *Neoplasia* **19**, 649–658 (2017).

30. Győrffy, B. Survival analysis across the entire transcriptome identifies biomarkers with the highest prognostic power in breast cancer. *Comput. Struct. Biotechnol. J.* **19**, 4101–4109 (2021).

4

Publication II: Optical quantification of intracellular mass density and cell mechanics in 3D mechanical confinement

4.1 Transition

After establishing our quiescence-inducing platform, we came across a work in which a pH-driven transition of the cytoplasm from fluid- to a solid-like state was shown to promote entry to a dormant state in yeast cells. To investigate whether a similar process occurs in dormant breast cancer cells as well, we teamed with the Guck's lab in Dresden to measure intracellular mass density and mechanics using state-of-the art label- and contact-free microscopy techniques.

4.2 Personal contribution

For this publication, I carried out the material synthesis, hydrogel fabrication and characterization, as well as in vitro experiments with the support of all co-authors. Additionally, I evaluated the data, interpreted the results, generated the figures, and wrote the manuscript. Optical diffraction tomography and Brillouin image acquisition were performed by collaborators from Dresden.

4.3 Publication notification

This work was published in the journal *Soft Matter* in September 2020 and is available at https://doi.org/10.1039/D0SM01556C, reproduced with permission from the Royal Society of

"Quiescence-inducing 3D-engineered matrix uncovers drug protective signaling pathway of dormant cancer cells"

Sadra Bakhshandeh, Hubert M. Taïeb, Raimund Schlüßler, Kyoohyun Kim, Timon Beck, Anna Taubenberger, Jochen Guck, Amaia Cipitria

Soft Matter

PAPER

View Article Online
View Journal | View Issue

Cite this: *Soft Matter*, 2021, **17**, 853

Optical quantification of intracellular mass density and cell mechanics in 3D mechanical confinement†

Sadra Bakhshandeh,[a] Hubert M. Taïeb,[a] Raimund Schlüßler,[b] Kyoohyun Kim,[bc] Timon Beck,[bc] Anna Taubenberger,[b] Jochen Guck*[bc] and Amaia Cipitria *[a]

Biophysical properties of cells such as intracellular mass density and cell mechanics are known to be involved in a wide range of homeostatic functions and pathological alterations. An optical readout that can be used to quantify such properties is the refractive index (RI) distribution. It has been recently reported that the nucleus, initially presumed to be the organelle with the highest dry mass density (ρ) within the cell, has in fact a lower RI and ρ than its surrounding cytoplasm. These studies have either been conducted in suspended cells, or cells adhered on 2D substrates, neither of which reflects the situation *in vivo* where cells are surrounded by the extracellular matrix (ECM). To better approximate the 3D situation, we encapsulated cells in 3D covalently-crosslinked alginate hydrogels with varying stiffness, and imaged the 3D RI distribution of cells, using a combined optical diffraction tomography (ODT)-epifluorescence microscope. Unexpectedly, the nuclei of cells in 3D displayed a higher ρ than the cytoplasm, in contrast to 2D cultures. Using a Brillouin-epifluorescence microscope we subsequently showed that in addition to higher ρ, the nuclei also had a higher longitudinal modulus (M) and viscosity (η) compared to the cytoplasm. Furthermore, increasing the stiffness of the hydrogel resulted in higher M for both the nuclei and cytoplasm of cells in stiff 3D alginate compared to cells in compliant 3D alginate. The ability to quantify intracellular biophysical properties with non-invasive techniques will improve our understanding of biological processes such as dormancy, apoptosis, cell growth or stem cell differentiation.

Received 28th August 2020,
Accepted 16th November 2020

DOI: 10.1039/d0sm01556c

rsc.li/soft-matter-journal

Introduction

The biophysical properties of cells hold important physiological information.[1,2] This can be gathered from different levels of structural hierarchy, spanning from cellular-level mechanics and cytoskeletal organization to sub-cellular level spatial distribution and the physicochemical state of organelles and sub-organelles. It has been shown that biophysical properties such as cell stiffness, can be altered during physiological processes such as stem cell differentiation[3,4] and tissue morphogenesis[5,6] as well as pathological conditions like cardiovascular diseases,[7,8] tumour growth, migration and metastasis.[9–12] At the sub-cellular level, liquid–liquid phase separation of cytoplasmic stress granules or nuclear chromatin condensation, are examples of physical changes that have also been linked to cellular states and processes such as dormancy,[13] apoptosis[14] and cell growth.[15] These biological phenomena have also been associated with changes in mass density (ρ) distribution within the cell. The refractive index (RI), reported to vary at the sub-cellular level, is linearly proportional to protein concentration in most in most biological materials,[16,17] which can be in turn correlated with good approximation to ρ and has been proposed as a suitable parameter in cell sorting and diagnostic devices.[18]

Earlier optical studies on two-dimensional (2D) cell cultures reported higher RI for the nucleus compared to the cytoplasm.[19–22] Interestingly, recent studies using a variety of microscopy techniques such as quantitative phase imaging,[23,24] orientation-independent differential interference microscopy,[25] plasmon resonance microscopy[26] and transport-of-intensity microscopy,[27] have shown the opposite. Furthermore, using a combined optical diffraction tomography (ODT) and epifluorescence microscope, it was reported that such relationship, meaning the cytoplasm having a higher RI and ρ than the

[a] *Department of Biomaterials, Max Planck Institute of Colloids and Interfaces, Potsdam, Germany. E-mail: amaia.cipitria@mpikg.mpg.de*
[b] *Biotechnology Center, Center for Molecular and Cellular Bioengineering, Technische Universität Dresden, Dresden, Germany*
[c] *Max Planck Institute for the Science of Light & Max-Planck-Zentrum für Physik und Medizin, Erlangen, Germany. E-mail: jochen.guck@mpl.mpg.de*

† Electronic supplementary information (ESI) available. See DOI: 10.1039/d0sm01556c

nucleus, is robustly conserved not only throughout the whole cell cycle, but also after actin and microtubule depolymerization and chromatin condensation or decondensation.[28] Upon drug perturbations, the cell morphology, including shape, volume and dry mass changed, while the relative mass densities among sub-cellular compartments was preserved.[28]

Most of these studies have been performed on 2D substrates or suspended cells, neglecting the third dimension (3D) provided by the extracellular matrix (ECM) in physiological environments. Changes in the ECM have been associated to phenotypic and genotypic alterations in cell properties such as morphology,[29] differentiation,[30] signal transduction,[31] migration and proliferation.[32] To our knowledge, no study has investigated the effect of the dimensionality provided by the ECM on sub-cellular mass distribution. For this purpose, we employed a covalently-crosslinked 3D alginate hydrogel, which allows for versatile and independent tuning of various biophysical properties such as adhesion,[33] stiffness,[33,34] viscoelasticity[35–37] and degradation.[38,39] Using a custom-made combined ODT-epifluorescence microscope, we quantitatively mapped the 3D RI distribution of human breast cancer cells MDA-MB-231, encapsulated in 3D hydrogels with different stiffness, and compared the resulting ρ with cells on 2D substrates.

While optical properties of cells are accessible in 2D and 3D using optical techniques, mechanical testing of cells has mostly been performed using mechanical or particle probes such as atomic force microscopy (AFM) indentation,[40] micropipette aspiration[41] or optical tweezers.[42] However, with the more recent availability of optical techniques such as Brillouin spectroscopy,[43,44] it is now possible to measure mechanical properties of cells in a contact-free fashion. Its ability to map at high resolution 3D (visco)elastic properties[45,46] in terms of longitudinal modulus M and viscosity η, has made Brillouin spectroscopy an attractive tool in the biomechanical analysis of biological samples, in this case cells encapsulated in 3D hydrogels.

This is, to our knowledge, the first study where the effect of dimensionality and matrix stiffness on intracellular ρ distribution and sub-cellular mechanics have been assessed in a 3D, contact-free fashion using ODT-epifluorescence and confocal Brillouin-epifluorescence microscopes. We show that the nuclei of MDA-MB-231 cells in 3D hydrogels display higher RI and ρ compared to the cytoplasm, differently to what is commonly found on 2D substrates. In addition, the nuclei reveal higher M and η compared to the cytoplasm. Moreover, cells encapsulated in stiff alginate hydrogels show a higher M for both the nucleus and cytoplasm compared to cells in compliant 3D alginate hydrogels.

Materials and methods

Fabrication of covalently-crosslinked norbornene-modified alginate hydrogels

Covalently-crosslinked alginate hydrogels were fabricated as previously reported.[38] Briefly, 1% w/v high guluronic acid sodium alginate (265 kDa Pronova MVG; NovaMatrix) was dissolved in 0.1 M 2-(*N*-morpholino)ethanesulfonic acid (MES; Sigma-Aldrich), 0.3 M NaCl (EMD Millipore) buffer (pH 6.5) overnight. *N*-Hydroxysuccinimide (NHS; Sigma-Aldrich) and 1-ethyl-3-(3-dimethylaminopropyl)-carbodiimide hydrochloride (EDC; Sigma-Aldrich) were added drop-wise at 5000 molar equivalents to the alginate solution while stirring. To functionalize the polymer backbone with norbornene, 5-norbornene-2-methylamine (TCI Deutschland GmbH) was added to the solution. The theoretical degree of substitution (DS_{theo}) was aimed at 300 molecules per alginate chain. The reaction (final concentration 0.6% w/v) was run for 20 h stirring at 700 rpm and quenched with hydroxylamine (Sigma-Aldrich). After 3 days dialysis (Spectra/Por 6, MWCO 3.5 kDa; Spectrum) with 3–4 changes per day against a salt gradient (6 g L^{-1} to 0 g L^{-1}; Sigma-Aldrich), purification followed using activated charcoal (Sigma-Aldrich). Finally, the solution was sterile-filtered (0.22 μm; Steriflip-GP; Merck) and lyophilized.

Thiol–ene crosslinking and casting of norbornene-modified alginate hydrogels

Norbornene-modified alginate and the photoinitiator (PI, Irgacure 2959; Sigma-Aldrich) were dissolved in PBS overnight at 50 °C under shaking. The crosslinker dithiothreitol (DTT, Sigma-Aldrich) was mixed just before casting for a final concentration of 2% w/v alginate and 0.5% w/v PI. The solution was then pipetted on glass plates using positive displacement pipettes, covered with a dichloromethylsilane-coated glass slide (≥99.5%; Sigma-Aldrich) with 2 mm spacers, placed in a custom-built chamber and exposed to UV light (365 nm) for 10 min at 10 mW cm^{-2} (OmniCure S2000). The coated glass slide was then carefully removed and the gels were punched out using biopsy punches (Integra Miltex) with 8 mm in diameter. The reaction of double cysteine-containing DTT with the alkene-containing molecules of norbornene in the presence of a photoinitiator, yielded covalently-crosslinked non degradable 3D hydrogels after UV exposure (Fig. 1a). The fast and high efficiency of this click reaction results in an increased yield of functionalization without side products. A final washing step with PBS to remove residual and unreacted material preceded the mechanical characterization.

Mechanical characterization of hydrogels

Norbornene-modified alginate (2% w/v) with different concentration of DTT (0.01–0.1 mg mL^{-1}) was casted to yield hydrogels with different stiffness. Following overnight incubation in PBS, a frequency sweep from 0.01 to 10 Hz over 30 min was performed at constant 1% shear strain using a rheometer (Physica MCR 301; Anton Paar) with a 8 mm flat plate (PP08; Anton Paar). The temperature was kept at 25 °C using a Peltier cooling module. The elastic modulus (E) was calculated using the following equations:[47] $E = 2G(1 + \vartheta)$ and $G = \sqrt{G'^2 + G''^2}$. G, G' and G'' are the shear, storage and loss moduli respectively. E is the Young's modulus and $\vartheta = 0.5$ is the Poisson's ratio in hydrogels.[48]

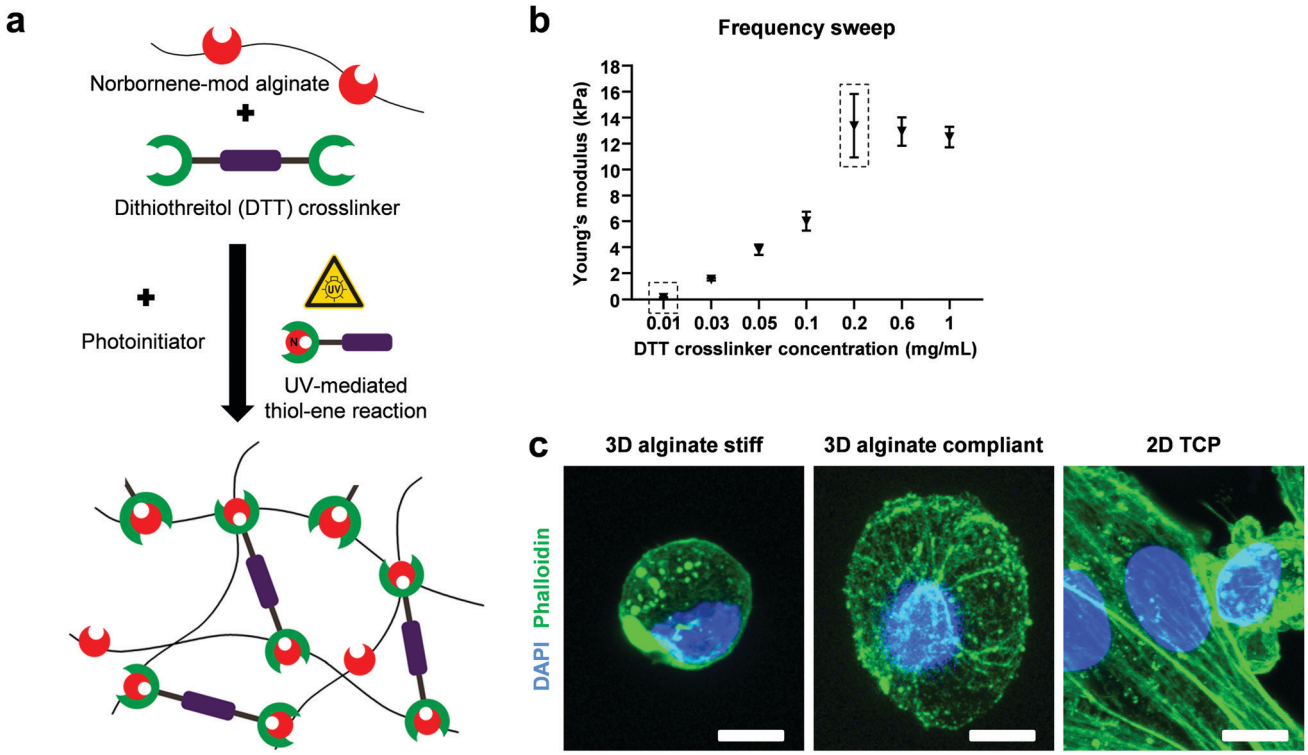

Fig. 1 Thiol–ene mediated norbornene-modified 3D alginate hydrogels allows for synthesis of hydrogels with tunable mechanical properties. (a) Norbornene-modified alginate hydrogels were synthesized *via* a UV-mediated thiol–ene crosslinking process. The alkene groups in the norbornene form covalent bonds with the thiol groups in the double-cysteine-containing dithiothreitol (DTT) crosslinker. (b) Frequency sweep was conducted with a rheometer from 0.01 to 10 Hz at 1% shear strain at 25 °C. Different concentrations of DTT yield Young's moduli between 300 Pa to 13 kPa (n = 3). Dashed boxes indicate the concentrations and corresponding Young's moduli used as the compliant and stiff 3D alginate groups. (c) Representative maximum projection images of DAPI (blue = nucleus) and phalloidin (green = actin fibers) stainings of MDA-MB-231 cells encapsulated in stiff alginate hydrogels (13 kPa), compliant alginate hydrogels (300 Pa) and on 2D TCP. Scale bar equals 10 μm.

Cell culture and generation of FUCCI2 cell reporters

MDA-MB-231 highly metastatic human breast cancer cells (HTB-26; ATCC) were cultured in Dulbecco's Modified Eagle's Medium (D6046; Sigma-Aldrich) supplemented with 10% v/v fetal bovine serum (Biochrom), and 1% penicillin/streptomycin (Gibco). The cells were incubated in a 5% CO_2 environment at 37 °C and passaged every 3–5 days. MDA-MB-231 FUCCI2 cell cycle reporter was generated using lentiviral transduction and employed as nucleus reporter as previously reported.[49] Briefly, lentiviral particles were produced by co-transfecting HEK-293TN cells (System Biosciences) with mCherry-hCdt1 (30/120)/pCSII-EF-MCS (DDBJ/EMBL/GenBank, AB512478) or mVenus-hGeminin (1/100)/pCSII-EF-MCS (DDBJ/EMBL/GenBank, AB512479) lentiviral vectors in the presence of packaging and envelope plasmids psPAX2 (Addgene plasmid, #12260) and pMD2.G (Addgene plasmid, #12259). Subsequently, parental MDA-MB-231 cell line was transfected with the previously produced particles and sorted *via* FACSAria™ II flow cytometer (Becton Dickinson) for mCherry and mVenus fluorescence. For 2D experiments, cells were seeded on 2D glass bottom dishes (FluoroDish, WPI).

3D cell encapsulation, viability and morphological characterization

Norbornene-modified alginate with two different DTT concentrations (0.01 and 0.2 mg mL^{-1}) were selected to yield compliant (300 Pa) and stiff (13 kPa) hydrogels, respectively. For 3D cell encapsulation, MDA-MB-231 cells were mixed with the gel precursor solution as a cell suspension (10^6 cells per mL). To visualize the nucleus and actin cytoskeleton, 3D encapsulated cells were fixed with paraformaldehyde 4% (Boster), permeabilized with 0.1% wt/v Triton-X-100 (Sigma-Aldrich), blocked with 3% wt/v bovine serum albumin (Sigma-Aldrich) in phosphate buffer solution (PBS) and stained with DAPI (1 : 1000, Roche) and Alexa Fluor 488 Phalloidin (1 : 50, Invitrogen). Due to camera limitations resulting in the FUCCI2 signal not being detectable for cells in 3D hydrogels, Hoechst 33342 (8 μM, Molecular Probes) was used for live nuclear staining following manufacturer's indications. To assess viability, cells were stained with 1.6 μM calcein AM (C125400; TRC) and 4 μM ethidium homodimer-1 (L3224; Thermo Fisher Scientific) for live and dead, respectively. Images were acquired using either a Zeiss AxioObserver 7 fluorescence microscope and a 10×, 0.3 NA objective or a Leica SP8 confocal microscope with 63×, 1.4 NA oil-immersion objective.

Optical diffraction tomography: setup, tomogram reconstruction and analysis

The combined ODT and epifluorescence microscope setup hasde-scribed.[50] Briefly, to measure the 3D RI distribution, a Mach–Zehnder interferometer was used (Fig. 2). A laser beam

(λ = 532 nm, frequency-doubled Nd-YAG laser, Torus, Laser Quantum Inc.) and an optical fiber were coupled and then separated into two beams using a 2 × 2 single-mode fiber-optic coupler. These beams were used as sources for sample illumination and reference through a tube lens (f = 175 mm) on a custom-made inverted microscope equipped with a water immersion objective lens (NA = 1.0, 40×, Carl Zeiss AG).

The samples were illuminated from 150 different incident angles using a dual-axis galvano-mirror (GVS012/M, Thorlabs Inc.) in order to reconstruct the 3D RI tomograms of cells.

A high-numerical aperture objective lens (NA = 1.2, 63×, water immersion, Carl Zeiss AG) and a tube lens (f = 200 mm) were employed for collection of the diffracted beam. The total magnification was set at 57×.

Interference between the reference and the diffracted beam at an image plane resulted in a spatially modulated hologram which was recorded using a CCD camera (FL3-U3-13Y3M-C, FLIR Systems, Inc.). Temperature of the glass bottom Petri dish and the objective lenses were kept at 37 °C with resistant foil heaters (Thorlabs Inc.).

For epifluorescence measurements, a three-channel dichroic mirror (FF409/493/596-Di01-25×36, Semrock Inc.) was employed to couple an incoherent light from a halogen lamp (DC-950, Dolan-Jenner Industries Inc.) into the same path as the ODT beam. To image the nuclei with Hoechst staining, a corresponding bandpass filter was employed.

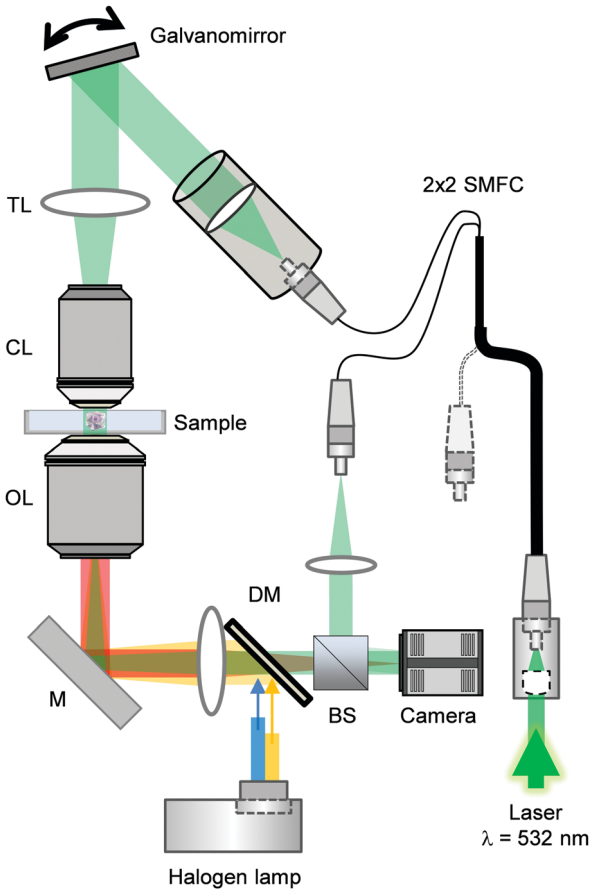

Fig. 2 Combined optical diffraction tomography and epifluorescence microscope setup. Abbreviations correspond to BS = beam splitter, DM = dichroic mirror, M = mirror, OL = objective lens, CL = condenser lens, TL = tube lens, SMFC = single-mode fiber coupler. Image adapted from ref. 28.

The Fourier transform-based field retrieval algorithm was applied to obtain the complex optical fields of the scattered light from the recorded holograms, which were then used to reconstruct the 3D RI distribution using the Fourier diffraction theorem.[51–53] More detailed descriptions can be found elsewhere.[54,55]

Based on the reconstructed tomograms, the nucleus was then segmented using the Hoechst or FUCCI2 fluorescence image, while the boundaries for the cytoplasm were defined by the plasma membrane and double-checked with phase contrast images (Fig. 3).

In addition, the perinuclear region was segmented separately as the neighbouring region within 2 μm distance from the nuclear membrane by expanding the nuclear binary mask.

The mass density ρ, is linearly proportional to the RI in most biological samples[16,17] and was calculated using the following equation:[28] $\rho = (n - n_m)/\alpha$, where n is the sample RI, n_m the RI of the empty hydrogel which was measured using an Abbe refractometer (2WAJ, Arcarda GmbH) and found to be 1.3370 at λ = 532 nm, and α = 0.190 mL g^{-1} as the RI increment for proteins and nucleic acids.[56,57] To calculate the cell volume, ODT-derived binary masks were segmented using AMIRA ZIB software and the cell volume was extracted by counting the number of voxels.

Data acquisition and analysis were done using custom-written MATLAB scripts (R2019b, MathWorks, Inc.).

Confocal Brillouin epifluorescence microscopy: scattering, setup, imaging and analysis

Brillouin images were acquired employing a two-stage VIPA spectrometer based on the design by Scarcelli *et al.*[58] The spectrometer was attached to a custom-built confocal unit employing a Zeiss Axiovert 200 M microscope stand (Carl Zeiss AG, Germany). A frequency-modulated diode laser with a wavelength of 780.24 nm was used as illumination source. The laser was stabilized to the D2 transition line of Rubidium 85 to block the elastically scattered light. Amplified spontaneous emission (ASE) was suppressed by a Fabry–Pérot interferometer (FPI) (Light Machinery, CA) and a Bragg grating (Ondax NoiseBlock, Ondax, CA). The utilized setup was described in detail by Schlüßler *et al.*,[46] and was slightly modified for the measurements performed here. To further improve the ratio of the intensity of the central laser line to the ASE intensity the alignment of the FPI was changed from a one-pass to a two-pass configuration (Fig. 4), which improved the ASE ratio to 95 dB. The Brillouin setup was controlled with a custom acquisition software written in C++, which stores the data as HDF5 files (https://github.com/BrillouinMicroscopy/BrillouinAcquisition). All images were obtained with a 40×/0.95 air objective (Carl Zeiss AG, Germany). The sample temperature was controlled to 37 °C by a Petri dish heater (JPK BioAFM). Longitudinal modulus and viscosity were derived as previously described.[46]

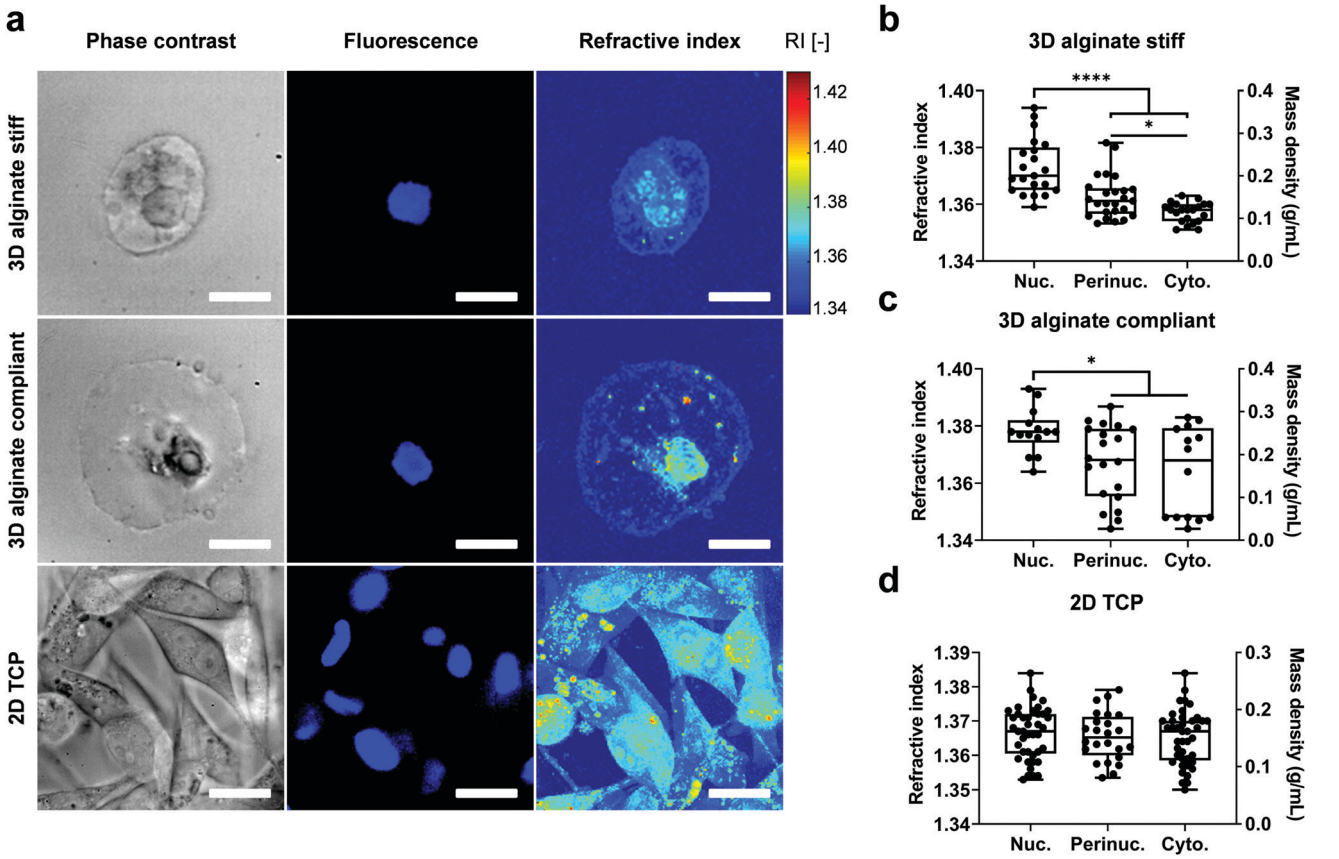

Fig. 3 Mass density distribution between nucleus and cytoplasm is dimensionality-dependent. (a) Epifluorescence images of MDA-MB-231 cells encapsulated in 3D alginate stiff, 3D alginate compliant or on 2D TCP with their corresponding 3D maximum projection tomogram of RI. The epifluorescence images were employed for segmentation of the RI tomogram. Hoechst staining was used for nucleus labelling of cells in 3D alginate groups and the 2D TCP nucleus segmentation was performed based on detectable FUCCI2 signal. (b–d) Quantification of refractive index (RI) and dry mass density (ρ) for nuclear, perinuclear and cytoplasmic regions in 3D alginate stiff, 3D alginate compliant and 2D TCP, respectively. The perinuclear region corresponds to the area in close proximity to the nucleus with 2 μm thickness. Only statistically significant differences were marked. Scale bar equals 10 μm.

Statistical analysis

Experiments were performed with cells on 2D tissue culture plate and 3D encapsulated cells in compliant *vs.* stiff alginate hydrogels. At least three samples per hydrogel group, and multiple cell measurements within each group, were analysed. Box plots showing minimum, maximum, median and interquartile range were used to illustrate the results. Two-tailed student's *t*-test or Mann–Whitney *U*-test were used to statistically compare between normally-distributed or non-parametric groups, respectively (*: $p \leq 0.05$, **: $p \leq 0.01$, ***: $p \leq 0.001$, ****: $p \leq 0.0001$). For multiple group comparison one-way Anova with Tukey's correction or Kruskal–Wallis test with Dunn's correction was conducted. GraphPad Prism 8 software was used to plot the data and for statistical analysis.

Results

Mechanical characterization of 3D alginate hydrogels

To investigate the mechanical and rheological properties of norbornene-modified alginate, frequency sweep experiments were conducted (Fig. 1b). By changing the concentration of the DTT, a stiffness range between 300 Pa and 13 kPa was achieved. The minimum and maximum stiffness-yielding concentrations were selected for further cell encapsulation and will be referred to as compliant and stiff hydrogels, respectively.

3D cell encapsulation, viability and morphological characterization

MDA-MB-231 highly metastatic human breast cancer cells encapsulated in 3D alginate hydrogels remained viable as evidenced by calcein/ethidium homodimer-1 stainings (Fig. S1, ESI†). They remained as single cells, displaying a round morphology after 5 days of encapsulation compared to the more elongated shape of cells on 2D TCP (Fig. 1c).

Refractive index and mass density

To determine intracellular mass density distribution in 3D confined single cells, ODT measurements were performed after staining for the nuclei with Hoechst for cells encapsulated in 3D alginate hydrogels. Following RI tomogram reconstruction, regions associated with nucleus, perinuclear region and cytoplasm were segmented by colocalizing RI tomograms with epifluorescence images (Fig. 3a). Subsequently, the RI and ρ of

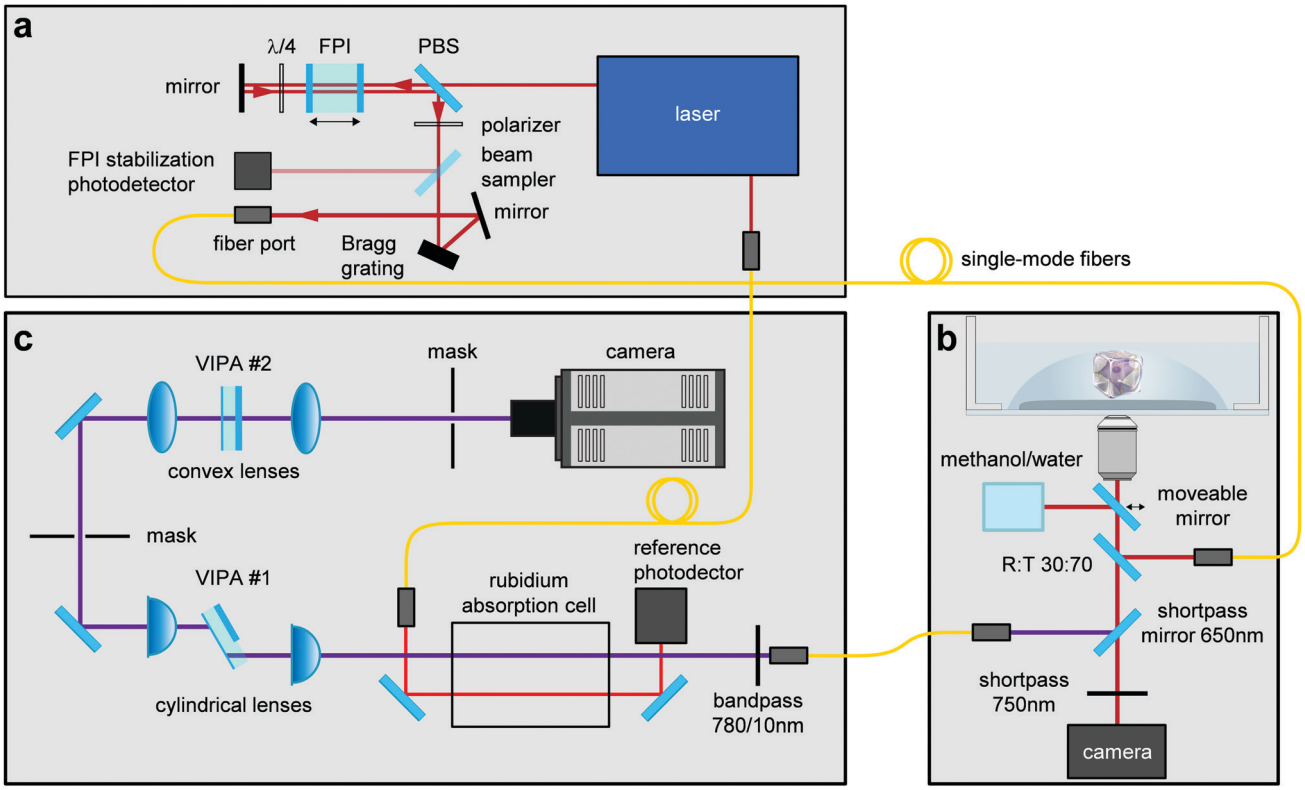

Fig. 4 Combined confocal Brillouin and epifluorescence microscope setup. The different components of this custom-built microscope consist of: (a) illumination source, (b) confocal microscope, (c) Brillouin spectrometer. Abbreviations correspond to FPI = Fabry–Pérot interferometer, PBS = polarizing beam splitter, VIPA = virtually imaged phased array. Image adapted from ref. 46.

the segmented compartments were calculated (Fig. 3b–d). The nuclei in the cells encapsulated in 3D alginate hydrogels displayed higher RI and ρ compared to cytoplasm independent from their stiffness (Fig. 3b and c). In addition, the perinuclear region of cells encapsulated in stiff but not compliant 3D alginate hydrogels was characterised by a higher RI and ρ compared to the cytoplasmic region (Fig. 3b). Notably, RI and ρ values in the cytoplasm and perinuclear regions of cells encapsulated in 3D alginate compliant displayed considerably high variability and dispersion as evidenced by the larger interquartile range (Fig. 3c). Nonetheless, no difference was detected between the absolute values of RI of nuclei, perinucleus or cytoplasm of cells encapsulated in either stiff or compliant 3D alginate hydrogels (Fig. S2a, ESI†). Volume analysis revealed significantly higher volume for cells encapsulated in compliant compared to stiff 3D alginate hydrogels (Fig. S2b, ESI†). The RI and ρ from different sub-cellular regions of cells on 2D TCP did not show any statistical difference (Fig. 3d). Noteworthy, no difference between the nuclear to cytoplasmic ratio of RI and ρ of cells in neither 3D alginate compliant or stiff was detected (Fig. S2c, ESI†).

Longitudinal modulus and viscosity

To investigate the mechanical properties of 3D confined single cells in a non-invasive way, Brillouin measurements were performed after staining for the nucleus. After map reconstruction, regions associated with the nucleus and cytoplasm were segmented based on fluorescence images and their respective Brillouin shift (ν_B) and linewidth (Δ_B) were calculated (Fig. 5a and c). Longitudinal modulus (M) and viscosity (η) were calculated as described previously.[46] Like for RI and ρ, ν_B and the corresponding M of the nucleus for both stiff and compliant 3D alginate were higher than the corresponding values for the cytoplasm (Fig. 5b). Those values were on average greater for both the nucleus and cytoplasm of cells in stiff than in compliant 3D alginate hydrogels (Fig. 5b). The Δ_B and corresponding η of the nucleus was also significantly higher than the values of the cytoplasm for cells in both stiff and compliant hydrogels (Fig. 5d). Noteworthy, in contrast to ν_B, Δ_B and η did not differ between the compliant and stiff 3D alginate hydrogels (Fig. 5d). In addition, the nuclear to cytoplasmic ratio of the ν_B and Δ_B did not reveal any statistical difference among stiff and compliant 3D alginate hydrogels (Fig. S3a and b, ESI†), resembling RI and ρ behaviour. Noteworthy, ν_B, M, Δ_B and η of the nucleus and cytoplasm of cells seeded on 2D TCP didn't display any statistical difference, even though a trend for higher values of the nucleus compared to the cytoplasm could be observed (Fig. S4, ESI†).

Discussion

Using a combined ODT-epifluorescence microscope, to our surprise, we found that human breast cancer cells MDA-MB-231 encapsulated in 3D hydrogels displayed a significantly

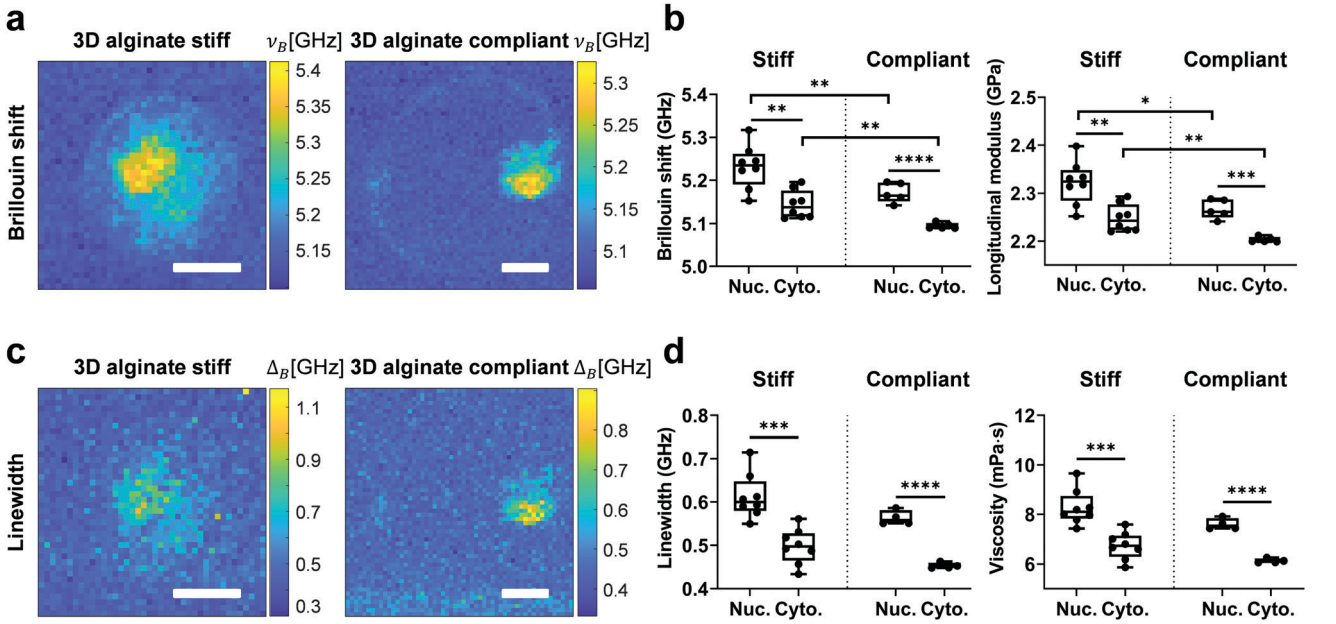

Fig. 5 The nucleus displays higher longitudinal modulus and viscosity than the cytoplasm and the values are matrix stiffness-dependent, with higher values in stiff *vs.* compliant hydrogels. (a) Brillouin shift (ν_B) images of MDA-MB-231 cells encapsulated in 3D alginate stiff (left image) and 3D alginate compliant (right image). Segmentation of cytoplasm and nucleus was performed using brightfield and epifluorescence images. (b) Brillouin shift (ν_B) and corresponding longitudinal modulus (M) quantification for cells in 3D alginate stiff and 3D alginate compliant. (c) Linewidth images (Δ_B) of MDA-MB-231 cells encapsulated in 3D alginate stiff (left image) and 3D alginate compliant (right image). (d) Linewidth (Δ_B) and corresponding viscosity (η) quantification for cells in 3D alginate stiff and 3D alginate compliant. Only statistically significant differences were marked. Scale bar equals 10 μm.

higher nuclear RI and ρ compared to the cytoplasm, irrespective of matrix stiffness. This is different from our 2D results as well as compared to recent 2D data on RI distribution across various cell lines including MDA-MB-231, where it was shown that cells cytoplasm have higher RI than their nuclei using a wide variety of microscopy techniques.[23–28,59,60] Such discrepancy might be attributed to differences in cytoskeletal and/or nuclear morphologies in 2D compared to 3D. Cells on 2D substrates spread out and elongate, displaying a forced ventral-dorsal polarity compared to the non-polarized shape of cells in 3D.[32] Moreover, attachment and spreading on 2D surfaces is accompanied by more pronounced stress fiber formation along the ventral plane, compared to the cortical arrangement of F-actin in 3D.[32] In this scenario, the force sensed by the cell's focal adhesions is tangentially-oriented to the substrate which results in stress propagation along the basal fibers.[61,62] This is in stark contrast to the 3D context, where the less mature focal adhesions and stress fibers are associated to an unpolarized and more round morphology.[32] Here, the cell is exposed to external forces mainly perpendicular to its membrane, which will result in a more isotropic propagation of the stress up to the nucleus.[32] Previous works have shown that cells adherent on 2D substrates display higher nuclear volume and cross-sectional size as well as a more elongated nucleus shape compared to cells encapsulated in 3D hydrogels or on loosely adherent surfaces.[63,64] These differences in cytoskeletal architecture and nuclear shape have distinct signalling implications. In this regard, it has been previously shown that in weakly adhered cells which have reduced stress fiber formation and actomyosin contractility, the histone deacetylases (HDACs) translocates from the cytoplasm to nucleus.[63,65,66] This results in chromatin condensation and compaction with fluid exiting from the nucleus.[63,65,66] Whether this is the reason for the higher nuclear RI and ρ in 3D compared to 2D seen in this study remains to be elucidated. Indeed, it was recently reported that inhibition of chromatin condensation in HeLa cells on 2D substrates results in a reduction of RI and ρ, while inducing chromatin condensation results in the opposite effect.[28]

It has been widely reported that external osmotic pressure modulates chromatin structure and aberrations[67–69] and more recently intracellular mass density.[15] In addition, it was shown that cancer cells under mechanical compression, actively efflux ions to decrease their intracellular tonicity in order to improve their chances of survival.[70] A recent work by the Chaudhuri group showed that stiffer 3D alginate hydrogels induce a tumorigenic phenotype in MCF10A breast epithelial cells by making chromatin sites more accessible.[34] These observations motivate the assumption that 3D matrix-mediated compression could exert an analogous effect as external hyperosmotic pressure. Within this line of reasoning, our study is providing evidence for the effect of alginate-provided 3D mechanical confinement on intracellular mechanical properties, which is reflected in a higher M for both the nucleus and cytoplasm of cells encapsulated in stiff compared to compliant hydrogels. This is in agreement with a recent study where AFM measurements were conducted on isolated MCF-7 spheroids and constituent cells that had been grown in 3D compliant and stiff

polyethylene glycol-heparin hydrogels.[12] Both single cells and spheroids displayed a higher Young's modulus after growth in stiff compared to compliant hydrogels. Interestingly, this effect was mitigated when cells were perturbed with cytochalasin D (F-actin depolymerisation) and Y-27632 (ROCK inhibitor), underlining the importance of F-actin cytoskeleton adaptations in modulating cell mechanics.[12]

Another aspect that can explain the different M between compliant and stiff hydrogels is the cell volume. In a seminal paper from the Weitz group, Guo *et al.*[71] showed that cell cortical and cytoplasmic stiffness scales inversely with their volume in a 2D set-up. Specifically, by increasing external osmotic pressure or substrate stiffness, they observed an increase in cytoplasmic and cortical stiffness coupled with a decrease in cell volume.[71] Similarly, here we show that cells encapsulated in 3D stiff hydrogels display a smaller volume compared to 3D compliant hydrogels, which is reflected in a higher M for both the nucleus and cytoplasm in the former. Remarkably, we show that cells in 2D display an almost double value for M and η compared to cells encapsulated in 3D hydrogels, stressing again on the importance of dimensionality provided by the ECM when assessing mechanical properties of cells.

Noteworthy, viscosity η did not show any statistical difference for the nucleus nor the cytoplasm between compliant and stiff hydrogels. This indicates that, depending on the type of microenvironmental alteration, elastic and viscous properties of the cell might be influenced differently. Indeed, microviscosity of cellular organelles was shown to affect intracellular diffusion and macromolecular crowding.[72] In an elegant study employing molecular rotor-based optical imaging, Chambers *et al.*[72] demonstrated that subjecting cells to hypotonic or hypertonic culture conditions resulted in a respective decrease or increase in the viscosity of the endoplasmic reticulum (ER), mirroring changes in the cytoplasm, while the mitochondria remained relatively unaffected. Interestingly, we show that the cytoplasm of cells adherent on 2D substrates display a considerably higher viscosity compared to cells encapsulated in 3D hydrogels, presumably due to an enhanced stress fiber formation and actomyosin contractility. A similar explanation might hold true for cells embedded in stiff compared to compliant 3D hydrogels, where the cytoplasm in the former group displays higher trends in viscosity than the latter, even though the difference is not statistically significant.

Apart from being contact-free, an important feature of Brillouin spectroscopy is the possibility to extract multiple readouts from both elastic and viscous regimes, which offers additional opportunities not accessible by current conventional methods. Still, care must be taken when interpreting M and η from Brillouin shift measurements. As extensively discussed elsewhere,[43] the spatial and temporal scales of Brillouin measurements are much shorter than conventional AFM, questioning as to whether the frequency range (GHz) at which biomechanical properties are probed is indeed physiologically relevant. In addition, the type of 'stiffness' provided by Brillouin measurements is fundamentally different from the Young's modulus (E). The latter considers the resistance to shape changes where the material is not confined in the direction orthogonal being tested. In contrast, the longitudinal modulus test the elastic resistance while the material is constrained laterally and therefore not allowed to expand. This results in differences between M and E for highly hydrated ($>90\%$) materials,[73] as M is more sensitive to changes in the mechanical properties of the liquid component in a material than E. Nonetheless, cells do not fall under this category ($\sim$60–80% water content).[43] This was shown by a comparative study, where fibroblasts were subjected to mechanical and cytoskeletal perturbations, after which they displayed comparable variation of Brillouin shifts and AFM Young's moduli.[45] That being said, improving instrument sensitivity will increasingly facilitate the detection of even small variations in the compressibility properties of different components.[43,74]

Recent efforts are pointing towards liquid–solid-like transition processes participating in the local increase of intracellular ρ, which was shown to contribute to the stiffening of the cytoplasm and growth arrest in yeast cells.[13,15] Likewise, how the nucleus and cytoplasm in cells interact with each other, and in what way such an interplay is influenced by extracellular cues, is still an underexplored field. One reason is the practical inaccessibility in a non-invasive way using conventional instruments. With the advent of state-of-the-art optical techniques such as ODT and Brillouin microscopy, it will become easier to address such questions in a non-invasive manner.

Conclusions

The effect of ECM-provided dimensionality is being increasingly recognized in cell biology. Nonetheless, less is known about its effect on sub-cellular ρ distribution and the potential physiological changes it might accompany. Using a combined epifluorescence-ODT setup, we showed that MDA-MB-231 cells encapsulated in 3D alginate hydrogels display a higher RI and ρ in the nucleus than the cytoplasm, which is different to the situation where the cells adhere to 2D substrates. This RI and ρ distribution coincides with a higher M and η for the nucleus than the cytoplasm, measured using a confocal Brillouin-epifluorescence microscope. Furthermore, the nucleus and cytoplasm of cells encapsulated in stiff 3D alginate hydrogels displayed higher M and η compared to cells in compliant 3D alginate hydrogels. Changes in biophysical properties such as intracellular osmolarity, cytoplasmic/nuclear stiffening and mass distribution have been associated with alterations of cell growth and division. Deregulation of these processes have been linked to various diseases; nevertheless, little is known about the underlying mechanisms governing such alterations. Even less is understood about the role of microenvironmental changes in this context. The ability to visualize and quantify intracellular biophysical properties at the single-cell level with non-invasive techniques is a first and important step towards better understanding of a wide variety of biological processes, in particular those associated with alterations in ρ distribution, such as dormancy, apoptosis, cell growth or stem cell differentiation.

Conflicts of interest

There are no conflicts to declare.

Acknowledgements

This work was funded by the Deutsche Forschungsgemeinschaft (DFG) Emmy Noether grant (CI 203/2-1 to A. C.), a DFG research grant (GU 612/8-1 to J. G.), a "Life? A Fresh Scientific Approach to the Basic Principles of Life" research grant from the Volkswagen Foundation (92847 to J. G.), and an Alexander von Humboldt Professorship (to J. G.). A. T. is fellow of the Mildred Scheel Early Career Center Dresden funded by the German Cancer Aid (Deutsche Krebshilfe). H. M. T. thanks the International Max Planck Research School (IMPRS) on Multiscale Bio Systems for financial support. Additionally, the authors would like to acknowledge Peter Fratzl for scientific discussion.

References

1 D. Di Carlo, *J. Lab. Autom.*, 2012, **17**, 32–42.
2 E. M. Darling and D. Di Carlo, *Annu. Rev. Biomed. Eng.*, 2015, **17**, 35–62.
3 M. Urbanska, M. Winzi, K. Neumann, S. Abuhattum, P. Rosendahl, P. Müller, A. Taubenberger, K. Anastassiadis and J. Guck, *Development*, 2017, **144**, 4313–4321.
4 J. Lin, D. Kim, H. T. Tse, P. Tseng, L. Peng, M. Dhar, S. Karumbayaram and D. Di Carlo, *Microsyst. Nanoeng.*, 2017, **3**, 17013.
5 C. J. Chan, C.-P. Heisenberg and T. Hiiragi, *Curr. Biol.*, 2017, **27**, R1024–R1035.
6 T. Mammoto and D. E. Ingber, *Development*, 2010, **137**, 1407–1420.
7 J. C. Benech, N. Benech, A. I. Zambrana, I. Rauschert, V. Bervejillo, N. Oddone and J. P. Damián, *Am. J. Physiol.: Cell Physiol.*, 2014, **307**, C910–C919.
8 A. E. Ekpenyong, G. Whyte, K. Chalut, S. Pagliara, F. Lautenschläger, C. Fiddler, S. Paschke, U. F. Keyser, E. R. Chilvers and J. Guck, *PLoS One*, 2012, **7**, e45237.
9 J. Guck, S. Schinkinger, B. Lincoln, F. Wottawah, S. Ebert, M. Romeyke, D. Lenz, H. M. Erickson, R. Ananthakrishnan, D. Mitchell, J. Käs, S. Ulvick and C. Bilby, *Biophys. J.*, 2005, **88**, 3689–3698.
10 C. N. Holenstein, A. Horvath, B. Schär, A. D. Schoenenberger, M. Bollhalder, N. Goedecke, G. Bartalena, O. Otto, M. Herbig, J. Guck, D. A. Müller, J. G. Snedeker and U. Silvan, *Mol. Biol. Cell*, 2019, **30**, 887–898.
11 V. Swaminathan, K. Mythreye, E. T. O'Brien, A. Berchuck, G. C. Blobe and R. Superfine, *Cancer Res.*, 2011, **71**, 5075–5080.
12 A. V. Taubenberger, S. Girardo, N. Träber, E. Fischer-Friedrich, M. Kräter, K. Wagner, T. Kurth, I. Richter, B. Haller, M. Binner, D. Hahn, U. Freudenberg, C. Werner and J. Guck, *Adv. Biosyst.*, 2019, **1900128**, 1900128.
13 M. C. Munder, D. Midtvedt, T. Franzmann, E. Nüske, O. Otto, M. Herbig, E. Ulbricht, P. Müller, A. Taubenberger, S. Maharana, L. Malinovska, D. Richter, J. Guck, V. Zaburdaev and S. Alberti, *eLife*, 2016, **5**, 1–30.
14 S. Toné, K. Sugimoto, K. Tanda, T. Suda, K. Uehira, H. Kanouchi, K. Samejima, Y. Minatogawa and W. C. Earnshaw, *Exp. Cell Res.*, 2007, **313**, 3635–3644.
15 S. Abuhattum, K. Kim, T. M. Franzmann, A. Eßlinger, D. Midtvedt, R. Schlüßler, S. Möllmert, H.-S. Kuan, S. Alberti, V. Zaburdaev and J. Guck, *Front. Phys.*, 2018, **6**, 131.
16 G. Popescu, Y. Park, N. Lue, C. Best-Popescu, L. Deflores, R. R. Dasari, M. S. Feld and K. Badizadegan, *Am. J. Physiol.: Cell Physiol.*, 2008, **295**, C538–C544.
17 H. G. Davies and M. H. F. Wilkins, *Nature*, 1952, **169**, 541.
18 P. Y. Liu, L. K. Chin, W. Ser, H. F. Chen, C.-M. Hsieh, C.-H. Lee, K.-B. Sung, T. C. Ayi, P. H. Yap, B. Liedberg, K. Wang, T. Bourouina and Y. Leprince-Wang, *Lab Chip*, 2016, **16**, 634–644.
19 P. M. A. Sloot, A. G. Hoekstra and C. G. Figdor, *Cytometry*, 1988, **9**, 636–641.
20 A. Brunsting and P. F. Mullaney, *Biophys. J.*, 1974, **14**, 439–453.
21 R. Drezek, M. Guillaud, T. Collier, I. Boiko, A. Malpica, C. Macaulay, M. Follen and R. R. Richards-Kortum, *J. Biomed. Opt.*, 2003, **8**, 7.
22 V. V. Tuchin, *J. Biomed. Opt.*, 1997, **2**, 401.
23 M. Schürmann, J. Scholze, P. Müller, J. Guck and C. J. Chan, *J. Biophotonics*, 2016, **9**, 1068–1076.
24 Z. A. Steelman, W. J. Eldridge, J. B. Weintraub and A. Wax, *J. Biophotonics*, 2017, **10**, 1714–1722.
25 R. Imai, T. Nozaki, T. Tani, K. Kaizu, K. Hibino, S. Ide, S. Tamura, K. Takahashi, M. Shribak and K. Maeshima, *Mol. Biol. Cell*, 2017, **28**, 3349–3359.
26 H. Hassani and E. Kreysing, *Opt. Lett.*, 2019, **44**, 1359.
27 N. J. Mudrak, P. S. Rana and M. A. Model, *Cytometry, Part A*, 2018, **93**, 297–304.
28 K. Kim and J. Guck, *Biophys. J.*, 2020, **119**(10), 1946–1957.
29 P. A. Kenny, G. Y. Lee, C. A. Myers, R. M. Neve, J. R. Semeiks, P. T. Spellman, K. Lorenz, E. H. Lee, M. H. Barcellos-Hoff, O. W. Petersen, J. W. Gray and M. J. Bissell, *Mol. Oncol.*, 2007, **1**, 84–96.
30 N. Huebsch, P. R. Arany, A. S. Mao, D. Shvartsman, O. A. Ali, S. A. Bencherif, J. Rivera-Feliciano and D. J. Mooney, *Nat. Mater.*, 2010, **9**, 518–526.
31 S. Raghavan, C. J. Shen, R. A. Desai, N. J. Sniadecki, C. M. Nelson and C. S. Chen, *J. Cell Sci.*, 2010, **123**, 2877–2883.
32 B. M. Baker and C. S. Chen, *J. Cell Sci.*, 2012, **125**, 3015–3024.
33 N. Huebsch, P. R. Arany, A. S. Mao, D. Shvartsman, O. A. Ali, S. A. Bencherif, J. Rivera-Feliciano and D. J. Mooney, *Nat. Mater.*, 2010, **9**, 518–526.
34 R. S. Stowers, A. Shcherbina, J. Israeli, J. J. Gruber, J. Chang, S. Nam, A. Rabiee, M. N. Teruel, M. P. Snyder, A. Kundaje and O. Chaudhuri, *Nat. Biomed. Eng.*, 2019, **3**(12), 1009–1019.
35 O. Chaudhuri, L. Gu, M. Darnell, D. Klumpers, S. A. Bencherif, J. C. Weaver, N. Huebsch and D. J. Mooney, *Nat. Commun.*, 2015, **6**, 6365.

36 O. Chaudhuri, L. Gu, D. Klumpers, M. Darnell, S. A. Bencherif, J. C. Weaver, N. Huebsch, H. Lee, E. Lippens, G. N. Duda and D. J. Mooney, *Nat. Mater.*, 2016, **15**, 326–334.
37 O. Chaudhuri, J. Cooper-White, P. A. Janmey, D. J. Mooney and V. B. Shenoy, *Nature*, 2020, **584**, 535–546.
38 A. Lueckgen, D. S. Garske, A. Ellinghaus, D. J. Mooney, G. N. Duda and A. Cipitria, *Biomaterials*, 2019, **217**, 119294.
39 A. Lueckgen, D. S. Garske, A. Ellinghaus, R. M. Desai, A. G. Stafford, D. J. Mooney, G. N. Duda and A. Cipitria, *Biomaterials*, 2018, **181**, 189–198.
40 M. Krieg, G. Fläschner, D. Alsteens, B. M. Gaub, W. H. Roos, G. J. L. Wuite, H. E. Gaub, C. Gerber, Y. F. Dufrêne and D. J. Müller, *Nat. Rev. Phys.*, 2019, **1**, 41–57.
41 R. M. Hochmuth, *J. Biomech.*, 2000, **33**, 15–22.
42 H. Zhang and K.-K. Liu, *J. R. Soc., Interface*, 2008, **5**, 671–690.
43 R. Prevedel, A. Diz-Muñoz, G. Ruocco and G. Antonacci, *Nat. Methods*, 2019, **16**, 969–977.
44 G. Antonacci, T. Beck, A. Bilenca, J. Czarske, K. Elsayad, J. Guck, K. Kim, B. Krug, F. Palombo, R. Prevedel and G. Scarcelli, *Biophys. Rev.*, 2020, **12**(3), 615–624.
45 G. Scarcelli, W. J. Polacheck, H. T. Nia, K. Patel, A. J. Grodzinsky, R. D. Kamm and S. H. Yun, *Nat. Methods*, 2015, **12**, 1132–1134.
46 R. Schlüßler, S. Möllmert, S. Abuhattum, G. Cojoc, P. Müller, K. Kim, C. Möckel, C. Zimmermann, J. Czarske and J. Guck, *Biophys. J.*, 2018, **115**, 911–923.
47 O. Chaudhuri, S. T. Koshy, C. Branco da Cunha, J.-W. Shin, C. S. Verbeke, K. H. Allison and D. J. Mooney, *Nat. Mater.*, 2014, **13**, 970–978.
48 S. T. Gould, N. J. Darling and K. S. Anseth, *Acta Biomater.*, 2012, **8**, 3201–3209.
49 A. Sakaue-Sawano, T. Kobayashi, K. Ohtawa and A. Miyawaki, *BMC Cell Biol.*, 2011, **12**, 2.
50 K. Kim, W. S. Park, S. Na, S. Kim, T. Kim, W. Do Heo and Y. Park, *Biomed. Opt. Express*, 2017, **8**, 5688.
51 E. Cuche, P. Marquet and C. Depeursinge, *Appl. Opt.*, 2000, **39**, 4070.
52 E. Wolf, *Opt. Commun.*, 1969, **1**, 153–156.
53 Y. Sung, W. Choi, C. Fang-Yen, K. Badizadegan, R. R. Dasari and M. S. Feld, *Opt. Express*, 2009, **17**, 266.
54 K. Kim, H. Yoon, M. Diez-Silva, M. Dao, R. R. Dasari and Y. Park, *J. Biomed. Opt.*, 2013, **19**, 1.
55 P. Müller, M. Schürmann and J. Guck, *The Theory of Diffraction Tomography*, 2016, arXiv:1507.00466v3.
56 H. Zhao, P. H. Brown and P. Schuck, *Biophys. J.*, 2011, **100**, 2309–2317.
57 T. A. Zangle and M. A. Teitell, *Nat. Methods*, 2014, **11**, 1221–1228.
58 G. Scarcelli and S. H. Yun, *Opt. Express*, 2011, **19**, 10913.
59 J. Lee, H. Kim, H. Cho, Y. Jo, Y. Song, D. Ahn, K. Lee, Y. Park and S.-J. Ye, *IEEE Access*, 2019, **7**, 83449–83460.
60 W. Sung, Y. Jeong, H. Kim, H. Jeong, C. Grassberger, S. Jung, G.-O. Ahn, I. H. Kim, J. Schuemann, K. Lee and S.-J. Ye, *Radiat. Res.*, 2018, **190**, 558.
61 M. Dembo and Y.-L. Wang, *Biophys. J.*, 1999, **76**, 2307–2316.
62 J. L. Tan, J. Tien, D. M. Pirone, D. S. Gray, K. Bhadriraju and C. S. Chen, *Proc. Natl. Acad. Sci. U. S. A.*, 2003, **100**, 1484–1489.
63 F. Alisafaei, D. S. Jokhun, G. V. Shivashankar and V. B. Shenoy, *Proc. Natl. Acad. Sci. U. S. A.*, 2019, **116**, 13200–13209.
64 J. Y. Lee, J. K. Chang, A. A. Dominguez, H. Lee, S. Nam, J. Chang, S. Varma, L. S. Qi, R. B. West and O. Chaudhuri, *Nat. Commun.*, 2019, **10**, 1848.
65 K. Damodaran, S. Venkatachalapathy, F. Alisafaei, A. V. Radhakrishnan, D. Sharma Jokhun, V. B. Shenoy and G. V. Shivashankar, *Mol. Biol. Cell*, 2018, **29**, 3039–3051.
66 N. Jain, K. V. Iyer, A. Kumar and G. V. Shivashankar, *Proc. Natl. Acad. Sci. U. S. A.*, 2013, **110**, 11349–11354.
67 S. M. Galloway, D. A. Deasy, C. L. Bean, A. R. Kraynak, M. J. Armstrong and M. O. Bradley, *Mutat. Res.*, 1987, **189**, 15–25.
68 A. L. Olins, T. J. Gould, L. Boyd, B. Sarg and D. E. Olins, *Nucleus*, 2020, **11**, 1–18.
69 A. F. Lima, G. May, J. Díaz-Colunga, S. Pedreiro, A. Paiva, L. Ferreira, T. Enver, F. J. Iborra and R. Pires das Neves, *Sci. Rep.*, 2018, **8**, 7210.
70 D. J. McGrail, K. M. McAndrews, C. P. Brandenburg, N. Ravikumar, Q. M. N. Kieu and M. R. Dawson, *Biophys. J.*, 2015, **109**, 1334–1337.
71 M. Guo, A. F. Pegoraro, A. Mao, E. H. Zhou, P. R. Arany, Y. Han, D. T. Burnette, M. H. Jensen, K. E. Kasza, J. R. Moore, F. C. Mackintosh, J. J. Fredberg, D. J. Mooney, J. Lippincott-Schwartz and D. A. Weitz, *Proc. Natl. Acad. Sci. U. S. A.*, 2017, **114**, E8618–E8627.
72 J. E. Chambers, M. Kubánková, R. G. Huber, I. López-Duarte, E. Avezov, P. J. Bond, S. J. Marciniak and M. K. Kuimova, *ACS Nano*, 2018, **12**, 4398–4407.
73 P.-J. Wu, I. V. Kabakova, J. W. Ruberti, J. M. Sherwood, I. E. Dunlop, C. Paterson, P. Török and D. R. Overby, *Nat. Methods*, 2018, **15**, 561–562.
74 P. Shao, T. G. Seiler, A. M. Eltony, A. Ramier, S. J. J. Kwok, G. Scarcelli, R. Pineda II and S.-H. Yun, *Invest. Ophthalmol. Vis. Sci.*, 2018, **59**, 3020.

Supplementary information

Optical quantification of intracellular mass density and cell mechanics in 3D mechanical confinement

Sadra Bakhshandeh[a], Hubert M. Taïeb [a], Raimund Schlüßler[b], Kyoohyun Kim[b,c], Timon Beck[b,c], Anna Taubenberger[b], Jochen Guck*[b,c] and Amaia Cipitria*[a]

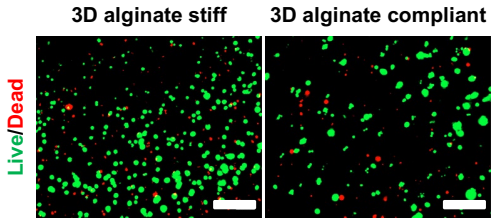

Fig. S1 MDA-MB-231 retain high viability after 5 days of encapsulation. Live/Dead images of MDA-MB-231 cells encapsulated in 3D alginate stiff (left image) and 3D alginate compliant (right image) after 5 days. Green (calcein) and red (ethidium homodimer-1) correspond to live and dead cells respectively. Scale bar equals 200 µm.

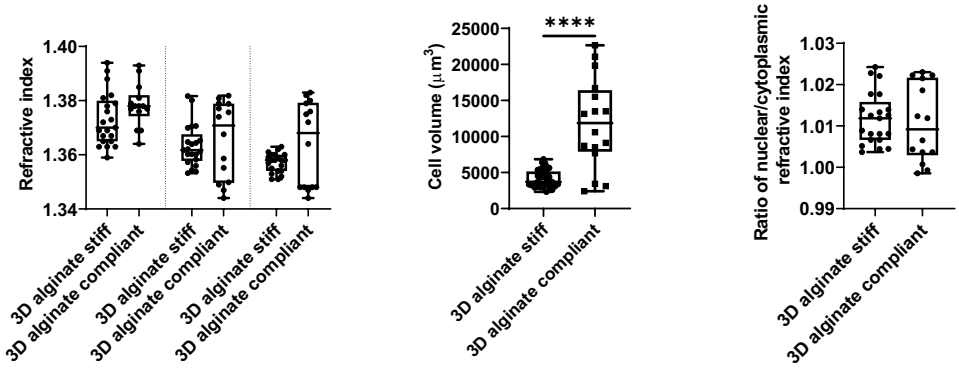

Fig. S2 Comparison of RI, cell volume and ratio of nuclear to cytoplasmic RI among cells encapsulated in stiff and compliant 3D alginate hydrogels. **a)** Comparison of nuclear, perinuclear and cytoplasmic RI among cells encapsulated in stiff and compliant 3D alginate hydrogels. **b)** Comparison of volume of cells encapsulated in stiff and compliant 3D alginate hydrogels. **c)** Ratio of nuclear to cytoplasmic RI for cells in 3D alginate stiff and compliant hydrogels. Only statistically significant differences are marked.

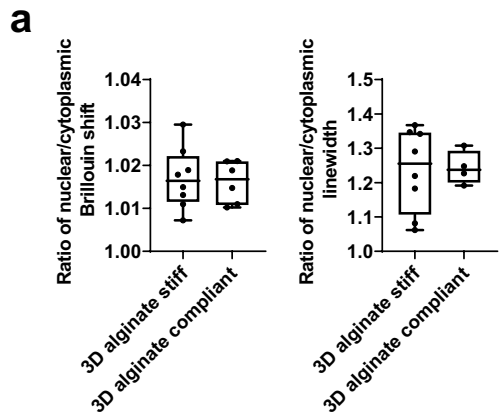

Fig. S3 Nuclear to cytoplasmic ratio of Brillouin shift and linewidth among cells encapsulated in stiff and compliant 3D alginate hydrogels. Ratio of nuclear to cytoplasmic **a)** Brillouin shift and **b)** linewidth for cells in 3D alginate stiff and compliant hydrogels. Only statistically significant differences are marked.

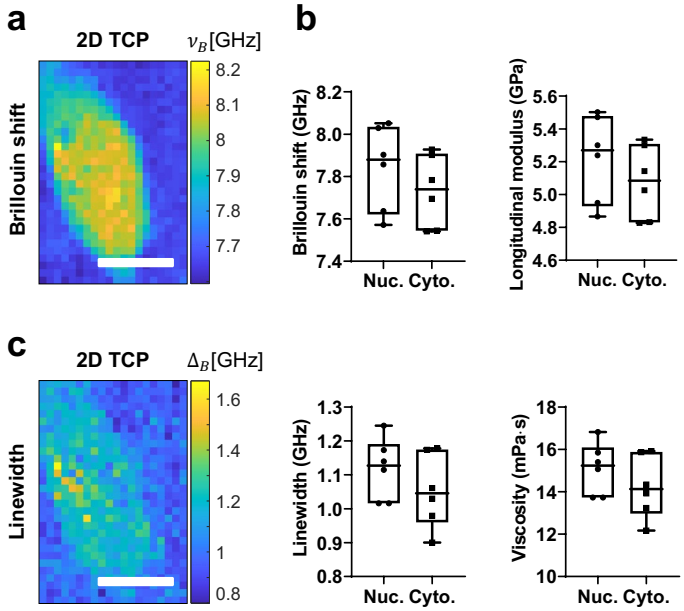

Fig. S4 Brillouin measurements of cells seeded on 2D TCP. a) Brillouin shift ($\boldsymbol{\nu_B}$) images of MDA-MB-231 cells seeded on 2D TCP. Segmentation of cytoplasm and nucleus was performed using brightfield and epifluorescence images, respectively. **b)** Brillouin shift ($\boldsymbol{\nu_B}$) and corresponding longitudinal modulus (M) quantification for cells seeded on 2D TCP. **c)** Linewidth images (Δ_B) of MDA-MB-231 cells seeded on 2D TCP. **d)** Linewidth (Δ_B) and corresponding viscosity (η) quantification for cells seeded on 2D TCP. Only statistically significant differences are marked. Scale bar equals 10 µm.

4.4 Insights into intracellular organelle distribution using Focused Ion Beam Electron Microscopy (FIB-SEM)

4.4.1 Overview

To gain further insight into intracellular organelle distribution we took advantage of Focused Ion Beam Electron Microscopy (FIB-SEM), a tool used to visualize (intra-)cellular architecture in three dimension (3D) at high resolution (up to nanometer scales) via surface milling [91]. One recent advancement has been the ability to image at cryo conditions via amorphous ice embedding techniques, ensuring better preservation of biological materials [92]. Combining cryo and FIB-SEM have been already established for cells on 2D [93], but not for cells within a more biologically faithful 3D settings. Thus, we decided to image cells encapsulated in natural extracellular matrix (ECM), in this case ligand-rich basement membrane derived Matrigel with cryo-FIB-SEM.

4.4.2 Methods

Cryo-fixation, or to be more accurate, vitrification, is the physical process through which water solidifies into an amorphous (non-crystalline) phase of ice, which, in our case, is induced by high-pressure freezing [92]. This is of utmost importance to ensure proper preservation of biological materials, as, in the case of cells, for instance, growing ice crystals are known to absorb the water present in the cytoplasm causing dehydration and destruction of the sample's microstructure [92]. This was achieved by using a high-pressure-freezing EM PACT2 device (Leica-Microsystems) by directly plunging pieces of cells encapsulated in Matrigel into the machine. The vitrified samples were then collected in liquid nitrogen to be later imaged with cryo-FIB-SEM (Carl Zeiss Microsystems GmbH, Oberkochen, Germany). The latter combines ion and electron beams enabling monitoring of the milling process conducted by electrons in a serial slicing (FIB) and imaging (SEM) fashion, providing stacks of images for further 3D reconstruction [91, 93] (Fig.4.1).

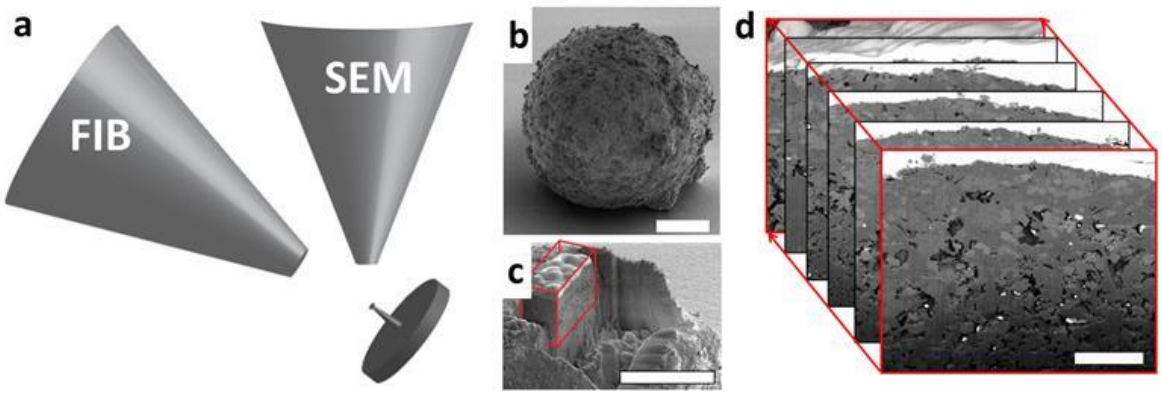

Figure 4.1: FIB-SEM enables milling/slicing (FIB) and imaging (SEM) in a serial manner for further 3D reconstruction. Images from www.chemistryworld.com.

4.4.3 Results and discussion

Remarkably, without any exogenous labeling, we were able to identify different organelles in the cell with distinct shape and contrast (Fig.4.2). Furthermore, the inherent contrast of each organelle matches typical refractive index values reported using different optical techniques [94], hinting at the possibility of using cryo-FIB-SEM as a method to measure intracellular mass density, among others. Overall, the data here illustrates the potential of using cryo-FIB-SEM to observe the detailed intracellular architecture of cells in a 3D environment in their most close-to-native condition. Nonetheless, due to hurdles associated with sample preparation and cell detection, along with high instability of the device and lengthy manual image processing and analysis, we decided not to pursue this further. Despite that, with a robust sample preparation as well as an automated artificial intelligence-based image segmentation pipeline, cryo-FIB-SEM could provide cellular details at resolutions hardly achievable with conventional fluorescence-based microscopy.

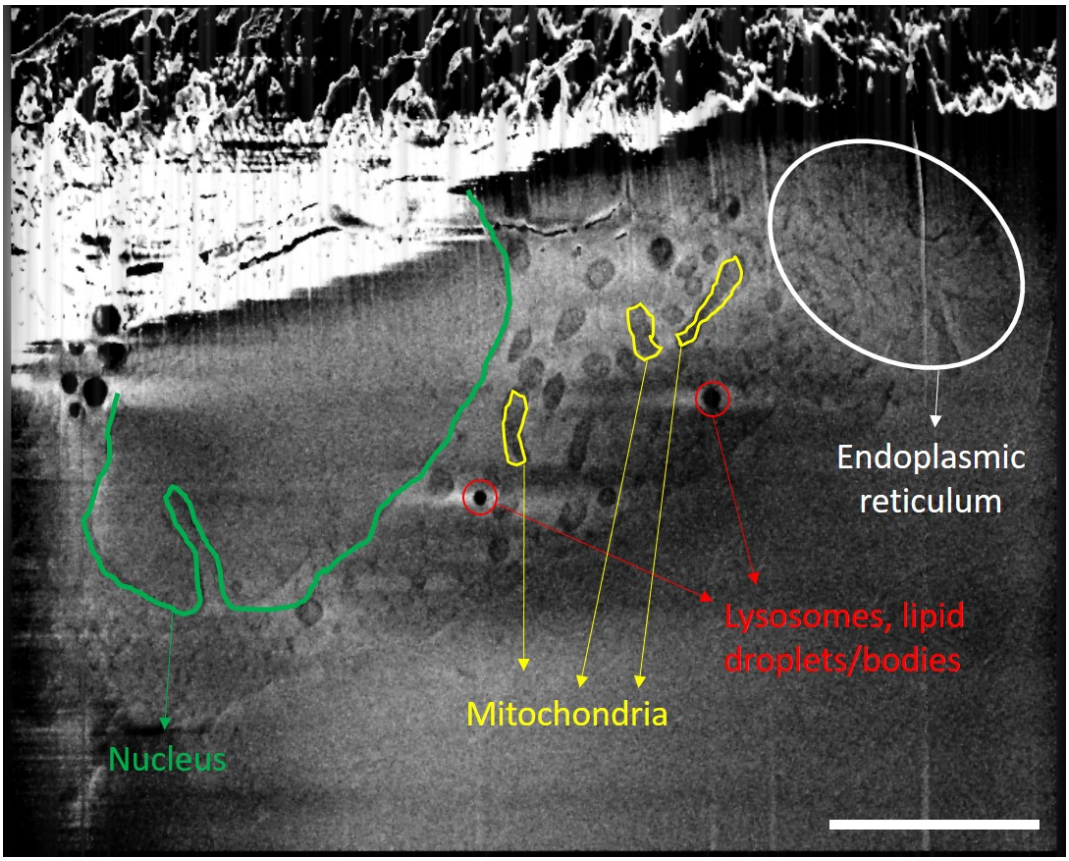

Figure 4.2: Slice of FIB-SEM image of an MDA-MB-231 cell encapsulated in 3D Matrigel hydrogels with correspondingly indicated organelles. Scale bar equals 5µm.

5

Organotypic model of breast cancer bone metastasis

5.1 Briefing of methods, results and discussion

To look at cell cycle progression in breast cancer cells disseminated to the bone marrow in a more physiologically relevant in vitro system, we teamed with the group of Dr. Mark Rosowski at the TU Berlin. They had previously developed a bone-marrow-mimicking 3D culture model including primary mesenchymal stromal cells (MSCs) and hematopoietic stem and progenitor cells (HSPCs). With the help of a master student, Ms. Sanem Özayral, we included into their model a breast cancer cell line genetically modified with the cell cycle reporter FUCCI2 and observed cell cycle progression and niche homing preference. Most of the results are still preliminary as this was part of a master thesis project. We nevertheless decided to report the most relevant and reliable set of data as we believe they provide significant insight into the role of the bone microenvironment on breast cancer metastasis.

We genetically modified MDA-MB-231 FUCCI2 (fluorescence ubiquitination cell cycle indicator-2) [95] as breast cancer cell (BCC) cycle reporter (Fig.5.1) and seeded them in a 3D hydroxyapatite coated zirconium oxide scaffold pre-seeded with primary human mesenchymal stromal cells (MSCs) and human cord blood-derived multipotent HSPCs [76] (Fig.1.6). We then observed MDA-MB-231 FUCCI2 cells localization and interaction within the MSCs-derived fibronectin extracellular matrix network using immunofluorescence. Remarkably, MDA-MB-231 FUCCI2 were observed to be entrapped within the fibronectin network, with significant prevalence for the G0/G1 state (mCherry+), pointing to a likely growth arrest-inducing effect of the bone microenvironments (Fig.5.2). Please refer to Sanem Özayral's master thesis entitled "Breast cancer cell cycle progression in a 3D bone marrow mimicking system" at Ulm University repository for further details.

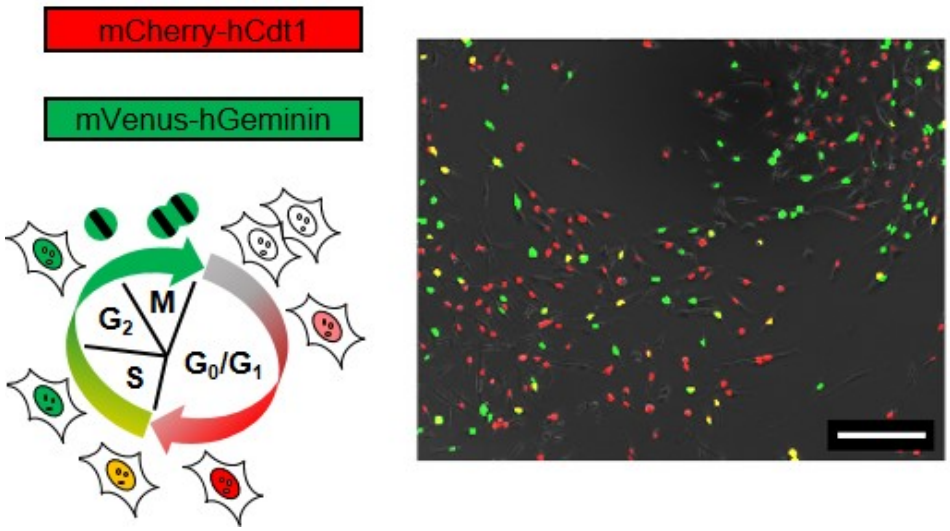

Figure 5.1: Schematic of FUCCI2 cell cycle reporter. Cells in the G0/G1 state of the cell cycle express a spectrum of mCherry signal depending on how far they are through this stage, while cells in the S/G2/M state express mVenus. The image on the right shows MDA-MB-231 FUCCI2 cells. Scale bar equals 200µm.

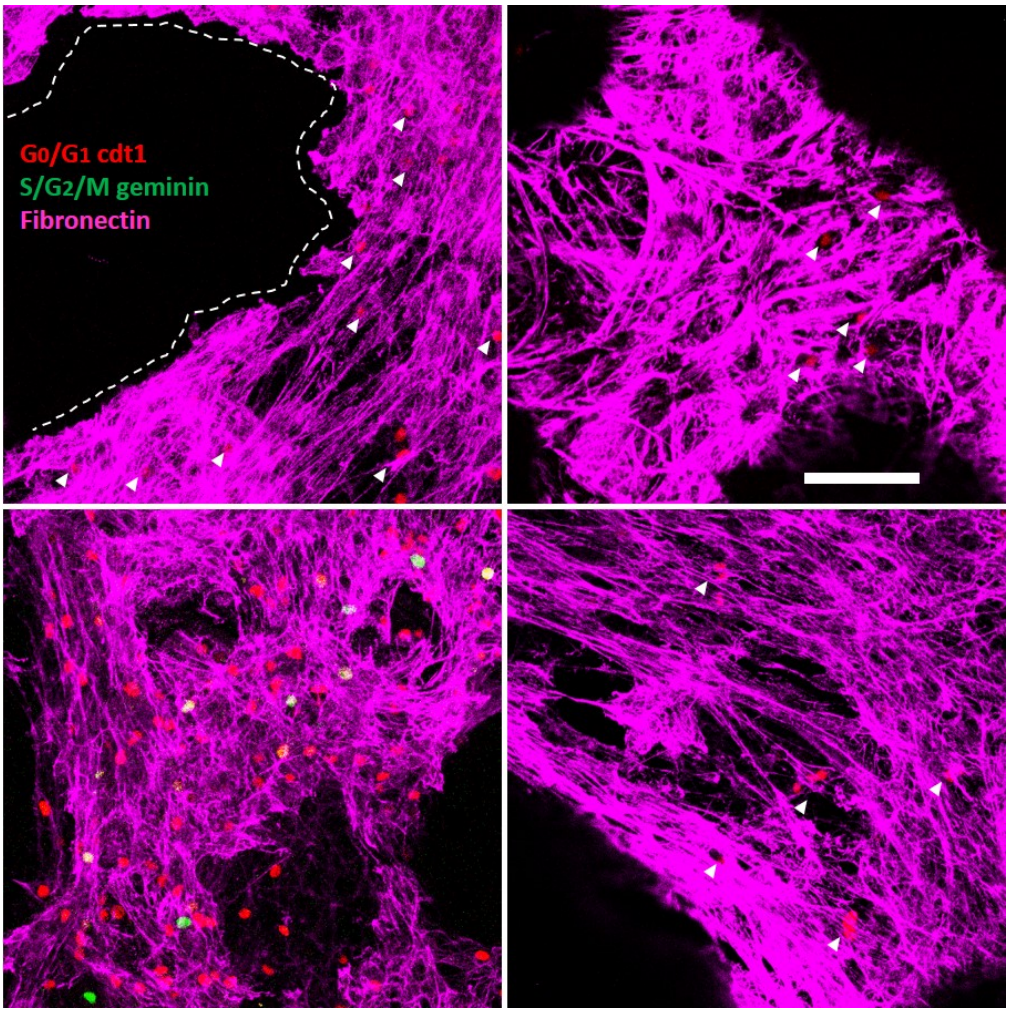

Figure 5.2: Schematic of FUCCI2 cell cycle reporter. Cells in the G0/G1 state of the cell cycle express a spectrum of mCherry signal depending on how far they are through this stage, while cells in the S/G2/M state express mVenus. The image on the right shows MDA-MB-231 FUCCI2 cells. Scale bar equals 200µm.

6

Publication III: Microenvironment-mediated cancer dormancy: insights from metastability theory

6.1 Transition

To provide a more global description of the process of microenvironment-mediated dormancy, we took advantage of well-known thermodynamic concepts of wetting, phase separation and (meta)stability theory of a growing droplet. Inspired by experimental data, we simplistically model three distinct types of interaction, namely adhesion, mechanical confinement and size-dependent limited growth due to lack of nutrients and oxygen. We postulated that the emergence of metastable states (local energy minima) in the growth kinetics of a droplet under the above-mentioned conditions could be considered as a proxy of dormancy. The tendency of the droplet to remain in this state is influenced by microenvironmental fluctuations and perturbations which may or may not provide the energy required to overcome this energy valley (also known as energy barrier), thereby enabling or hindering the droplet's growth progression.

6.2 Personal contribution

For this publication, Prof. Peter Fratzl raised the idea of dormancy sharing several parallels with metastable states, together with providing analytical data and its interpretation for the growth kinetics of a droplet under different conditions. Contextualization with respect to experimental and clinical data was conducted with the support of all co-authors. I further

generated the figures, and wrote the manuscript.

6.3 Publication notification

This work was published in the journal *Proceedings of the National Academy of Sciences of the United States of America (PNAS)* in January 2022 and is available at https://doi.org/10.1073/pnas.2111046118.

"Microenvironment-mediated cancer dormancy: insights from metastability theory"

Sadra Bakhshandeh, Carsten Werner, Peter Fratzl, Amaia Cipitria

PERSPECTIVE

Microenvironment-mediated cancer dormancy: Insights from metastability theory

Sadra Bakhshandeh[a], Carsten Werner[b,c], Peter Fratzl[a,1], and Amaia Cipitria[a,1]

Edited by David Weitz, Department of Physics Division of Engineering and Applied Science, Harvard University, Cambridge, MA; received July 5, 2021; accepted November 14, 2021

Dormancy is an evolutionarily conserved protective mechanism widely observed in nature. A pathological example is found during cancer metastasis, where cancer cells disseminate from the primary tumor, home to secondary organs, and enter a growth-arrested state, which could last for decades. Recent studies have pointed toward the microenvironment being heavily involved in inducing, preserving, or ceasing this dormant state, with a strong focus on identifying specific molecular mechanisms and signaling pathways. Increasing evidence now suggests the existence of an interplay between intracellular as well as extracellular biochemical and mechanical cues in guiding such processes. Despite the inherent complexities associated with dormancy, proliferation, and growth of cancer cells and tumor tissues, viewing these phenomena from a physical perspective allows for a more global description, independent from many details of the systems. Building on the analogies between tissues and fluids and thermodynamic phase separation concepts, we classify a number of proposed mechanisms in terms of a thermodynamic metastability of the tumor with respect to growth. This can be governed by interaction with the microenvironment in the form of adherence (wetting) to a substrate or by mechanical confinement of the surrounding extracellular matrix. By drawing parallels with clinical and experimental data, we advance the notion that the local energy minima, or metastable states, emerging in the tissue droplet growth kinetics can be associated with a dormant state. Despite its simplicity, the provided framework captures several aspects associated with cancer dormancy and tumor growth.

cancer dormancy | metastability | tissue growth | phase separation | extracellular matrix

Cell and tissue growth is tightly regulated by intracellular as well as extracellular mechanisms. The latter, comprising both cell–cell and cell–extracellular matrix (ECM) interactions, provides a wide variety of biochemical and biophysical signals, which critically affect growth kinetics and fate (1). In particular, the physical/mechanical role of the surrounding microenvironment is being increasingly recognized in many physiological processes such as stem cell maintenance, differentiation (2), and tissue morphogenesis and adaptation (3, 4), as well as pathological conditions like tumor progression (5, 6). Nonetheless, the focus of most studies has overwhelmingly weighed toward the role of specific genes and proteins involved in these processes and less toward providing a physical framework for a more global description. This is hardly surprising, considering the complexity of biological systems.

From a thermodynamic point of view, living entities are considered "open systems" lying in a highly unpredictable "far-from-equilibrium" state, as opposed to their nonliving counterparts (7). Nonetheless, thermodynamic phase transitions occurring in open physical systems, such as the Bénard instability or the Belousov–Zhabotinski chemical reaction, where stationary states emerge by virtue of energy and material exchange with the environment, have prompted physicists to compare certain aspects of biological systems with thermodynamic phase transitions and metastable or critical states (8–12). Such parallels range from associating healthy-to-cancerous transformations, epithelial-to-mesenchymal transitions, and tumor invasion with

[a]Department of Biomaterials, Max Planck Institute of Colloids and Interfaces, 14476 Potsdam, Germany; [b]Leibniz-Institut für Polymerforschung Dresden, Max Bergmann Center of Biomaterials, 01069 Dresden, Germany; and [c]Center for Regenerative Therapies, Technische Universität Dresden, 01069 Dresden, Germany

Author contributions: S.B., C.W., P.F., and A.C. designed research; S.B. performed research; P.F. contributed new reagents/analytic tools; S.B. analyzed data; S.B., P.F., and A.C. wrote the paper; and C.W. and P.F. reviewed the manuscript.

The authors declare no competing interest.

This article is a PNAS Direct Submission.

[1]To whom correspondence may be addressed. Email: fratzl@mpikg.mpg.de or amaia.cipitria@mpikg.mpg.de.

This article contains supporting information online at http://www.pnas.org/lookup/suppl/doi:10.1073/pnas.2111046118/-/DCSupplemental.

Published December 23, 2021.

first-order far-from-equilibrium phase transitions (8, 13) or modeling cancer dormancy as a critical phenomenon using evolutionary game theory approaches (9).

Despite intrinsic differences across biological species, dormancy can be regarded as an evolutionarily conserved mechanism exploited by a multitude of organisms, such as insects, bacteria, worms, or plant seeds, which enables them to enter a growth-arrested state under hostile conditions (14–16). Such a mechanism must be reversible to ensure regrowth upon restoration of favorable settings. Notably, the physiological state of most mammalian adult stem cells is quiescent (or dormant) (17), reentering the cell cycle only when required. This low metabolic state prevents their exhaustion and lowers the probability of acquiring oncogenic mutations upon cell division (17).

A pathological example of dormancy, on the other hand, can be found during cancer metastasis, which involves the dissemination of detached cells from the primary tumor mass into distant organs. Here, disseminated cancer cells (DCCs) require growth-friendly conditions for metastatic progression; if the secondary organ does not foster metastatic growth, cancer cells can recapitulate the evolutionarily conserved mechanism of older organisms and switch into a dormant state (18, 19).

The consideration that almost half of all forms of cancer metastasis become clinically detectable years or even decades after primary tumor resection points toward the presence of an invisible latent stage of metastatic colonization (20). This challenges the hypothesis of an otherwise linear or exponential growth between primary tumor and metastatic site (21, 22). The question that arises then is: What is the cause for such nonlinearity in growth kinetics? A plausible answer would be that changes in the microenvironment at the dissemination site might provide the stimuli necessary for dormancy of DCCs, until either accumulation of genetic aberrations and/or microenvironment alterations trigger their awakening (20).

For a better description of the role of the microenvironment in modulating this process, we took advantage of the well-known concepts of stability and metastability for growing droplets of a thermodynamic phase. The idea is that a cancer cell aggregate (described as a droplet) grows by proliferation and migration of cancer cells within a normal tissue (the parent phase). When assuming that the cancer cell aggregate has a tendency to grow that is counterbalanced by an unfavorable interface between the droplet and the surrounding normal tissue, one obtains a formal analogy with thermodynamics of phase separation. The associated nucleation process can be 1) homogeneous, that is, occurring fully inside the parent phase (that is, the normal tissue) or 2) heterogeneous when the droplet grows in contact with a surface, so that the total interface between the nucleating droplet and the parent phase is reduced (see Fig. 2*A*). In this description, growth arrest (or dormancy) would correspond to a "metastable" state, which can be defined as a state of local (as opposed to global) minimum of energy, so that further growth requires to overcome a barrier. As a consequence, the system can reside in this local minimum, until enough energy is gained to leave this state and to progress toward a global minimum of energy (23). A crossing of the barrier may result from various perturbations, such as fluctuations in the driving force for growth or a decrease in the barrier height through a modification of the microenvironment. In this sense, metastability is the resilience of the system against small mechanobiological perturbations (24–28) that would ultimately lead to unrestricted growth (beyond the unstable state; see the sketch in Fig. 2*C*). In particular, we assume the growing tissue "droplet" to behave like a fluid, in that the relaxation of local stress concentrations is much faster than growth itself. Under these conditions, the Young–Laplace law leads to droplet shapes with constant curvature and kinetic metastability (see details in *SI Appendix*) that results from the fact that a small increase in droplet volume would lead to a negative change in growth rate (24, 29).

In this respect, some parallels can be drawn with critical states [also known as the emergence of multistability (8)], such as their reduced sensitivity to the details of the system, while acquiring increased susceptibility to environmental perturbations (8, 9, 11). Building on the fact that, at least for spherical shapes, tissue growth models fall under the same category as phase separation models of nodular structures (24, 29, 30) (e.g., growth of a particle within a solution, or diffusion along dislocation lines or grain boundaries), here we propose that cancer dormancy shares several traits of thermodynamic metastability. The duration (or stability) of this "dormant" state will then depend on the activation energy barrier, which, in thermodynamic terms, can be described as the amount of energy that needs to be overcome in order to transition from particle nucleation to its critical size and eventual growth.

We argue that the ability of cells and tissues to grow vs. remain dormant is highly sensitive to their interaction with the microenvironment, which introduces the emergence of one or more metastable states, assumed to be proxies of dormancy. Different modes of dormancy induction have been proposed, spanning from drug-induced survival of subpopulations of cells under chemotherapy treatment, paracrine signaling from vasculature and niche cells, biochemical factors (i.e., hypoxia or nutrients), and ECM-induced dormancy (31). Here we focus on more physical aspects of the microenvironment, and based on experimental data (Fig. 1) we simplistically classify three distinct classes of interactions: 1) cells adhering to a wetting flat surface in the form of a spherical cap, 2) a spherical droplet enclosed by an elastic sheath as a mechanical interpretation of ECM-mediated confinement, and 3) a spherical droplet with size-dependent limited growth due to lack of nutrients and oxygen, leading to cell apoptosis deep inside the tissue. We then put these results in the context of recent modeling, experimental, and clinical data from both physiological and pathological examples of cell and tissue growth. Notably, the concepts proposed here are not meant to replace cellular or genetic mechanisms but to provide a complementary physical description with a more global perspective for the role of the microenvironment in mediating the described processes. In other terms, thermodynamics dictates the possible, while mutations direct the probable (32).

Role of Adhesion

The majority of cells and tissues in the body are not just suspended in a void but require either cell–cell or cell–ECM anchorage in order to grow and proliferate. Meanwhile, adhesion has been shown to be directly involved in many steps of the metastatic cascade, including dissemination, homing, and dormancy. It has been previously reported that DCCs can adhere either close to the vasculature (i.e., perivascular niche) (34, 36) (Fig. 1, *1B* and *1D*) or in the proximity of bones (i.e., endosteal niche) (35) of the target organs (Fig. 1, *1C*). To better understand the role of adhesion in mediating dormancy and tissue growth, we start by observing the growth kinetics of an unconfined spherical droplet, well-known from classical nucleation theory (Fig. 2 *B* and *C*). This simple model shows that a size-dependent parameter, named the critical

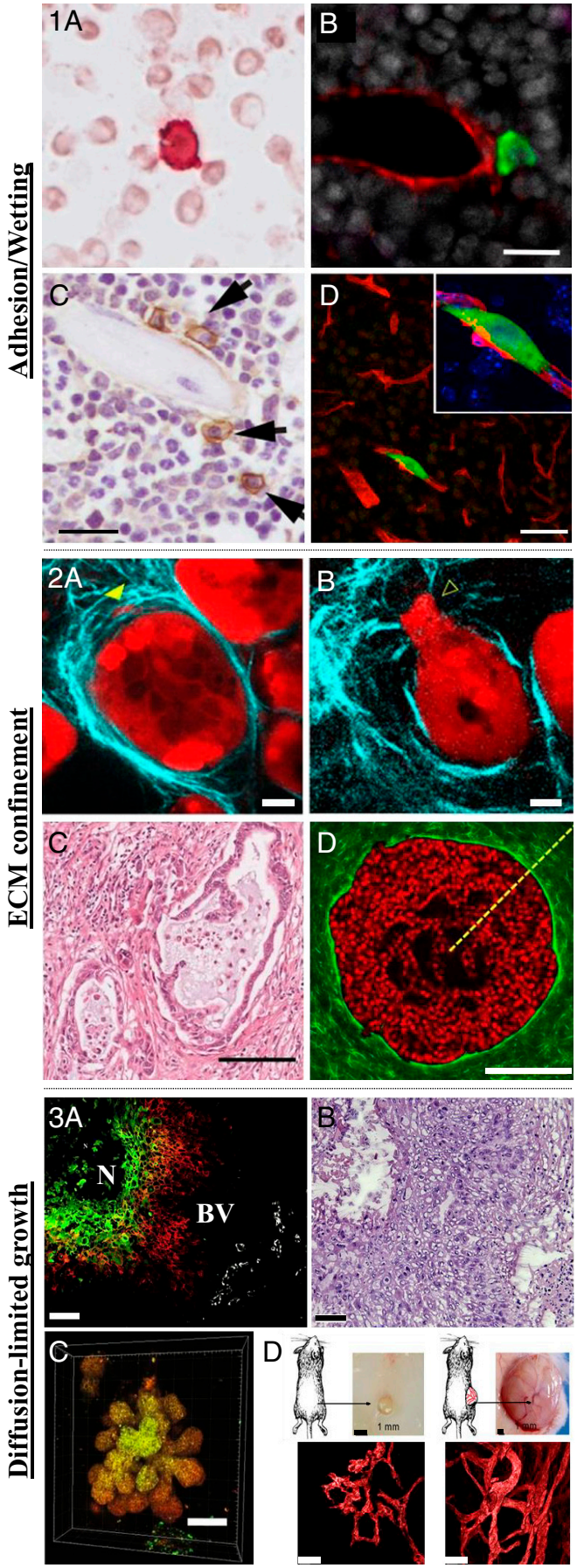

Fig. 1. Microenvironment-mediated cancer dormancy. (*1*) Adhesion/wetting. (*1A*) Disseminated breast cancer cell (red) in the proximity of neighboring cells in the bone marrow of patients with ductal carcinoma in situ (DCIS), the earliest and most noninvasive form of breast cancer (400-fold magnification). Adapted from ref. 33. (*1B*) Disseminated breast cancer cell (green) adhering to the microvasculature (red) of the bone marrow in a mouse model. (Scale bar, 20 μm.) Adapted from ref. 34. (*1C*) Disseminated MM cells (brown) adhere to the endosteal surface of trabecular bone in a mouse model. (Scale bar, 20 μm.) Adapted from ref. 35. (*1D*) Disseminated breast cancer cell (green) adhere to the microvasculature (red) of the brain in a mouse model. (Scale bar, 50 μm.) Adapted from ref. 36. (*2*) Mechanical confinement. (*2A and 2B*) Pancreatic ductal carcinoma (red) surrounded by collagen ECM (cyan) before (*2A*) and after (*2B*) invasion of the surrounding murine tissue. (Scale bar, 20 μm.) Adapted from ref. 37. (*2C*) Histopathological staining of collagen (pink) shows a dense sheath of collagen surrounding the tumor core in a patient diagnosed with pancreatic cancer. (Scale bar, 100 μm.) Adapted from ref. 38. (*2D*) Noninvasive mammary epithelial spheroid (red) embedded in a 3D collagen hydrogel. (Scale bar, 200 μm.) Adapted from ref. 39. (*3*) Diffusion of oxygen and nutrients. (*3A*) Fluorescent image of a human biopsy of squamous cell carcinoma of the larynx shows that the outer cells (red) which are close to the blood vessels (BV, white) to be less hypoxic than the cells at the core of the tumor (green cells) close to the black necrotic (N) region. (*3B*) Hematoxylin and eosin histological staining of the same region. (Scale bar, 50 μm.) Adapted from ref. 40. (*3C*) Fate mapping of hypoxic cells in 3D spheroid cultures reveal higher hypoxia levels at the core of the spheroids (yellow region) as opposed to the outer region (orange). (Scale bar, 100 μm.) Adapted from ref. 41. (*3D*) Human tumor cells injected subcutaneously in mice reveal slower tumor size with impaired and less developed vasculature for dormant, nonangiogenic tumors (*Left*) as opposed to fast-growing angiogenic tumors (*Right*). (Scale bar of vasculature images, 40 μm.) Adapted from ref. 42.

radius (R_c), exists, which, if exceeded, will result in the sustained growth of the droplet; otherwise, it will shrink and disappear (24) (Fig. 2*B*). More specifically, droplets with a volume smaller than V^* will shrink to zero while those larger than this size will see an unlimited growth. This means that in a classical nucleation process, as in the case of a tumor suspended in a void, there is no metastable droplet of finite size; instead, it either disappears or grows. This aspect is also visible in earlier theories of cancer growth (see figure 5 of ref. 43), where the tumor either grows or shrinks, depending on whether its size is above or below a critical dimension. Indeed, the critical size corresponds to a maximum of the energy curve (Fig. 2*B*) and, thus, to an unstable state (Fig. 2*C*). In Fig. 2, we restrict ourselves to a qualitative stability analysis, because the growth kinetics as well as actual values of the critical size will be different depending on the details of any specific tissue (type of cells, ECM composition, etc.).

We then model adhesion by including a wetting substrate to which the previously unsupported tissue nodule can now adhere (Fig. 2*A*). From a modeling point of view, this wetting surface provides a boundary condition, which limits the growth of an otherwise unconfined spherical droplet, also known as surface-directed phase separation (44–47). We and others have previously shown that this simple physical constraint can lead to the emergence of extremely complex structural shapes (24, 29, 48, 49).

Based on this, we hypothesize that the tissue adheres to a surface (that is "liked" by the tissue in the droplet) without costs in energy and in contrast to the interface with the foreign microenvironment. Fig. 2*A* shows two configurations for a droplet taking the shape of a spherical cap adhering to a circular patch of radius R_0 on the flat surface. Outside this patch, the adherence is not favorable (in physical terms, the droplet would not wet the foreign microenvironment outside the circular patch).

First, it is observed that with adhesion to a surface, a minimum value of the energy E/E^* appears at small volumes (red 40%, blue

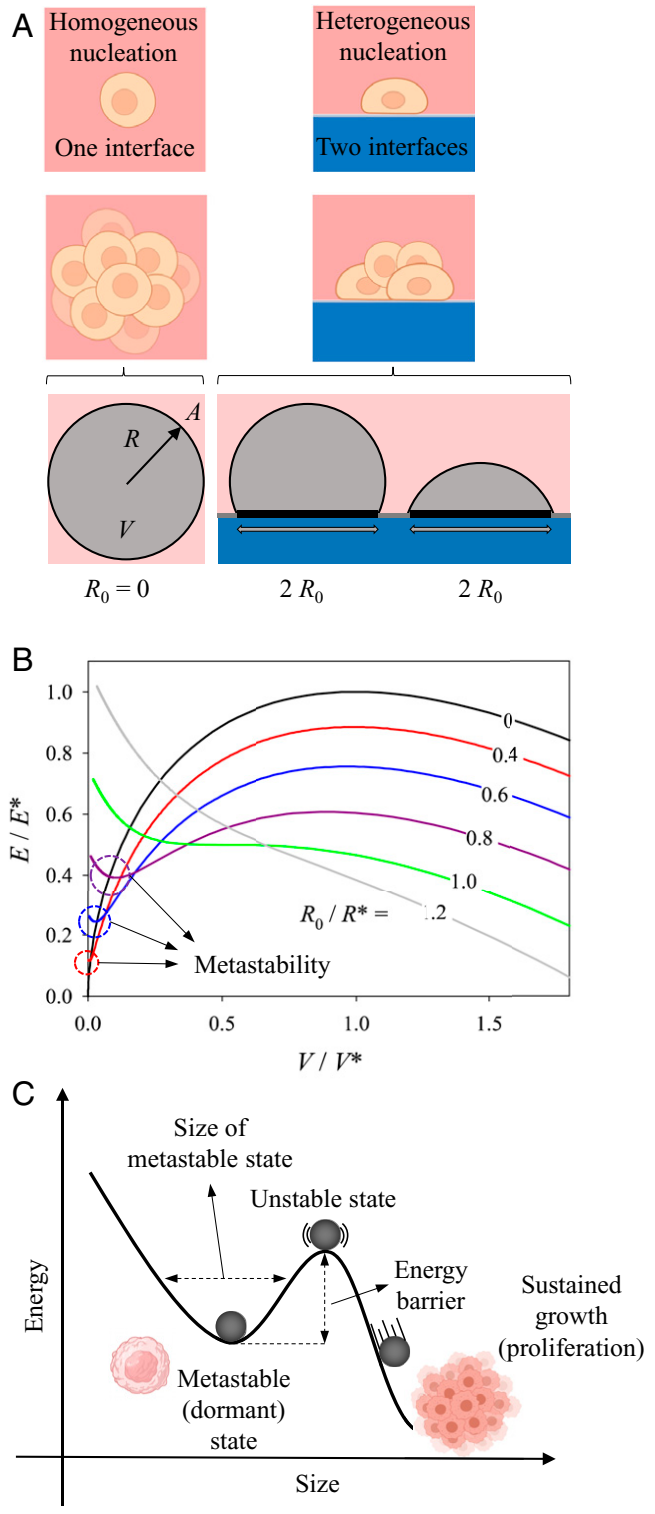

Fig. 2. Spherical droplet adhering to a flat wetting surface. (*A*) Graphical illustration of homogeneous and heterogeneous nucleation, where the former corresponds to a nonadhering spherical droplet (left circle) with radius R, surface area A, and volume V and the latter to a sphere adhering to a wetting surface on a circular patch of radius R_0. (*B*) Energy diagram as a function of volume changes when the droplet adheres to a wetting surface. The parameters E^*, V^*, and R^* are the energy, volume, and radius of a critical spherical droplet, respectively. The black line with $R_0/R^* = 0$ is the curve for a nonadherent spherical droplet, while the remaining curves show what happens when the same droplet adheres to a wetting surface on a contact circular patch with a radius 40 to 120% of the critical radius, R^*, as indicated. For detailed mathematical derivations, see equations in *SI Appendix*. (*C*) Example of an energy diagram illustrating a local energy minima or metastable state, an unstable state and sustained growth with the analogous proliferative state of cancer cells (illustrations created with BioRender.com).

60%, and purple 80%) (Fig. 2*B*). This minimum indicates the existence of a metastable droplet whose size is directly related to the radius of the adhesion patch, or, in other words, the amount of surface cells adhere to. In the context of cancer dormancy, it has been reported in multiple in vitro studies that adhesion of breast or prostate cancer cells to ECM-derived proteins such as fibronectin or collagen results in the up-regulation of transmembrane cell–ECM receptor integrins, which confer tumor cells with enhanced survival abilities in the form of a growth-arrested dormant phenotype (50–54). Likewise, it has been reported that at the site of primary breast tumors there is a great abundance of collagenous proteins, which bind to Discoidin Domain Receptors 1 and 2 (DDR1 and DDR2) transmembrane receptor kinases, which foster adhesion and endow tumor cells with stemness properties via STAT3 signaling (55, 56). Knocking out DDR1 in mouse models resulted in increased tumor malignancy and metastatic potential (57).

On the metastatic site, Montagner et al. (58) recently revealed that dormant disseminated breast cancer cells in the lung of mice secrete fibronectin fibrils, which leads to the activation of an integrin-mediated prosurvival mechanism. Seemingly, Carlson et al. (34) showed that disseminated tumor cells residing in the perivascular niche of the bone marrow are protected against chemotherapy by adhering to the vascular endothelium (Fig. 1, *1B*). Surprisingly, deleting the integrin-mediated adhesion between the tumor cells and their niche resulted in enhanced chemosensitization and prevention of bone metastasis, irrespective of cell cycle and proliferation state of the cells (34). Using intravital imaging, Lawson et al. (35) observed multiple myeloma (MM) cells switching to a dormant state after adhering to the endosteal surface of trabecular bones (Fig. 1, *1C*). Gene expression analysis revealed that cell adhesion molecules such as Vcam1 and Axl were highly up-regulated in dormant MMs, rendering them resistant to chemotherapy (35). Highlighting the importance of engaging with adhesion molecules, and not just their expression, recent work has shown that breast cancer cells that directly engage with specific "integrin subtype-specific peptidomimetics" immobilized on a surface via nanolithography display significant increase in survival upon exposure to chemotherapeutics (59).

Analogous behavior to dormant cancer cells was observed for adult quiescent hematopoietic stem cells, which, when presented with substrates coated with bone marrow-inspired ECM ligands or adherence junctions, showed reduced cycling and maintenance of long-term multipotency (60–62).

Nonetheless, an important observation from the growth kinetics of the adhering droplet is that, even though the size of the metastable state increases with adhesion, at the same time its stability, or, in other words, the activation barrier for growth (as measured by the energy difference between the minimum and the maximum of the curve), decreases (red 40%, blue 60%, purple 80%) (Fig. 2*B*). Concurrently, with increasing the size of the patch of radius R_0 the maximum value of the energy E/E^* decreases and, when the radius of the adhesion patch is equal to or exceeds the critical radius of a spherical droplet, there is no more stability (green 100% and grey 120% curves) (Fig. 2*B*). This indicates that, above a certain threshold, increasing adhesion will result in the

droplet leaving its dormant state, which is, apparently, in contrast to its previously described role in inducing and preserving dormancy (34, 50–57).

An example illustrating this controversy comes from a recent study featuring the effects of inflammation on dormant breast and prostate DCCs in the lungs of mice (63). Before inducing inflammation, DCCs resided in a dormant state with expressed but not engaged integrin receptors (low degree of adhesion). After tobacco smoke or bacterial lipopolysaccharide exposure, activated neutrophils were recruited to the lungs, where they formed neutrophil extracellular traps, which released ECM-degrading enzymes, resulting in the cleavage of ECM proteins, in particular laminin. These cleaved proteins then engaged with DCCs integrin receptors (high degree of adhesion), triggering their awakening and subsequent metastatic growth. Inhibiting this interaction by means of blocking antibodies prevented such outcome (63). Several other studies have similarly pointed to integrin or other adhesion molecules as essential mediators in the downstream signaling leading to the awakening of dormant DCCs (64–69).

Efforts in deciphering this seemingly paradoxical effect of adhesion have led to recognizing a graded rather than a binary role for adhesion on dormancy vs. proliferation of cancer cells (70–72). Within these lines, it had been previously reported that dormant DCCs express lower levels of integrin compared to their activated form (64, 73). Despite its simplicity, our model manages to capture this graded effect of adhesion: 1) Low adhesion (proportional to the size of the adhesion patch) leads to the emergence of a metastable (dormant) state, 2) increasing the adhesion patch lowers the energy required to exit this state, 3) until the size of the adhesion patch reaches the critical size of the droplet, resulting in the loss of metastability. Nevertheless, the concept of adhesion-mediated cancer dormancy is still in its infancy and far more experimental models are needed to validate the proposed thesis.

Importantly, the single size-dependent parameter, which controls both the size and the stability of the metastable droplet, is the radius of the adhesive patch, or in other words, the contact area to which cells/tissues adhere. The central role of a size-dependent parameter has been seemingly observed for tissues growing on substrates with different geometries (29). For a tissue growing on top of a hollow cylinder, for instance, a maximum height exists which the tissue will tend to reach, and above which tissue growth will stop. This resembles the case of fracture gaps present in osteotomy (74), where bone at each free end of the fracture grows to bridge the gap. Based on this model, it can be predicted that if the size of the segmental bone defect is bigger than a critical value, complete bone filling and healing will not take place (75).

Role of Mechanical Confinement

Growing tumors within different organs have been shown to be surrounded by a plethora of cells and ECM which restrict their growth in such confined microenvironment, while being subjected to mechanical compression (76, 77). Premalignant and less-invasive tumors in both humans and mouse models have been widely reported of being surrounded by dense ECM fibers (37, 38) (Fig. 1 *2A–2D*). Seemingly, single cancer cells have been observed to reside within the dense collagen stroma enclosing breast tumors (78). Here we seek to understand how mechanical confinement provided by an elastic sheath, meant to resemble a fibrous capsule with predominantly elastic

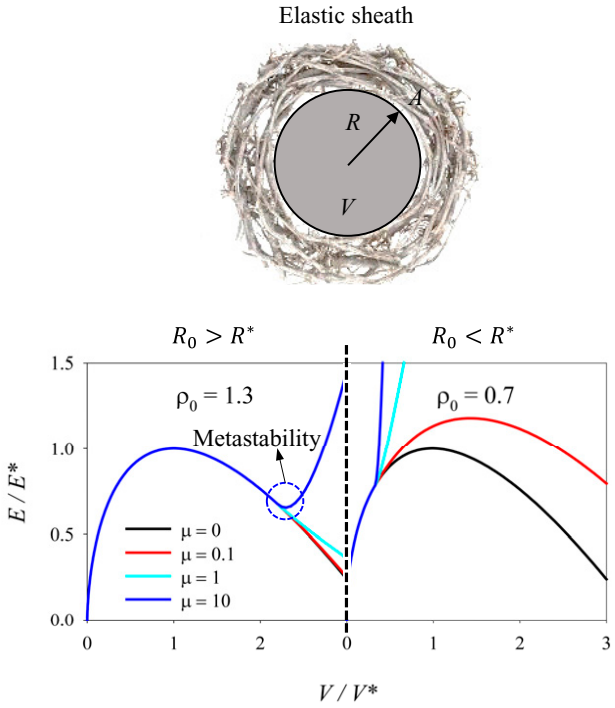

Fig. 3. Spherical droplet mechanically confined by an elastic sheath. Graphical illustration and energy diagram of a spherical droplet mechanically confined by an elastic sheath meant to resemble an ECM with predominantly elastic properties, as a function of volume changes. ρ_0 shows the relation between the unstretched radius of the sheath (R_0) and the critical radius of the droplet (R^*). μ characterizes the stiffness of the elastic sheath in relation to the critical energy of the droplet (E^*) and ρ_0. For detailed mathematical derivations, see equations in *SI Appendix*.

properties, restrains the growth of a spherical droplet starting from a volume V_0 (corresponding to a sphere of radius R_0) (Fig. 3).

Given that the elastic energy of the sheath increases with the volume of the droplet, if $\rho_0 = {}^{R_0}/_{R^*}$ is lower than 1 ($\rho_0 < 1$), or in other words if the initial radius of the sphere is lower than its critical radius, there is no minimum in the total energy. Instead, for $\rho_0 > 1$ and for a sufficiently stiff sheath (μ), a minimum of the energy appears for a size larger than ρ_0 (how much larger will depend on the stiffness of the elastic sheath). There are, however, important differences from the previous case, where the droplet growth was controlled only by adhesion to a substrate: 1) Now the metastable state (corresponding to the minimum of the energy) is at a relatively large size of the droplet (necessarily larger than its critical size R^*, given that the metastable state emerges at $V/V^* > 2$), 2) the energy barrier (the difference between the maximum and the minimum energy) to exit the dormant state toward further growth is predicted to be very large or even infinite. In this sense, such a state would represent a stable state and not a metastable one, unless the elastic sheath is damaged or degraded in some way. A change from elastic to viscous properties of the ECM or proteolytic degradation could reflect such variations (55).

Indeed, in benign tumors or early-stage carcinoma in situ, growth is contained by a basement membrane which needs to be breached either by proteolytic degradation through matrix metalloproteinases secreted by tumor and stromal cells or through force-mediated remodeling and rupture for successful tissue invasion and tumor progression (55, 79). Intuitively, recent in vitro

experiments have shown that highly proliferative cancer cells encapsulated in nondegradable stiff synthetic hydrogels display several phenotypic features of dormant cancer cells (80). This resemblance is reduced if cells were allowed to grow in degradable hydrogels (80). In a less-intuitive in vitro study, it was observed that even within nondegradable hydrogels with matching elastic moduli, breast cancer cell cycle progression can be modulated as a function of the stress relaxation (viscosity) properties of the surrounding material (81). Specifically, encapsulation within hydrogels with slow stress relaxation led to a higher number of growth-arrested cells compared to the faster stress-relaxing hydrogels (81). As for the case of adhesion, mechanical confinement has been shown to play a role in stem cell maintenance as well. Hematopoietic stem and progenitor cells within spatially constrained microcavities or embedded in hydrogels of a higher degree of cross-linking maintained a quiescent and undifferentiated state as opposed to less-confining microenvironments (82, 83).

Theoretical models of tumor growth within a surrounding tissue have similarly highlighted the importance of the ECM's physical properties in driving tumor progression. Basan et al. (43), for instance, have shown that if the surface tension of the ECM basement membrane surrounding the tumor increases faster than the radius of the tumor, cancer expansion will eventually stop, resembling a dormant state. Building on the previously described (84) vertex model of solid–liquid transition of a two-dimensional (2D) confluent monolayer, Merkel and Manning (85) generalized a three-dimensional (3D) tissue-based vertex model introducing the ECM as a spring network with interfacial line tension (γ) surrounding a tissue. Interestingly, above a certain critical tension ($\gamma > \gamma_c$), a cavitational instability occurs, resulting in a compression-induced fluidization of the tissue. Below this critical tension ($\gamma < \gamma_c$), tissue boundaries become unstable due to cavities and empty spaces hindering cell–ECM coupling (86). In the compact regime, the tissue is not affected by the network tension and its state is a function of cell shape as defined by 2D vertex models (84). On the other hand, when γ is low, the tissue becomes sensitive to the network and its phase will depend on both shape and cell–cell alignment (86). Based on these results, the authors postulated that prior to invasion cell alignment might lead to tumor solidification, which, upon breaching through the basement membrane, will switch to a fluid behavior (relative to the external ECM), leading to tumor migration (86). Importantly, this and previous work suggests that in solid-to-liquid transitions the origin of rigidity remains purely geometric and therefore robust among different biological systems for both 2D and 3D configurations (84, 85).

These examples underline the importance of the ECM's confining role, which, when coupled with specific mechanical properties, could grant (or prevent) tumor growth and progression by means of protease-dependent and/or independent mechanisms.

Role of Diffusion of Oxygen and Nutrients

The high proliferation rate of tumor cells requires extensive nutrient and oxygen supply. Nonetheless, this is impaired by the highly dense tumor mass, whose growth is mediated by a turnover/balance between apoptotic and proliferating cells (87), until hypoxia-mediated signaling triggers ECM remodeling and subsequent vascularization promoting tumor progression (40–42, 88) (Fig. 1, *3A–3D*). Several studies have associated tumor dormancy with impaired vasculature in both primary and secondary sites (42, 89), which can be interrupted by angiogenic bursts within the tumor microenvironment (90).

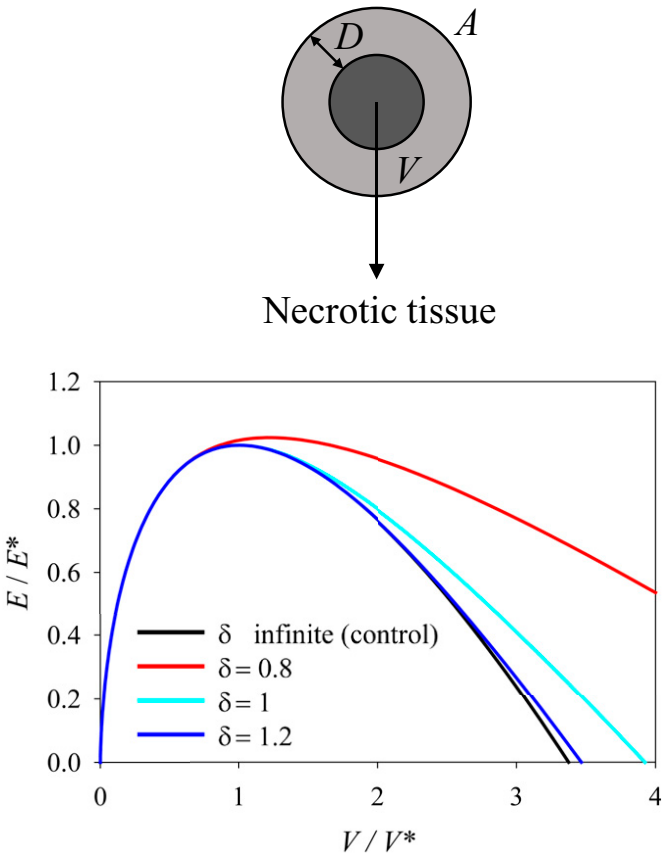

Fig. 4. Spherical droplet with size-dependent growth. Graphical illustration and energy diagram of a spherical droplet with size-dependent growth as a function of volume changes. The assumed tissue cannot survive below a distance *D* from the surface due to necrosis associated with limited diffusion of oxygen and nutrients. δ is the ratio of the thickness of the viable part (*D*) and the critical radius of the droplet (R^*). For detailed mathematical derivations, see equations in *SI Appendix*.

To model such behavior with a very simplistic approach, here we consider a tissue that cannot survive below a distance D from the surface, as it gets necrotic due to limited diffusion of oxygen and nutrients Fig. 4. Hence, the volume is reduced to the outer shell with thickness D, as soon as the radius of the droplet $R > D$.

When looking in more detail at this model, it appears that this function has no minimum outside $\rho = 0$ for any value of D, meaning that no metastable state is predicted which could be interpreted in terms of dormancy. In line with our physical framework, and in accordance with clinical data, Monte Carlo simulations have predicted that cancer dormancy as a function of balanced apoptosis/proliferation alone has low survival probabilities, suggesting that accounting for an alternative growth-arrested or dormant state is indispensable to explain the strikingly high recurrence of late-stage metastatic relapse (91).

Discussion and Concluding Remarks

The nonlinear progression of tumor growth at the primary compared to the secondary site has led cancer biologists and clinicians to emphasize more than ever the role of the tumor microenvironment in modulating the growth of DCCs in this invisible phase of metastasis (20). Inspired by nucleation theory and concepts from thermodynamic phase separation, here we propose that the

emergence of metastable states in the growth kinetics of surface-directed or enclosed droplets can be assumed as proxies of cancer dormancy. Importantly, and in line with experimental and clinical data, we show that the only scenarios where a metastable state is predicted is when physical aspects of the microenvironment are included in the model: adhesion and mechanical-mediated confinement. It is worth noting that the concepts of phase separation and nucleation are not new to biology: At the subcellular level, a fast-growing body of evidence is pointing toward liquid–liquid phase separation underlying the organization of membrane-free biomolecular condensates (92), known to participate in a wide variety of intracellular processes such as DNA damage response (93), protein translocation (94, 95), and signal transduction (96). Importantly, nucleation was shown to govern growth initiation and size control of these condensates (97). These, in turn, interact with existing substrates which energetically favor their coacervation (agglomeration), as shown for chromatin during spindle formation (98), ribosomal RNA for the nucleolus (99), or centrioles for centrosomes (100, 101).

To achieve an optimal level of functionality, biological systems require adaptability and robustness during growth and development or upon environmental perturbations. Being near critical and metastable states during phase transitions allows the system to reach a balance between stability from the ordered and versatility from the disordered state, respectively (10, 102). Slow-driven processes in particular, such as evolution (103), morphogenesis (11), or dormancy (9), have proven to fit analogies of criticality, metastability, and phase transition processes. Their long time scales and environmental interaction-dominated nature leads to large fluctuations at transition points, which results in high energy gains upon even small perturbations (11, 104). Studies on brain neural networks have shown that the number of metastable states is highest at the critical point, where the role of the ordered state is to optimize information storage, while the disordered state maximizes transmission efficiency (105). Extensive empirical evidence from gene expression patterns (106), morphogenesis (11), cell growth (107), and dormancy (9), alongside recent computational and analytical models from information theory (102), substantiate this hypothesis (108).

With this in mind, here we propose that cancer dormancy can be regarded as an example where an equilibrium between stability and adaptability is achieved: DCCs reside in a growth-arrested state (e.g., mediated by adhesion or confinement), acquiring several survival traits against an otherwise hostile environment (robust ordered state). Concurrently, this metabolically less-committing noncycling state allows DCCs to activate specific molecular pathways which act by influencing their sensitivity to changes in the microenvironment, or by actively fostering growth-favoring/suppressing conditions (adaptability state) (109). In this article, we have not considered adaptability, as the aim was to advance the idea of viewing dormancy from a metastability theory perspective. Future work could address this point by introducing a chemical potential, where spheroid growth rate is not constant but rather a variable which depends on the presence/absence of growth factors (29), or alterations of surface tension due to changes in cytoskeletal contractility of the cells within the tissue (110, 111).

Notably, the physical framework of microenvironment-mediated dormancy proposed in this article does not oppose or replace genetic/molecular signaling or other subcellular mechanisms involved in the process. Instead, it proposes a multiscale hand-to-hand relationship, where the microenvironment feeds information to cells/tissues, and vice versa.

Data Availability. The data presented here have been deposited in Edmond, Open Access Data Repository of the Max Planck Society (https://dx.doi.org/10.17617/3.8j), or provided in the *SI Appendix* and within this paper.

Acknowledgments

S.B. and A.C. acknowledge funding by the Deutsche Forschungsgemeinschaft Emmy Noether grant CI 203/2-1.

1 M. J. Bissell, H. G. Hall, G. Parry, How does the extracellular matrix direct gene expression? *J. Theor. Biol.* **99**, 31–68 (1982).
2 K. H. Vining, D. J. Mooney, Mechanical forces direct stem cell behaviour in development and regeneration. *Nat. Rev. Mol. Cell Biol.* **18**, 728–742 (2017).
3 K. Goodwin, C. M. Nelson, Mechanics of development. *Dev. Cell* **56**, 240–250 (2020).
4 T. Mammoto, D. E. Ingber, Mechanical control of tissue and organ development. *Development* **137**, 1407–1420 (2010).
5 H. T. Nia, L. L. Munn, R. K. Jain, Physical traits of cancer. *Science* **370**, eaaz0868 (2020).
6 C. D. Paul *et al.*, Tissue architectural cues drive organ targeting of tumor cells in zebrafish. *Cell Syst.* **9**, 187–206.e16 (2019).
7 H. Haken, *Synergetics* (Springer, Berlin, 1978).
8 P. C. W. Davies, L. Demetrius, J. A. Tuszynski, Cancer as a dynamical phase transition. *Theor. Biol. Med. Model.* **8**, 30 (2011).
9 A. Wu *et al.*, Cancer dormancy and criticality from a game theory perspective. *Cancer Converg.* **2**, 1 (2018).
10 N. I. Petridou, C. P. Heisenberg, Tissue rheology in embryonic organization. *EMBO J.* **38**, e102497 (2019).
11 D. Krotov, J. O. Dubuis, T. Gregor, W. Bialek, Morphogenesis at criticality. *Proc. Natl. Acad. Sci. U.S.A.* **111**, 3683–3688 (2014).
12 J. Ranft *et al.*, Fluidization of tissues by cell division and apoptosis. *Proc. Natl. Acad. Sci. U.S.A.* **107**, 20863–20868 (2010).
13 W. Kang *et al.*, A novel jamming phase diagram links tumor invasion to non-equilibrium phase separation. *iScience* **24**, 103252 (2021).
14 S. E. Jones, J. T. Lennon, Dormancy contributes to the maintenance of microbial diversity. *Proc. Natl. Acad. Sci. U.S.A.* **107**, 5881–5886 (2010).
15 M. Koornneef, L. Bentsink, H. Hilhorst, Seed dormancy and germination. *Curr. Opin. Plant Biol.* **5**, 33–36 (2002).
16 J. Wang, S. K. Kim, Global analysis of dauer gene expression in Caenorhabditis elegans. *Development* **130**, 1621–1634 (2003).
17 L. Li, H. Clevers, Coexistence of quiescent and active. *Science* **327**, 542–545 (2010).
18 J. A. Aguirre-Ghiso, Models, mechanisms and clinical evidence for cancer dormancy. *Nat. Rev. Cancer* **7**, 834–846 (2007).
19 K. J. Pienta, E. U. Hammarlund, J. S. Brown, S. R. Amend, R. M. Axelrod, Cancer recurrence and lethality are enabled by enhanced survival and reversible cell cycle arrest of polyaneuploid cells. *Proc. Natl. Acad. Sci. U.S.A.* **118**, e2020838118 (2021).
20 C. A. Klein, Cancer progression and the invisible phase of metastatic colonization. *Nat. Rev. Cancer* **20**, 681–694 (2020).
21 J. W. Uhr, K. Pantel, Controversies in clinical cancer dormancy. *Proc. Natl. Acad. Sci. U.S.A.* **108**, 12396–12400 (2011).
22 C. A. Klein, Framework models of tumor dormancy from patient-derived observations. *Curr. Opin. Genet. Dev.* **21**, 42–49 (2011).
23 S. E. Machlin, *An Introduction to Aspects of Thermodynamics and Kinetics Relevant to Materials Science* (Elsevier, 2007).
24 J. W. C. Dunlop, G. A. Zickler, R. Weinkamer, F. D. Fischer, P. Fratzl, The emergence of complexity from a simple model for tissue growth. *J. Stat. Phys.* **180**, 459–473 (2020).
25 C. J. Cyron, J. D. Humphrey, Vascular homeostasis and the concept of mechanobiological stability. *Int. J. Eng. Sci.* **85**, 203–223 (2014).
26 C. J. Cyron, R. C. Aydin, Mechanobiological free energy: A variational approach to tensional homeostasis in tissue equivalents. *ZAMM* **97**, 1011–1019 (2017).

27 C. J. Cyron, J. D. Humphrey, Growth and remodeling of load-bearing biological soft tissues. *Meccanica* **52**, 645–664 (2017).
28 C. J. Cyron, J. S. Wilson, J. D. Humphrey, Mechanobiological stability: A new paradigm to understand the enlargement of aneurysms? *J. R. Soc. Interface* **11**, 20140680 (2014).
29 F. D. Fischer, G. A. Zickler, J. W. C. Dunlop, P. Fratzl, Tissue growth controlled by geometric boundary conditions: A simple model recapitulating aspects of callus formation and bone healing. *J. R. Soc. Interface* **12**, 20150108 (2015).
30 R. D. Vengrenovitch, On the Ostwald ripening theory. *Acta Metall.* **30**, 1079–1086 (1982).
31 S. Pradhan, J. L. Sperduto, C. J. Farino, J. H. Slater, Engineered *in vitro* models of tumor dormancy and reactivation. *J. Biol. Eng.* **12**, 37 (2018).
32 Y. Wang, R. Crea, Eds., *Tumor Dormancy and Recurrence* (Springer International Publishing, 2017).
33 N. Sänger *et al.*, Disseminated tumor cells in the bone marrow of patients with ductal carcinoma in situ. *Int. J. Cancer* **129**, 2522–2526 (2011).
34 P. Carlson *et al.*, Targeting the perivascular niche sensitizes disseminated tumour cells to chemotherapy. *Nat. Cell Biol.* **21**, 238–250 (2019).
35 M. A. Lawson *et al.*, Osteoclasts control reactivation of dormant myeloma cells by remodelling the endosteal niche. *Nat. Commun.* **6**, 8983 (2015).
36 S. Malladi *et al.*, Metastatic latency and immune evasion through autocrine inhibition of WNT. *Cell* **165**, 45–60 (2016).
37 A. Ray *et al.*, Stromal architecture directs early dissemination in pancreatic ductal adenocarcinoma. bioRxiv [Preprint] (2021). https://www.biorxiv.org/content/10.1101/2021.02.19.431984v1 (Accessed 1 March 2021).
38 A. Keikhosravi *et al.*, Non-disruptive collagen characterization in clinical histopathology using cross-modality image synthesis. *Commun. Biol.* **3**, 414 (2020).
39 J. Ferruzzi *et al.*, Compressive remodeling alters fluid transport properties of collagen networks – Implications for tumor growth. *Sci. Rep.* **9**, 17151 (2019).
40 I. J. Hoogsteen *et al.*, Hypoxia in larynx carcinomas assessed by pimonidazole binding and the value of CA-IX and vascularity as surrogate markers of hypoxia. *Eur. J. Cancer* **45**, 2906–2914 (2009).
41 I. Godet *et al.*, Fate-mapping post-hypoxic tumor cells reveals a ROS-resistant phenotype that promotes metastasis. *Nat. Commun.* **10**, 4862 (2019).
42 N. Almog, Molecular mechanisms underlying tumor dormancy. *Cancer Lett.* **294**, 139–146 (2010).
43 M. Basan, T. Risler, J. F. Joanny, X. Sastre-Garau, J. Prost, Homeostatic competition drives tumor growth and metastasis nucleation. *HFSP J.* **3**, 265–272 (2009).
44 S. Bastea, S. Puri, J. L. Lebowitz, Surface-directed spinodal decomposition in binary fluid mixtures. *Phys. Rev. E Stat. Nonlin. Soft Matter Phys.* **63**, 041513 (2001).
45 K. Binder, S. Puri, S. K. Das, J. Horbach, Phase separation in confined geometries. *J. Stat. Phys.* **138**, 51–84 (2010).
46 S. Puri, Surface-directed spinodal decomposition. *J. Phys. Condens. Matter* **17**, R101–R142 (2005).
47 S. Puri, K. Binder, Surface-directed phase separation with off-critical composition: Analytical and numerical results. *Phys. Rev. E Stat. Nonlin. Soft Matter Phys.* **66**, 061602 (2002).
48 P. Lenz, W. Fenzl, R. Lipowsky, Wetting of ring-shaped surface domains. *Europhys. Lett.* **53**, 618–624 (2001).
49 H. Gau, Liquid morphologies on structured surfaces: From microchannels to microchips. *Science* **283**, 46–49 (1999).
50 M. Ojalill *et al.*, Integrin α2β1 decelerates proliferation, but promotes survival and invasion of prostate cancer cells. *Oncotarget* **9**, 32435–32447 (2018).
51 J. Barrios, R. Wieder, Dual FGF-2 and intergrin α5β1 signaling mediate GRAF-induced RhoA inactivation in a model of breast cancer dormancy. *Cancer Microenviron.* **2**, 33–47 (2009).
52 R. Korah, M. Boots, R. Wieder, Integrin α5β1 promotes survival of growth-arrested breast cancer cells: An in vitro paradigm for breast cancer dormancy in bone marrow. *Cancer Res.* **64**, 4514–4522 (2004).
53 L. E. Barney *et al.*, Tumor cell-organized fibronectin maintenance of a dormant breast cancer population. *Sci. Adv.* **6**, eaaz4157 (2020).
54 P. Henriet, Z.-D. Zhong, P. C. Brooks, K. I. Weinberg, Y. A. DeClerck, Contact with fibrillar collagen inhibits melanoma cell proliferation by up-regulating p27KIP1. *Proc. Natl. Acad. Sci. U.S.A.* **97**, 10026–10031 (2000).
55 J. Winkler, A. Abisoye-Ogunniyan, K. J. Metcalf, Z. Werb, Concepts of extracellular matrix remodelling in tumour progression and metastasis. *Nat. Commun.* **11**, 5120 (2020).
56 H. Gao *et al.*, Multi-organ site metastatic reactivation mediated by non-canonical discoidin domain receptor 1 signaling. *Cell* **166**, 47–62 (2016).
57 K. Takai *et al.*, Discoidin domain receptor 1 (DDR1) ablation promotes tissue fibrosis and hypoxia to induce aggressive basal-like breast cancers. *Genes Dev.* **32**, 244–257 (2018).
58 M. Montagner *et al.*, Crosstalk with lung epithelial cells regulates Sfrp2-mediated latency in breast cancer dissemination. *Nat. Cell Biol.* **22**, 289–296 (2020).
59 J. L. Young *et al.*, Integrin subtypes and nanoscale ligand presentation influence drug sensitivity in cancer cells. *Nano Lett.* **20**, 1183–1191 (2020).
60 M. Kräter *et al.*, Bone marrow niche-mimetics modulate HSPC function via integrin signaling. *Sci. Rep.* **7**, 2549 (2017).
61 A. Roch *et al.*, Single-cell analyses identify bioengineered niches for enhanced maintenance of hematopoietic stem cells. *Nat. Commun.* **8**, 221 (2017).
62 J. S. Choi, B. A. C. Harley, Marrow-inspired matrix cues rapidly affect early fate decisions of hematopoietic stem and progenitor cells. *Sci. Adv.* **3**, e1600455 (2017).
63 J. Albrengues, *et al.*, Neutrophil extracellular traps produced during inflammation awaken dormant cancer cells in mice. *Science* **361**, eaao4227 (2018).
64 D. Barkan *et al.*, Inhibition of metastatic outgrowth from single dormant tumor cells by targeting the cytoskeleton. *Cancer Res.* **68**, 6241–6250 (2008).
65 D. Barkan *et al.*, Metastatic growth from dormant cells induced by a col-I-enriched fibrotic environment. *Cancer Res.* **70**, 5706–5716 (2010).
66 J. A. Aguirre Ghiso, Inhibition of FAK signaling activated by urokinase receptor induces dormancy in human carcinoma cells in vivo. *Oncogene* **21**, 2513–2524 (2002).
67 T. Shibue, M. W. Brooks, R. A. Weinberg, An integrin-linked machinery of cytoskeletal regulation that enables experimental tumor initiation and metastatic colonization. *Cancer Cell* **24**, 481–498 (2013).
68 T. Shibue, R. A. Weinberg, Integrin beta1-focal adhesion kinase signaling directs the proliferation of metastatic cancer cells disseminated in the lungs. *Proc. Natl. Acad. Sci. U.S.A.* **106**, 10290–10295 (2009).
69 E. E. Er *et al.*, Pericyte-like spreading by disseminated cancer cells activates YAP and MRTF for metastatic colonization. *Nat. Cell Biol.* **20**, 966–978 (2018).
70 S.-Y. Park, J.-S. Nam, The force awakens: Metastatic dormant cancer cells. *Exp. Mol. Med.* **52**, 569–581 (2020).
71 D. Barkan, J. E. Green, A. F. Chambers, Extracellular matrix: A gatekeeper in the transition from dormancy to metastatic growth. *Eur. J. Cancer* **46**, 1181–1188 (2010).
72 D. E. White, J. H. Rayment, W. J. Muller, Addressing the role of cell adhesion in tumor cell dormancy. *Cell Cycle* **5**, 1756–1759 (2006).
73 J. A. Aguirre-Ghiso, Y. Estrada, D. Liu, L. Ossowski, ERK(MAPK) activity as a determinant of tumor growth and dormancy; regulation by p38(SAPK). *Cancer Res.* **63**, 1684–1695 (2003).
74 D. R. Epari, H. Schell, H. J. Bail, G. N. Duda, Instability prolongs the chondral phase during bone healing in sheep. *Bone* **38**, 864–870 (2006).
75 J. C. Reichert *et al.*, The challenge of establishing preclinical models for segmental bone defect research. *Biomaterials* **30**, 2149–2163 (2009).
76 G. Helmlinger, P. A. Netti, H. C. Lichtenbeld, R. J. Melder, R. K. Jain, Solid stress inhibits the growth of multicellular tumor spheroids. *Nat. Biotechnol.* **15**, 778–783 (1997).
77 H. T. Nia, *et al.*, Solid stress and elastic energy as measures of tumour mechanopathology. *Nat. Biomed. Eng.* **1**, 0004 (2017).
78 V. Raviraj *et al.*, Dormant but migratory tumour cells in desmoplastic stroma of invasive ductal carcinomas. *Clin. Exp. Metastasis* **29**, 273–292 (2012).
79 O. W. Petersen, L. Rønnov-Jessen, A. R. Howlett, M. J. Bissell, Interaction with basement membrane serves to rapidly distinguish growth and differentiation pattern of normal and malignant human breast epithelial cells. *Proc. Natl. Acad. Sci. U.S.A.* **89**, 9064–9068 (1992).
80 S. Pradhan, J. H. Slater, Tunable hydrogels for controlling phenotypic cancer cell states to model breast cancer dormancy and reactivation. *Biomaterials* **215**, 119177 (2019).
81 S. Nam *et al.*, Cell cycle progression in confining microenvironments is regulated by a growth-responsive TRPV4-PI3K/Akt-p27^{Kip1} signaling axis. *Sci. Adv.* **5**, eaaw6171 (2019).

82 E. Müller *et al.*, Distinguishing autocrine and paracrine signals in hematopoietic stem cell culture using a biofunctional microcavity platform. *Sci. Rep.* **6**, 31951 (2016).
83 D. Gvaramia *et al.*, Combined influence of biophysical and biochemical cues on maintenance and proliferation of hematopoietic stem cells. *Biomaterials* **138**, 108–117 (2017).
84 D. Bi, J. H. Lopez, J. M. Schwarz, M. L. Manning, A density-independent rigidity transition in biological tissues. *Nat. Phys.* **11**, 1074–1079 (2015).
85 M. Merkel, M. L. Manning, A geometrically controlled rigidity transition in a model for confluent 3D tissues. *New J. Phys.* **20**, 022002 (2018).
86 A. Parker, M. C. Marchetti, M. L. Manning, J. M. Schwarz, How does the extracellular matrix affect the rigidity of an embedded spheroid? arXiv [Preprint] (2020). https://arxiv.org/abs/2006.16203 (Accessed 1 March 2021).
87 L. Holmgren, M. S. O'Reilly, J. Folkman, Dormancy of micrometastases: Balanced proliferation and apoptosis in the presence of angiogenesis suppression. *Nat. Med.* **1**, 149–153 (1995).
88 D. Hanahan, R. A. Weinberg, The hallmarks of cancer. *Cell* **100**, 57–70 (2000).
89 M. S. O'Reilly, L. Holmgren, C. Chen, J. Folkman, Angiostatin induces and sustains dormancy of human primary tumors in mice. *Nat. Med.* **2**, 689–692 (1996).
90 S. Indraccolo *et al.*, Interruption of tumor dormancy by a transient angiogenic burst within the tumor microenvironment. *Proc. Natl. Acad. Sci. U.S.A.* **103**, 4216–4221 (2006).
91 D. P. Taylor, J. Z. Wells, A. Savol, C. Chennubhotla, A. Wells, Modeling boundary conditions for balanced proliferation in metastatic latency. *Clin. Cancer Res.* **19**, 1063–1070 (2013).
92 S. F. Banani, H. O. Lee, A. A. Hyman, M. K. Rosen, Biomolecular condensates: Organizers of cellular biochemistry. *Nat. Rev. Mol. Cell Biol.* **18**, 285–298 (2017).
93 A. Patel *et al.*, A liquid-to-solid phase transition of the ALS protein FUS accelerated by disease mutation. *Cell* **162**, 1066–1077 (2015).
94 Y. Lu *et al.*, Phase separation of TAZ compartmentalizes the transcription machinery to promote gene expression. *Nat. Cell Biol.* **22**, 453–464 (2020).
95 D. Cai *et al.*, Phase separation of YAP reorganizes genome topology for long-term YAP target gene expression. *Nat. Cell Biol.* **21**, 1578–1589 (2019).
96 X. Su, *et al.*, Phase separation of signaling molecules promotes T cell receptor signal transduction. *Science* **352**, 595–599 (2016).
97 A. A. Hyman, C. A. Weber, F. Jülicher, Liquid-liquid phase separation in biology. *Annu. Rev. Cell Dev. Biol.* **30**, 39–58 (2014).
98 R. Heald *et al.*, Self-organization of microtubules into bipolar spindles around artificial chromosomes in Xenopus egg extracts. *Nature* **382**, 420–425 (1996).
99 A. Grob, C. Colleran, B. McStay, Construction of synthetic nucleoli in human cells reveals how a major functional nuclear domain is formed and propagated through cell division. *Genes Dev.* **28**, 220–230 (2014).
100 P. Gönczy, Towards a molecular architecture of centriole assembly. *Nat. Rev. Mol. Cell Biol.* **13**, 425–435 (2012).
101 D. Zwicker, M. Decker, S. Jaensch, A. A. Hyman, F. Jülicher, Centrosomes are autocatalytic droplets of pericentriolar material organized by centrioles. *Proc. Natl. Acad. Sci. U.S.A.* **111**, E2636–E2645 (2014).
102 J. Hidalgo *et al.*, Information-based fitness and the emergence of criticality in living systems. *Proc. Natl. Acad. Sci. U.S.A.* **111**, 10095–10100 (2014).
103 D. M. Raup, The role of extinction in evolution. *Proc. Natl. Acad. Sci. U.S.A.* **91**, 6758–6763 (1994).
104 S. Complexity *et al.*, *Critical Phenomena in Natural Sciences* (Springer-Verlag, 2006).
105 C. Haldeman, J. M. Beggs, Critical branching captures activity in living neural networks and maximizes the number of metastable States. *Phys. Rev. Lett.* **94**, 058101 (2005).
106 M. Nykter *et al.*, Gene expression dynamics in the macrophage exhibit criticality. *Proc. Natl. Acad. Sci. U.S.A.* **105**, 1897–1900 (2008).
107 C. Furusawa, K. Kaneko, Adaptation to optimal cell growth through self-organized criticality. *Phys. Rev. Lett.* **108**, 208103 (2012).
108 T. Mora, W. Bialek, Are biological systems poised at criticality? *J. Stat. Phys.* **144**, 268–302 (2011).
109 M. Werner-Klein *et al.*, Interleukin-6 trans-signaling is a candidate mechanism to drive progression of human DCCs during clinical latency. *Nat. Commun.* **11**, 4977 (2020).
110 S. Ehrig *et al.*, Surface tension determines tissue shape and growth kinetics. *Sci. Adv.* **5**, eaav9394 (2019).
111 P. Kollmannsberger, C. M. Bidan, J. W. C. Dunlop, P. Fratzl, V. Vogel, Tensile forces drive a reversible fibroblast-to-myofibroblast transition during tissue growth in engineered clefts. *Sci. Adv.* **4**, eaao4881 (2018).

Appendix

Mathematical derivations

Description of the kinetic stability criterion

The kinetic stability criterion can be described using the following growth equation:

$$\dot{V}/_{V} = 3f\gamma(K - K^*)$$

where V is the nodule's volume and $\dot{V}$ its time derivative, f is a kinetic constant, γ the surface energy, K is the surface curvature (this would correspond to $2/_{R}$ for our sphere of radius R in Fig. 2a) and K^* the critical curvature. Based on this kinetic stability criterion, if, from a starting point, a small increase in V leads to a negative $\dot{V}$, then the system will tend to move to its starting position, thus resembling a stable position. On the other hand, if a small increase of V results in a positive $\dot{V}$, the system will become unstable moving further from its starting point.

Importantly, for the case of the spherical droplet adhering to a flat surface, when considering the functional relationship between V and K, unstable equilibrium states emerge for a range of critical curvatures K^*.

If the latter increases due to a burst of biochemical driving forces (i.e. growth factors), the system will reach a state of unstable growth, otherwise will remain "dormant". Notably, here a single criterion provides information regarding the stability of both equilibrium (thermodynamic or mechanical stability) and growth (kinetic stability) states of the system. Following this kinetic stability criterion, the lifetime of the metastable dormant phase could be therefore discussed in simple terms based on the droplet surface curvature. This will in turn depend on the relative contribution of cells cortical tension, growth, division and apoptosis within the droplet, as well as cell-ECM interactions, as illustrated by the concepts of wetting and mechanical confinement.

1_Spherical droplet adhering to a flat wetting surface

We start by defining the total energy of the droplet by the sum of two contributions, one from the volume V and another from the surface area A (Fig. 2a):

$$E = -\varepsilon V + \sigma A \quad (1)$$

Both parameters ε and σ are positive.The parameter ε describes interactions between cells in the nodule and between cells and their own ECM. Such interactions are favorable, thus the negative sign in front of ε that makes the overall energy decrease when the volume increases. The parameter σ represents the interaction with a foreign ECM that is considered unfavorable, thus the positive sign in from of σ which makes the overall energy increase when the area increases. For a spherical droplet, it is immediate to relate surface area to volume, where $A = (36\pi)^{1/3}V^{2/3}$, and to plot (Fig. 2b, black line) the energy as a function of volume $E\ (V)$. This curve has a maximum at the critical volume V^*, and we call $E\ (V^*) = E^*$. From classical nucleation theory, the values for the critical volume, radius and energy for a spherical droplet in terms of ε and σ are defined as: $V^* = \frac{4\pi}{3}\left(\frac{2\sigma}{\varepsilon}\right)^3$, $R^* = \left(\frac{2\sigma}{\varepsilon}\right)^3$ and $E^* = \frac{16\pi\sigma^3}{3\varepsilon^2}$, respectively. Eq. (1) can then be written as:

$$\frac{E}{E^*} = -\frac{2}{V^*}V + \left(\frac{3}{4\pi V^{*2}}\right)^{1/3} A \quad (2)$$

For a spherical droplet, this equation will be: $E/_{E^*} = -2\,V/_{V^*} + 3\,V/_{V^*}{}^{2/3}$, and describes a classical nucleation process (Fig. 2b, black line).

We now hypothesize that the tissue adheres to a surface (that is "liked" by the tissue in the droplet) without costs in energy (in contrast to the interface with the foreign ECM). The sketch in Fig. 2a shows two configurations for a droplet taking the shape of a spherical cap adhering to a circular patch of radius R_0 on the flat surface. Outside this patch, the adherence is not favorable (in physical terms, the droplet would not wet the foreign ECM outside the circular patch). It is then straightforward to calculate the droplet volume and its area not adhering to the surface by adapting volume and area as follows:

$V = \frac{\pi}{3}h^2(3R-h)$, $A = 2\pi Rh$ where $h = \begin{cases} R + \sqrt{R^2 - R_0^2}\ (left) \\ R - \sqrt{R^2 - R_0^2}\ (right) \end{cases}$ with "left" and "right" referring to the respective two adherent spherical droplets in Fig. 2a and R being the radius of the sphere, and to insert these values into Eq. 2. The parameters E^*, V^* and R^* are the energy, the volume and radius of a critical spherical droplet.

2_Spherical droplet mechanically confined by an elastic sheath

Here we seek to understand how mechanical confinement provided by an elastic sheath, meant to resemble an ECM with a predominant elastic properties (neglecting the viscous component), restrains the growth of a spherical droplet starting from a volume V_0 (corresponding to a sphere of radius R_0) (Fig. 3). For this purpose, we add the elastic energy of the sheath to the total energy in Eq. (2), which for an incompressible neo-Hookean solid can be described as follows:

$$E_{sheath} = \begin{cases} 0 & for\ V \le V_0 \\ \frac{1}{2}M(2\lambda^2 + \lambda^{-4} - 3)\ for\ V \ge V_0 \end{cases}$$

The parameter $\lambda = R/_{R_0}$ is the linear inflation of the sphere and M describes the elastic properties of the material. This energy can then be added to Eq. (2). This adds two parameters to the problem, namely $\mu = \frac{1}{2}\,M/_{E^*}$, which puts the elastic stiffness of the sheath in relation to the critical energy of the droplet, and $\rho_0 = R_0/_{R^*}$, which puts the original unstretched radius of the sheath in relation to the critical radius of the droplet. A convenient way of writing the total energy is:

$$\frac{E}{E^*} = -2\rho^3 + 3\rho^2 + \begin{cases} 0 & for\ \rho < \rho_0 \\ \mu\left(2\left(\frac{\rho}{\rho_0}\right)^2 + \left(\frac{\rho}{\rho_0}\right)^{-4} - 3\right) for\ \rho \ge \rho_0 \end{cases} \quad (3)$$

where $\rho = R/_{R^*}$ and $\rho^3 = V/_{V^*}$. Fig. 3 shows this energy for two values of ρ_0 and several values of μ. Higher values of μ correspond to a higher elastic energy being stored in the sheath, while ρ_0 lower and higher than 1 represent a sheath which has an initial unstretched radius smaller and higher than the critical radius of the droplet, respectively. Given that the elastic energy of the sheath increases with the volume of the droplet, there is no minimum (outside $\rho = 0$) in the total energy, if $\rho_0 < 1$. For $\rho_0 > 1$ and for

a sufficiently stiff sheath, a minimum of the energy appears for a size larger than ρ_0 (how much larger will depend of the stiffness of the elastic sheath).

3_Spherical droplet with size-dependent growth

Here we consider a tissue that cannot survive below a distance D from the surface and is getting necrotic (Fig. 4). Hence, the volume in Eq. (1) is reduced to the outer shell with thickness D, as soon as the radius of the droplet $R > D$. Again, we consider for simplicity a spherical droplet. With similar notations as in Eq. (3) and with $\delta = {}^{D}/_{R^*}$ we get for this case:

$$\frac{E}{E^*} = 3\rho^2 - 2\begin{cases}\rho^3 & for\ \rho < \delta \\ \rho^3 - (\rho - \delta)^3 & for\ \rho \geq \delta\end{cases} \quad (4)$$

This is illustrated for several values of D in Fig. 4.

7

Conclusions

7.1 Applications and future directions

The most intuitive and immediate application of the system here presented, would be a quiescence-inducing material platform for the systematic screen of novel compounds meant to target potentially relapsing dormant cancer cells, as well as fundamental investigation of underlying biological mechanisms. This is of utmost importance, as the asymptomatic nature of cancer dormancy poses significant technical and ethical challenges for the identification, isolation and investigation of DTCs [28]. These are known to be rare and inaccessible in large numbers from clinical settings, further stressing the importance of having a fast and scalable drug screening method to investigate large populations of DTCs. Such effort is currently being undertaken in collaboration with the Fraunhofer Institute for Toxicology and Experimental Medicine (Fraunhofer-Institut für Toxikologie und Experimentelle Medizin ITEM), where they have access to high-throughput drug screening devices for target discovery.

Material-wise, the versatility of the alginate hydrogel presented would further allow tuning of different biophysical and biochemical properties of the environment other than stiffness (which has been the main focus of this project), while monitoring cell cycle progression. Some of these properties could be the presentation of different biomolecules (e.g. RGD), providing different means of degradation (active enzymatic [16]) or passive hydrolytic [96]), enabling stress relaxation or multiphasic patterning [97]). Similar efforts are currently being pursued in the group in the context of regenerative medicine and tissue engineering with stem cells. On the biological aspect, several aspects could be pursued; are the cells, despite being encapsulated in an inert material, in immediate contact with the hydrogel interface, or do they secrete their own extracellular matrix (ECM)? If yes, does the latter have a role in providing drug resistance? Via which signaling mechanism? These and many other questions concerning single quiescence cells-ECM interactions could be investigated in the future.

In this project we focused on a specific mechanosensitive signaling axis, the FHL2-p21, but further exploration of the RNA sequencing data provided here might inform other potentially-relevant targets, not only in the context of dormancy but also DNA damage, inflammation, senescence, autophagy or apoptosis processes. The promising results for the FHL2, on the other hand, might justify further investigation of its role in cancer dormancy with more sophisticated readouts enabled by CRISPR/Cas9 cells and mice knockouts.

Last but not least, the cells utilized here were cell lines. Ideally, the quiescence-inducing effect of the material platform should be verified for primary cells as well. Patient-derived DTCs, as most of quiescent host cells in the body, lose their dormant phenotype as soon as extracted from their niche; therefore a platform that could preserve their native state would be very beneficial. A similar clinical example which could benefit from this approach, is the ex-vivo implantation of rare hematopoietic stem cells (HSCs) during bone marrow transplantation. Like DTCs, HSCs lose their native quiescent phenotype when outside their niche, significantly diminishing their ability for long-term blood reconstitution. We believe that, with the appropriate tuning and improvement, others can benefit from this platform in particular, or from this approach in general, for applications that we might not have even considered.

7.2 Limitations

Despite its advantages, the presented material has limitations which can be mainly attributed to alginate. Its ultrapure form, through which the material has been made cyto-compatible with acceptable lot-to-lot variability, alginate can be considered a relatively expensive material compared to its synthetic counterparts. Furthermore, the process leading to full norbornene/RGD-functionalization (from dialysis to lyophilization), as examples of modifications performed in this project, requires around 7-10 days, a considerable amount of time especially if this needs to be repeated on several occasions. The versatility of alginate allows for controlled modulation of specific biophysical and biochemical properties to investigate well-defined research questions, but not to mimic the native physiological environment of cells. If the aim is to replicate a biologically faithful microenvironment with as many details as possible, then alginate hydrogels might not be the best option available. Materials such as conventional basement membrane-derived Matrigel, collagen or fibrin-based hydrogels, decellularized matrices or interpenetrating networks (IPN) could fit such purpose.

From the biological aspect, a limitation of this work lies in the employment of breast cancer cell lines, which, despite their undeniable usefulness as standard cells to establish proof-of-concepts, do not fulfill the requirement of physiological/clinical faithfulness. Any further claim will require validation with primary cells.

References

[1] Douglas Hanahan and Robert A. Weinberg. "Hallmarks of Cancer: The Next Generation". In: *Cell* 144.5 (Mar. 2011), pp. 646–674. ISSN: 00928674. DOI: 10.1016/j.cell.2011.02.013. URL: http://dx.doi.org/10.1016/j.cell.2011.02.013%20https://linkinghub.elsevier.com/retrieve/pii/S0092867411001279.

[2] Hadi T Nia, Lance L Munn, and Rakesh K Jain. "Physical traits of cancer". In: *Science* 370.6516 (Oct. 2020), eaaz0868. ISSN: 0036-8075. DOI: 10.1126/science.aaz0868. URL: http://www.ncbi.nlm.nih.gov/pubmed/33122355%20https://www.sciencemag.org/lookup/doi/10.1126/science.aaz0868.

[3] Amaia Cipitria and Manuel Salmeron-Sanchez. "Mechanotransduction and Growth Factor Signalling to Engineer Cellular Microenvironments". In: *Advanced Healthcare Materials* 6.15 (Aug. 2017), p. 1700052. ISSN: 21922640. DOI: 10.1002/adhm.201700052. URL: http://doi.wiley.com/10.1002/adhm.201700052.

[4] Thomas R. Cox. "The matrix in cancer". In: *Nature Reviews Cancer* 21.4 (Apr. 2021), pp. 217–238. ISSN: 1474-175X. DOI: 10.1038/s41568-020-00329-7. URL: http://dx.doi.org/10.1038/s41568-020-00329-7%20http://www.nature.com/articles/s41568-020-00329-7.

[5] Victoria G. Muir and Jason A. Burdick. "Chemically Modified Biopolymers for the Formation of Biomedical Hydrogels". In: *Chemical Reviews* 121.18 (Sept. 2021), pp. 10908–10949. ISSN: 0009-2665. DOI: 10.1021/acs.chemrev.0c00923. URL: https://pubs.acs.org/doi/10.1021/acs.chemrev.0c00923.

[6] Kyle H. Vining and David J. Mooney. "Mechanical forces direct stem cell behaviour in development and regeneration". In: *Nature Reviews Molecular Cell Biology* 18.12 (Dec. 2017), pp. 728–742. ISSN: 1471-0072. DOI: 10.1038/nrm.2017.108. arXiv: 15334406. URL: http://www.nature.com/articles/nrm.2017.108.

[7] Elizabeth A Aisenbrey and William L Murphy. "Synthetic alternatives to Matrigel". In: *Nature Reviews Materials* (May 2020). ISSN: 2058-8437. DOI: 10.1038/s41578-020-0199-8. URL: http://www.nature.com/articles/s41578-020-0199-8.

[8] Kuen Yong Lee and David J. Mooney. "Alginate: Properties and biomedical applications". In: *Progress in Polymer Science* 37.1 (Jan. 2012), pp. 106–126. ISSN: 00796700. DOI: 10.1016/j.progpolymsci.2011.06.003. URL: http://dx.doi.org/10.1016/j.progpolymsci.2011.06.003%20https://linkinghub.elsevier.com/retrieve/pii/S0079670011000918.

[9] Kuen Yong Lee, Hyun Joon Kong, and David J. Mooney. "Quantifying Interactions between Cell Receptors and Adhesion Ligand-Modified Polymers in Solution". In: *Macromolecular Bioscience* 8.2 (Feb. 2008), pp. 140–145. ISSN: 16165187. DOI: 10.1002/mabi.200700169. URL: https://onlinelibrary.wiley.com/doi/10.1002/mabi.200700169.

[10] Hsiao-Li Ma et al. "Chondrogenesis of human mesenchymal stem cells encapsulated in alginate beads". In: *Journal of Biomedical Materials Research* 64A.2 (Feb. 2003), pp. 273–281. ISSN: 0021-9304. DOI: 10.1002/jbm.a.10370. URL: https://onlinelibrary.wiley.com/doi/10.1002/jbm.a.10370.

[11] Yash M. Kolambkar et al. "An alginate-based hybrid system for growth factor delivery in the functional repair of large bone defects". In: *Biomaterials* 32.1 (Jan. 2011), pp. 65–74. ISSN: 01429612. DOI: 10.1016/j.biomaterials.2010.08.074. URL: http://dx.doi.org/10.1016/j.biomaterials.2010.08.074%20https://linkinghub.elsevier.com/retrieve/pii/S0142961210011129.

[12] Eduardo A. Silva and David J. Mooney. "Effects of VEGF temporal and spatial presentation on angiogenesis". In: *Biomaterials* 31.6 (Feb. 2010), pp. 1235–1241. ISSN: 01429612. DOI: 10.1016/j.biomaterials.2009.10.052. URL: http://dx.doi.org/10.1016/j.biomaterials.2009.10.052%20https://linkinghub.elsevier.com/retrieve/pii/S0142961209011739.

[13] Ovijit Chaudhuri et al. "Extracellular matrix stiffness and composition jointly regulate the induction of malignant phenotypes in mammary epithelium". In: *Nature Materials* 13.10 (Oct. 2014), pp. 970–978. ISSN: 1476-1122. DOI: 10.1038/nmat4009. URL: http://www.nature.com/articles/nmat4009.

[14] Ovijit Chaudhuri et al. "Hydrogels with tunable stress relaxation regulate stem cell fate and activity". In: *Nature Materials* 15.3 (Mar. 2016), pp. 326–334. ISSN: 1476-1122. DOI: 10.1038/nmat4489. URL: http://www.nature.com/articles/nmat4489.

[15] Nathaniel Huebsch et al. "Harnessing traction-mediated manipulation of the cell/matrix interface to control stem-cell fate". In: *Nature Materials* 9.6 (June 2010), pp. 518–526. ISSN: 1476-1122. DOI: 10.1038/nmat2732. URL: http://www.nature.com/articles/nmat2732.

[16] Aline Lueckgen et al. "Enzymatically-degradable alginate hydrogels promote cell spreading and in vivo tissue infiltration". In: *Biomaterials* 217 (Oct. 2019), p. 119294. ISSN: 01429612. DOI: 10.1016/j.biomaterials.2019.119294. URL: http://www.sciencedirect.com/science/article/pii/S014296121930393X%20https://linkinghub.elsevier.com/retrieve/pii/S014296121930393X.

[17] Mireia Alemany-Ribes and Carlos E. Semino. "Bioengineering 3D environments for cancer models". In: *Advanced Drug Delivery Reviews* 79-80 (Dec. 2014), pp. 40–49. ISSN: 0169409X. DOI: 10.1016/j.addr.2014.06.004. URL: http://dx.doi.org/10.1016/j.addr.2014.06.004%20https://linkinghub.elsevier.com/retrieve/pii/S0169409X14001367.

[18] Juliane Winkler et al. “Concepts of extracellular matrix remodelling in tumour progression and metastasis”. In: *Nature Communications* 11.1 (Dec. 2020), p. 5120. ISSN: 2041-1723. DOI: 10.1038/s41467-020-18794-x. URL: http://dx.doi.org/10.1038/s41467-020-18794-x%20http://www.nature.com/articles/s41467-020-18794-x%20https://www.nature.com/articles/s41467-020-18794-x.

[19] O. W. Petersen et al. “Interaction with basement membrane serves to rapidly distinguish growth and differentiation pattern of normal and malignant human breast epithelial cells.” In: *Proceedings of the National Academy of Sciences* 89.19 (Oct. 1992), pp. 9064–9068. ISSN: 0027-8424. DOI: 10.1073/pnas.89.19.9064. URL: http://www.pnas.org/cgi/doi/10.1073/pnas.89.19.9064.

[20] V.M. Weaver et al. “Reversion of the Malignant Phenotype of Human Breast Cells in Three-Dimensional Culture and In Vivo by Integrin Blocking Antibodies”. In: *Journal of Cell Biology* 137.1 (Apr. 1997), pp. 231–245. ISSN: 0021-9525. DOI: 10.1083/jcb.137.1.231. URL: https://rupress.org/jcb/article/137/1/231/15446/Reversion-of-the-Malignant-Phenotype-of-Human.

[21] Stuart E Jones and Jay T Lennon. “Dormancy contributes to the maintenance of microbial diversity”. In: *Proceedings of the National Academy of Sciences* 107.13 (Mar. 2010), pp. 5881–5886. ISSN: 0027-8424. DOI: 10.1073/pnas.0912765107. URL: http://www.ncbi.nlm.nih.gov/pubmed/20231463%20http://www.pubmedcentral.nih.gov/articlerender.fcgi?artid=PMC2851880%20http://www.pnas.org/cgi/doi/10.1073/pnas.0912765107.

[22] John Wang. “Global analysis of dauer gene expression in Caenorhabditis elegans”. In: *Development* 130.8 (Apr. 2003), pp. 1621–1634. ISSN: 09501991. DOI: 10.1242/dev.00363. URL: http://dev.biologists.org/content/130/8/1621.abstract%20http://dev.biologists.org/cgi/doi/10.1242/dev.00363.

[23] Maarten Koornneef, Leónie Bentsink, and Henk Hilhorst. “Seed dormancy and germination”. In: *Current Opinion in Plant Biology* 5.1 (Feb. 2002), pp. 33–36. ISSN: 13695266. DOI: 10.1016/S1369-5266(01)00219-9. URL: https://academic.oup.com/jxb/article-lookup/doi/10.1093/jxb/erq063%20https://linkinghub.elsevier.com/retrieve/pii/S1369526601002199.

[24] Linheng Li and Hans Clevers. “Coexistence of Quiescent and Active”. In: *Science* 327.January (2010), pp. 542–545.

[25] Devon A. Lawson et al. “Tumour heterogeneity and metastasis at single-cell resolution”. In: *Nature Cell Biology* 20.12 (Dec. 2018), pp. 1349–1360. ISSN: 1465-7392. DOI: 10.1038/s41556-018-0236-7. URL: http://www.nature.com/articles/s41556-018-0236-7.

[26] Julio A. Aguirre-Ghiso. “Models, mechanisms and clinical evidence for cancer dormancy”. In: *Nature Reviews Cancer* 7.11 (Nov. 2007), pp. 834–846. ISSN: 1474-175X. DOI: 10.1038/nrc2256. URL: http://www.nature.com/articles/nrc2256.

[27] Christoph A. Klein. “Cancer progression and the invisible phase of metastatic colonization”. In: *Nature Reviews Cancer* 20.11 (Nov. 2020), pp. 681–694. ISSN: 1474-175X. DOI:

10.1038/s41568-020-00300-6. URL: http://dx.doi.org/10.1038/s41568-020-00300-6%20http://www.nature.com/articles/s41568-020-00300-6.

[28] Marco Montagner and Erik Sahai. "In vitro models of breast cancer metastatic dormancy". In: *Frontiers in cell and developmental biology* 8 (2020), p. 37.

[29] Shantanu Pradhan et al. "Engineered In Vitro Models of Tumor Dormancy and Reactivation". In: *Journal of Biological Engineering* 12.1 (Dec. 2018), p. 37. ISSN: 1754-1611. DOI: 10.1186/s13036-018-0120-9. URL: https://jbioleng.biomedcentral.com/articles/10.1186/s13036-018-0120-9.

[30] Dalit Barkan et al. "Inhibition of Metastatic Outgrowth from Single Dormant Tumor Cells by Targeting the Cytoskeleton". In: *Cancer Research* 68.15 (Aug. 2008), pp. 6241–6250. ISSN: 0008-5472. DOI: 10.1158/0008-5472.CAN-07-6849. URL: http://cancerres.aacrjournals.org/lookup/doi/10.1158/0008-5472.CAN-07-6849.

[31] Dalit Barkan et al. "Metastatic Growth from Dormant Cells Induced by a Col-I–Enriched Fibrotic Environment". In: *Cancer Research* 70.14 (July 2010), pp. 5706–5716. ISSN: 0008-5472. DOI: 10.1158/0008-5472.CAN-09-2356. URL: http://cancerres.aacrjournals.org/lookup/doi/10.1158/0008-5472.CAN-09-2356.

[32] Donna M. Sosnoski et al. "Dormancy and growth of metastatic breast cancer cells in a bone-like microenvironment". In: *Clinical Experimental Metastasis* 32.4 (Apr. 2015), pp. 335–344. ISSN: 0262-0898. DOI: 10.1007/s10585-015-9710-9. URL: http://link.springer.com/10.1007/s10585-015-9710-9.

[33] Xin Lu et al. "VCAM-1 Promotes Osteolytic Expansion of Indolent Bone Micrometastasis of Breast Cancer by Engaging $\alpha4\beta1$-Positive Osteoclast Progenitors". In: *Cancer Cell* 20.6 (Dec. 2011), pp. 701–714. ISSN: 15356108. DOI: 10.1016/j.ccr.2011.11.002. URL: https://linkinghub.elsevier.com/retrieve/pii/S1535610811004089.

[34] Jean Albrengues et al. "Neutrophil extracellular traps produced during inflammation awaken dormant cancer cells in mice". In: *Science* 361.6409 (Sept. 2018). ISSN: 0036-8075. DOI: 10.1126/science.aao4227. URL: https://www.science.org/doi/10.1126/science.aao4227.

[35] Ryan A. Carpenter et al. "Implantable pre-metastatic niches for the study of the microenvironmental regulation of disseminated human tumour cells". In: *Nature Biomedical Engineering* 2.12 (Dec. 2018), pp. 915–929. ISSN: 2157-846X. DOI: 10.1038/s41551-018-0307-x. URL: http://dx.doi.org/10.1038/s41551-018-0307-x%20http://www.nature.com/articles/s41551-018-0307-x.

[36] S. E. Wheeler et al. "Spontaneous dormancy of metastatic breast cancer cells in an all human liver microphysiologic system". In: *British Journal of Cancer* 111.12 (Dec. 2014), pp. 2342–2350. ISSN: 0007-0920. DOI: 10.1038/bjc.2014.533. URL: http://www.nature.com/articles/bjc2014533.

[37] Marco Montagner et al. "Crosstalk with lung epithelial cells regulates Sfrp2-mediated latency in breast cancer dissemination". In: *Nature Cell Biology* 22.3 (Mar. 2020), pp. 289–296. ISSN: 1465-7392. DOI: 10.1038/s41556-020-0474-3. URL: http://dx.doi.

org/10.1038/s41556-020-0474-3%20http://www.nature.com/articles/s41556-020-0474-3.

[38] Cyrus M. Ghajar et al. "The perivascular niche regulates breast tumour dormancy". In: *Nature Cell Biology* 15.7 (July 2013), pp. 807–817. ISSN: 1465-7392. DOI: 10.1038/ncb2767. URL: http://www.nature.com/articles/ncb2767.

[39] Rebecca Marlow et al. "A Novel Model of Dormancy for Bone Metastatic Breast Cancer Cells". In: *Cancer Research* 73.23 (Dec. 2013), pp. 6886–6899. ISSN: 0008-5472. DOI: 10.1158/0008-5472.CAN-13-0991. URL: http://cancerres.aacrjournals.org/lookup/doi/10.1158/0008-5472.CAN-13-0991.

[40] Patrick Carlson et al. "Targeting the perivascular niche sensitizes disseminated tumour cells to chemotherapy". In: *Nature Cell Biology* 21.2 (Feb. 2019), pp. 238–250. ISSN: 1465-7392. DOI: 10.1038/s41556-018-0267-0. URL: http://www.nature.com/articles/s41556-018-0267-0.

[41] Ryann E. Shor et al. "The PI3K/mTOR inhibitor Gedatolisib eliminates dormant breast cancer cells in organotypic culture, but fails to prevent metastasis in preclinical settings". In: *Molecular Oncology* (June 2021), pp. 1878–0261.13031. ISSN: 1574-7891. DOI: 10.1002/1878-0261.13031. URL: https://pubmed.ncbi.nlm.nih.gov/34058066/%20https://onlinelibrary.wiley.com/doi/10.1002/1878-0261.13031.

[42] Hak Rae Lee, Faith Leslie, and Samira M. Azarin. "A facile in vitro platform to study cancer cell dormancy under hypoxic microenvironments using CoCl2". In: *Journal of Biological Engineering* 12.1 (Dec. 2018), p. 12. ISSN: 1754-1611. DOI: 10.1186/s13036-018-0106-7. URL: https://jbioleng.biomedcentral.com/articles/10.1186/s13036-018-0106-7.

[43] Hak Rae Lee et al. "Biomaterial Platform To Establish a Hypoxic Metastatic Niche in Vivo". In: *ACS Applied Bio Materials* 2.4 (Apr. 2019), pp. 1549–1560. ISSN: 2576-6422. DOI: 10.1021/acsabm.8b00837. URL: http://pubs.acs.org/doi/10.1021/acsabm.8b00837.

[44] Judith Barrios and Robert Wieder. "Dual FGF-2 and intergrin $\alpha5\beta1$ signaling mediate GRAF-induced RhoA inactivation in a model of breast cancer dormancy". In: *Cancer Microenvironment* 2.1 (2009), pp. 33–47.

[45] Tiffany Lam et al. "Immobilization rapidly selects for chemoresistant ovarian cancer cells with enhanced ability to enter dormancy". In: *Biotechnology and bioengineering* 117.10 (2020), pp. 3066–3080.

[46] Julian Preciado et al. "Induction of dormancy by confinement: An agarose-silica biomaterial for isolating and analyzing dormant cancer cells". In: *Journal of Biomedical Materials Research Part B: Applied Biomaterials* December 2020 (May 2021), jbm.b.34859. ISSN: 1552-4973. DOI: 10.1002/jbm.b.34859. URL: https://onlinelibrary.wiley.com/doi/10.1002/jbm.b.34859.

[47] Cindy J Farino, Shantanu Pradhan, and John H. Slater. "The Influence of Matrix-Induced Dormancy on Metastatic Breast Cancer Chemoresistance". In: *ACS Applied Bio Materials* 3.9 (Sept. 2020), pp. 5832–5844. ISSN: 2576-6422. DOI: 10.1021/acsabm.0c00549. URL: https://dx.doi.org/10.1021/acsabm.0c00549%20https://pubs.acs.org/doi/10.1021/acsabm.0c00549.

[48] Shantanu Pradhan and John H. Slater. "Tunable hydrogels for controlling phenotypic cancer cell states to model breast cancer dormancy and reactivation". In: *Biomaterials* 215 (Sept. 2019), p. 119177. ISSN: 01429612. DOI: 10.1016/j.biomaterials.2019.04.022. URL: https://linkinghub.elsevier.com/retrieve/pii/S014296121930239X.

[49] Cindy J. Farino Reyes, Shantanu Pradhan, and John H Slater. "The Influence of Ligand Density and Degradability on Hydrogel Induced Breast Cancer Dormancy and Reactivation". In: *Advanced Healthcare Materials* 2002227 (Apr. 2021), p. 2002227. ISSN: 2192-2640. DOI: 10.1002/adhm.202002227. URL: https://onlinelibrary.wiley.com/doi/10.1002/adhm.202002227.

[50] Melanie Werner-Klein et al. "Interleukin-6 trans-signaling is a candidate mechanism to drive progression of human DCCs during clinical latency". In: *Nature Communications* 11.1 (Dec. 2020), p. 4977. ISSN: 2041-1723. DOI: 10.1038/s41467-020-18701-4. URL: http://www.nature.com/articles/s41467-020-18701-4.

[51] Hayden Huang, Roger D. Kamm, and Richard T. Lee. "Cell mechanics and mechanotransduction: pathways, probes, and physiology". In: *American Journal of Physiology-Cell Physiology* 287.1 (July 2004), pp. C1–C11. ISSN: 0363-6143. DOI: 10.1152/ajpcell.00559.2003. URL: https://doi.org/10.1038/nrc3080%20http://10.0.4.14/nrc3080%20https://www.physiology.org/doi/10.1152/ajpcell.00559.2003.

[52] Denis Wirtz, Konstantinos Konstantopoulos, and Peter C Searson. "The physics of cancer: the role of physical interactions and mechanical forces in metastasis". In: *Nature Reviews Cancer* 11.7 (2011), pp. 512–522.

[53] Marta Urbanska et al. "Single-cell mechanical phenotype is an intrinsic marker of reprogramming and differentiation along the mouse neural lineage". In: *Development* 144.23 (Dec. 2017), pp. 4313–4321. ISSN: 1477-9129. DOI: 10.1242/dev.155218. URL: https://journals.biologists.com/dev/article/144/23/4313/19252/Single-cell-mechanical-phenotype-is-an-intrinsic.

[54] Vinay Swaminathan et al. "Mechanical Stiffness Grades Metastatic Potential in Patient Tumor Cells and in Cancer Cell Lines". In: *Cancer Research* 71.15 (Aug. 2011), pp. 5075–5080. ISSN: 0008-5472. DOI: 10.1158/0008-5472.CAN-11-0247. URL: http://cancerres.aacrjournals.org/lookup/doi/10.1158/0008-5472.CAN-11-0247.

[55] Claude N Holenstein et al. "The relationship between metastatic potential and in vitro mechanical properties of osteosarcoma cells". In: *Molecular biology of the cell* 30.7 (2019), pp. 887–898.

[56] Pei-Hsun Wu et al. "A comparison of methods to assess cell mechanical properties". In: *Nature Methods* 15.7 (July 2018), pp. 491–498. ISSN: 1548-7091. DOI: 10.1038/s41592-018-0015-1. URL: http://www.nature.com/articles/s41592-018-0015-1.

[57] Francesca Palombo and Daniele Fioretto. “Brillouin Light Scattering: Applications in Biomedical Sciences”. In: *Chemical Reviews* 119.13 (July 2019), pp. 7833–7847. ISSN: 0009-2665. DOI: 10.1021/acs.chemrev.9b00019. URL: http://pubs.acs.org/doi/10.1021/acs.chemrev.9b00019%20https://pubs.acs.org/doi/10.1021/acs.chemrev.9b00019.

[58] Robert Prevedel et al. “Brillouin microscopy: an emerging tool for mechanobiology”. In: *Nature Methods* 16.10 (Oct. 2019), pp. 969–977. ISSN: 1548-7091. DOI: 10.1038/s41592-019-0543-3. URL: http://dx.doi.org/10.1038/s41592-019-0543-3%20http://www.nature.com/articles/s41592-019-0543-3.

[59] Gabriel Popescu et al. “Optical imaging of cell mass and growth dynamics”. In: *American Journal of Physiology-Cell Physiology* 295.2 (Aug. 2008), pp. C538–C544. ISSN: 0363-6143. DOI: 10.1152/ajpcell.00121.2008. URL: https://www.physiology.org/doi/10.1152/ajpcell.00121.2008.

[60] H. G. DAVIES and M. H. F. WILKINS. “Interference Microscopy and Mass Determination”. In: *Nature* 169.4300 (Mar. 1952), pp. 541–541. ISSN: 0028-0836. DOI: 10.1038/169541a0. URL: http://www.nature.com/articles/169541a0.

[61] Shigenobu Toné et al. “Three distinct stages of apoptotic nuclear condensation revealed by time-lapse imaging, biochemical and electron microscopy analysis of cell-free apoptosis”. In: *Experimental Cell Research* 313.16 (Oct. 2007), pp. 3635–3644. ISSN: 00144827. DOI: 10.1016/j.yexcr.2007.06.018. URL: https://linkinghub.elsevier.com/retrieve/pii/S0014482707002832.

[62] Shada Abuhattum et al. “Intracellular Mass Density Increase Is Accompanying but Not Sufficient for Stiffening and Growth Arrest of Yeast Cells”. In: *Frontiers in Physics* 6 (Nov. 2018). ISSN: 2296-424X. DOI: 10.3389/fphy.2018.00131. URL: https://www.frontiersin.org/article/10.3389/fphy.2018.00131/full.

[63] Matthias Christoph Munder et al. “A pH-driven transition of the cytoplasm from a fluid- to a solid-like state promotes entry into dormancy”. In: *eLife* 5.MARCH2016 (Mar. 2016), pp. 1–30. ISSN: 2050-084X. DOI: 10.7554/eLife.09347. arXiv: NIHMS150003. URL: https://elifesciences.org/articles/09347.

[64] Simon Alberti and Anthony A. Hyman. “Biomolecular condensates at the nexus of cellular stress, protein aggregation disease and ageing”. In: *Nature Reviews Molecular Cell Biology* 22.3 (Mar. 2021), pp. 196–213. ISSN: 1471-0072. DOI: 10.1038/s41580-020-00326-6. URL: http://dx.doi.org/10.1038/s41580-020-00326-6%20http://www.nature.com/articles/s41580-020-00326-6.

[65] Salman F. Banani et al. “Biomolecular condensates: organizers of cellular biochemistry”. In: *Nature Reviews Molecular Cell Biology* 18.5 (May 2017), pp. 285–298. ISSN: 1471-0072. DOI: 10.1038/nrm.2017.7. URL: http://www.nature.com/articles/nrm.2017.7.

[66] Peter M. A. Sloot, Alfons G. Hoekstra, and Carl G. Figdor. “Osmotic response of lymphocytes measured by means of forward light scattering: Theoretical considerations”. In: *Cytometry* 9.6 (Nov. 1988), pp. 636–641. ISSN: 0196-4763. DOI: 10.1002/cyto.990090620. URL: http://doi.wiley.com/10.1002/cyto.990090620.

[67] Albert Brunsting and Paul F. Mullaney. “Differential Light Scattering from Spherical Mammalian Cells”. In: *Biophysical Journal* 14.6 (June 1974), pp. 439–453. ISSN: 00063495. DOI: 10.1016/S0006-3495(74)85925-4. URL: http://dx.doi.org/10.1016/S0006-3495(74)85925-4%20https://linkinghub.elsevier.com/retrieve/pii/S0006349574859254.

[68] Rebekah Drezek et al. “Light scattering from cervical cells throughout neoplastic progression: influence of nuclear morphology, DNA content, and chromatin texture”. In: *Journal of Biomedical Optics* 8.1 (2003), p. 7. ISSN: 10833668. DOI: 10.1117/1.1528950. URL: http://biomedicaloptics.spiedigitallibrary.org/article.aspx?doi=10.1117/1.1528950.

[69] Valery V. Tuchin. “Light propagation in tissues with controlled optical properties”. In: *Journal of Biomedical Optics* 2.4 (1997), p. 401. ISSN: 10833668. DOI: 10.1117/12.281502. URL: http://biomedicaloptics.spiedigitallibrary.org/article.aspx?doi=10.1117/12.281502.

[70] Mirjam Schürmann et al. “Cell nuclei have lower refractive index and mass density than cytoplasm”. In: *Journal of Biophotonics* 9.10 (Oct. 2016), pp. 1068–1076. ISSN: 1864063X. DOI: 10.1002/jbio.201500273. URL: http://doi.wiley.com/10.1002/jbio.201500273.

[71] Zachary A. Steelman et al. “Is the nuclear refractive index lower than cytoplasm? Validation of phase measurements and implications for light scattering technologies”. In: *Journal of Biophotonics* 10.12 (Dec. 2017), pp. 1714–1722. ISSN: 1864063X. DOI: 10.1002/jbio.201600314. URL: http://doi.wiley.com/10.1002/jbio.201600314.

[72] Hossein Hassani and Eva Kreysing. “Noninvasive measurement of the refractive index of cell organelles using surface plasmon resonance microscopy”. In: *Optics Letters* 44.6 (Mar. 2019), p. 1359. ISSN: 0146-9592. DOI: 10.1364/OL.44.001359. URL: https://www.osapublishing.org/abstract.cfm?URI=ol-44-6-1359.

[73] Nathan J. Mudrak, Priyanka S. Rana, and Michael A. Model. “Calibrated brightfield-based imaging for measuring intracellular protein concentration”. In: *Cytometry Part A* 93.3 (Mar. 2018), pp. 297–304. ISSN: 15524922. DOI: 10.1002/cyto.a.23145. URL: http://doi.wiley.com/10.1002/cyto.a.23145.

[74] Ryosuke Imai et al. “Density imaging of heterochromatin in live cells using orientation-independent-DIC microscopy”. In: *Molecular Biology of the Cell* 28.23 (Nov. 2017). Ed. by Jennifer Lippincott-Schwartz, pp. 3349–3359. ISSN: 1059-1524. DOI: 10.1091/mbc.e17-06-0359. URL: https://www.molbiolcell.org/doi/10.1091/mbc.e17-06-0359.

[75] Kyoohyun Kim and Jochen Guck. “The Relative Densities of Cytoplasm and Nuclear Compartments Are Robust against Strong Perturbation”. In: *Biophysical Journal* 119.10 (Nov. 2020), pp. 1946–1957. ISSN: 00063495. DOI: 10.1016/j.bpj.2020.08.044. URL: https://linkinghub.elsevier.com/retrieve/pii/S0006349520308092.

[76] Stefan Sieber et al. “Bone marrow-on-a-chip: Long-term culture of human haematopoietic stem cells in a three-dimensional microfluidic environment”. In: *Journal of Tissue*

Engineering and Regenerative Medicine 12.2 (Feb. 2018), pp. 479–489. ISSN: 19326254. DOI: 10.1002/term.2507. URL: http://doi.wiley.com/10.1002/term.2507.

[77] Frank C. Cackowski and Russell S. Taichman. "Parallels between hematopoietic stem cell and prostate cancer disseminated tumor cell regulation". In: *Bone* 119 (Feb. 2019), pp. 82–86. ISSN: 87563282. DOI: 10.1016/j.bone.2018.02.025. URL: https://doi.org/10.1016/j.bone.2018.02.025%20https://linkinghub.elsevier.com/retrieve/pii/S875632821830084X.

[78] Saskia J.E. Suijkerbuijk and Jacco van Rheenen. "From good to bad: Intravital imaging of the hijack of physiological processes by cancer cells". In: *Developmental Biology* 428.2 (Aug. 2017), pp. 328–337. ISSN: 00121606. DOI: 10.1016/j.ydbio.2017.04.015. arXiv: arXiv:1506.04967. URL: http://dx.doi.org/10.1016/j.ydbio.2017.04.015%20https://linkinghub.elsevier.com/retrieve/pii/S0012160617300544.

[79] Yusuke Shiozawa et al. "Human prostate cancer metastases target the hematopoietic stem cell niche to establish footholds in mouse bone marrow". In: *Journal of Clinical Investigation* 121.4 (Apr. 2011), pp. 1298–1312. ISSN: 0021-9738. DOI: 10.1172/JCI43414. URL: http://www.jci.org/articles/view/43414.

[80] Gloria Allocca et al. "The bone metastasis niche in breast cancer: potential overlap with the haematopoietic stem cell niche in vivo". In: *Journal of Bone Oncology* 17 (Aug. 2019), p. 100244. ISSN: 22121374. DOI: 10.1016/j.jbo.2019.100244. URL: https://linkinghub.elsevier.com/retrieve/pii/S2212137419300387.

[81] Abhishek Dhawan et al. "Breast cancer cells compete with hematopoietic stem and progenitor cells for intercellular adhesion molecule 1-mediated binding to the bone marrow microenvironment". In: *Carcinogenesis* 37.8 (Aug. 2016), pp. 759–767. ISSN: 0143-3334. DOI: 10.1093/carcin/bgw057. URL: https://academic.oup.com/carcin/article-lookup/doi/10.1093/carcin/bgw057.

[82] Paul C.W. Davies, Lloyd Demetrius, and Jack A. Tuszynski. "Cancer as a dynamical phase transition". In: *Theoretical Biology and Medical Modelling* 8.1 (2011), p. 30. ISSN: 1742-4682. DOI: 10.1186/1742-4682-8-30. URL: http://tbiomed.biomedcentral.com/articles/10.1186/1742-4682-8-30.

[83] Wenying Kang et al. "A novel jamming phase diagram links tumor invasion to non-equilibrium phase separation". In: *iScience* (Oct. 2021), p. 103252. ISSN: 25890042. DOI: 10.1016/j.isci.2021.103252. URL: https://doi.org/10.1016/j.isci.2021.103252%20https://linkinghub.elsevier.com/retrieve/pii/S2589004221012219.

[84] S. Eugene Machlin. *An Introduction to Aspects of Thermodynamics and Kinetics Relevant to Materials Science*. Elsevier, 2007. ISBN: 9780080466156. DOI: 10.1016/B978-0-08-046615-6.X5016-4. URL: https://linkinghub.elsevier.com/retrieve/pii/B9780080466156X50164.

[85] J. W. C. Dunlop et al. "The Emergence of Complexity from a Simple Model for Tissue Growth". In: *Journal of Statistical Physics* 180.1-6 (Sept. 2020), pp. 459–473. ISSN: 0022-4715. DOI: 10.1007/s10955-019-02461-7. URL: https://doi.org/10.1007/s10955-019-02461-7%20http://link.springer.com/10.1007/s10955-019-02461-7.

[86] F. Dieter Fischer et al. “Tissue growth controlled by geometric boundary conditions: a simple model recapitulating aspects of callus formation and bone healing”. In: *Journal of The Royal Society Interface* 12.107 (June 2015), p. 20150108. ISSN: 1742-5689. DOI: 10.1098/rsif.2015.0108. URL: https://royalsocietypublishing.org/doi/10.1098/rsif.2015.0108.

[87] C. J. Cyron and R. C. Aydin. “Mechanobiological free energy: a variational approach to tensional homeostasis in tissue equivalents”. In: *ZAMM - Journal of Applied Mathematics and Mechanics / Zeitschrift für Angewandte Mathematik und Mechanik* 97.9 (Sept. 2017), pp. 1011–1019. ISSN: 00442267. DOI: 10.1002/zamm.201600126. URL: http://doi.wiley.com/10.1002/zamm.201600126.

[88] C. J. Cyron, J. S. Wilson, and J. D. Humphrey. “Mechanobiological stability: A new paradigm to understand the enlargement of aneurysms?” In: *Journal of the Royal Society Interface* 11.100 (2014). ISSN: 17425662. DOI: 10.1098/rsif.2014.0680.

[89] C.J. Cyron and J.D. Humphrey. “Vascular homeostasis and the concept of mechanobiological stability”. In: *International Journal of Engineering Science* 85 (Dec. 2014), pp. 203–223. ISSN: 00207225. DOI: 10.1016/j.ijengsci.2014.08.003. URL: http://www.sciencedirect.com/science/article/pii/S002072251400175X%20https://linkinghub.elsevier.com/retrieve/pii/S002072251400175X.

[90] Sadra Bakhshandeh et al. “Optical quantification of intracellular mass density and cell mechanics in 3D mechanical confinement”. In: *Soft Matter* (2020). ISSN: 1744-683X. DOI: 10.1039/D0SM01556C. URL: http://xlink.rsc.org/?DOI=D0SM01556C.

[91] John Melngailis. “Focused ion beam technology and applications”. In: *Journal of Vacuum Science Technology B: Microelectronics and Nanometer Structures* 5.2 (1987), p. 469. ISSN: 0734211X. DOI: 10.1116/1.583937.

[92] Hans Moor. “Theory and Practice of High Pressure Freezing”. In: *Cryotechniques in Biological Electron Microscopy*. Berlin, Heidelberg: Springer Berlin Heidelberg, 1987, pp. 175–191. DOI: 10.1007/978-3-642-72815-0_8. URL: http://link.springer.com/10.1007/978-3-642-72815-0_8.

[93] Daniele Spehner et al. “Cryo-FIB-SEM as a promising tool for localizing proteins in 3D”. In: *Journal of Structural Biology* 211.1 (July 2020), p. 107528. ISSN: 10478477. DOI: 10.1016/j.jsb.2020.107528. URL: https://linkinghub.elsevier.com/retrieve/pii/S1047847720301015.

[94] P. Y. Liu et al. “Cell refractive index for cell biology and disease diagnosis: past, present and future”. In: *Lab on a Chip* 16.4 (2016), pp. 634–644. ISSN: 1473-0197. DOI: 10.1039/C5LC01445J. URL: http://xlink.rsc.org/?DOI=C5LC01445J.

[95] Asako Sakaue-Sawano et al. “Visualizing Spatiotemporal Dynamics of Multicellular Cell-Cycle Progression”. In: *Cell* 132.3 (Feb. 2008), pp. 487–498. ISSN: 00928674. DOI: 10.1016/j.cell.2007.12.033. URL: https://linkinghub.elsevier.com/retrieve/pii/S0092867408000548.

[96] Aline Lueckgen et al. “Hydrolytically-degradable click-crosslinked alginate hydrogels”. In: *Biomaterials* 181 (Oct. 2018), pp. 189–198. ISSN: 01429612. DOI: 10.1016/j.biomaterials.2018.07.031. URL: https://doi.org/10.1016/j.biomaterials.2018.07.031%20https://linkinghub.elsevier.com/retrieve/pii/S0142961218305167.

[97] Aline Lueckgen et al. “Dual alginate crosslinking for local patterning of biophysical and biochemical properties”. In: *Acta Biomaterialia* 115 (Oct. 2020), pp. 185–196. ISSN: 17427061. DOI: 10.1016/j.actbio.2020.07.047. URL: https://doi.org/10.1016/j.actbio.2020.07.047%20https://linkinghub.elsevier.com/retrieve/pii/S1742706120304335.